AN INVESTIGATION OF LIGHTWEIGHT CONCEPTS FOR

LOW-FREQUENCY PERFORMANCE ENHANCEMENT IN ACOUSTIC LINERS

By

ALEXANDER A. SVETGOFF

Bachelor of Science in Mechanical Engineering

Oklahoma State University

Stillwater, Oklahoma

2018

Submitted to the Faculty of the
Graduate College of the
Oklahoma State University
in partial fulfillment of
the requirements for
the Degree of
MASTER OF SCIENCE
May, 2021

AN INVESTIGATION OF LIGHTWEIGHT CONCEPTS FOR

LOW-FREQUENCY PERFORMANCE ENHANCEMENT IN ACOUSTIC LINERS

Thesis Approved:

Dr. James Manimala

Thesis Adviser

Dr. Richard Gaeta

Dr. Kursat Kara

Name: ALEXANDER SVETGOFF

Date of Degree: MAY, 2021

Title of Study: AN INVESTIGATION OF LIGHTWEIGHT CONCEPTS FOR LOW-

FREQUENCY PERFORMANCE ENHANCEMENT IN ACOUSTIC LINERS

Major Field: MECHANICAL AND AEROSPACE ENGINEERING

Abstract:

Acoustic liners are extensively used to reduce noise emitted by aircraft engines. However, conventional acoustic liners are largely ineffective for low-frequency noise content (<~1000 Hz) due to impractical mass and volume requirements. Airborne noise regulations are becoming more and more stringent and new technologies such as ultra-high bypass ratio turbofan engines display a marked increase in low-frequency noise components. In this study, three lightweight and compact, low-frequency acoustic liner concepts – Membrane-Embedded (MEL), Folded Cavity (FCL), and Carbon Foam (CFL) Liners are investigated using normal-incidence impedance tube tests to better understand the mechanisms at work and their potential to deliver practical solutions. In its basic form, MEL is akin to a double degree-of-freedom liner implementing a membrane as septum in lieu of a typical wire mesh. Introducing the membrane provides a thin structural element whose resonance can be tuned to interact with acoustic resonances to enhance absorption bandwidth for the 500-1000 Hz range. Material, geometry, tension, and location of membrane are used as tunable parameters. It is found that by increasing the height of the acoustic cavity below the membrane, the absorption peaks are shifted to lower frequencies. Further, non-uniform cavity geometries allow the creation of multiple absorption peaks for a single membrane tensioning. MEL variants using perforated or mass-loaded membranes and slanted cores are found to provide additional tunability. The experimental results correlated well with COMSOL simulations. FCL utilizes 3D folded cavity cores to pack long acoustic paths into a compact space, thereby generating lower frequency absorption for a given liner volume. A Zwikker-Kosten Transmission Line (ZKTL)-based methodology was used to optimize designs for tonal and broadband low-frequency spectra. Experiments show that absorption peaks below 500 Hz can be engineered within a 1.27 cm thick FCL sample. Finally, CFL configurations employing various carbon foams suitable for multifunctional applications are studied. The influence of parameters such as foam type, thickness, spacing (air gap), and membrane-interaction are evaluated using experiments and simulations. Tailoring the spacing between the foam samples was found to significantly (>~50%) improve mid-range absorption. A low-frequency absorption peak is obtained in the vicinity of the natural frequency (~600 Hz) of the tensioned membrane embedded within the CFL sample, indicating the potential of combining carbon foam-based acoustic bulk absorbers with structurally resonant elements such as the tensioned membrane to bolster low-frequency absorption. Successful transition of these low-frequency liner concepts to applications such as in the aerospace domain could potentially deliver solutions that are congruent with evolving regulatory requirements as well as technological innovations.

Table of Contents

Chapter   Page

LIST OF TABLES

LIST OF FIGURES

LIST OF SYMBOLS AND ABBREVIATIONS

2DOF	2-Degree of Freedom
α	Absorption Coefficient
a, b	Side Length
a	Parameter
b	Fitting Parameter
c_o	Speed of Sound in Air
c_m	Speed of Sound in Membrane
CF	Carbon Foam
d	Resonator Neck Diameter
d_c	Cavity Diameter
d_1, d_2	Thicknesses of Test Samples
d_s	Thickness of Arbitrary Test Sample
ε_p	Porosity
f	Frequency
f_{mn}	Modal Frequency
FAA	Federal Aviation Administration
FCL	Folded-Cavity Liner
g	Acceleration Due to Gravity
Γ	Propagation Constant
Γ_r	Attenuation Rate
Γ_i	Phase Rate

H	Total Liner Height
H_r	Hydraulic Radius
J_0, J_1	Bessel Number of the First and Second Kind
K	Bulk Modulus
K_{bar}	Reduced Frequency
k	Coefficient of Thermal Expansion
L	Length (or Length of the Neck)
L_R	Length of Rectangular Cell
m, n	Mode Numbers in Principal Directions
m_t	Membrane Tensioning Mass
MEL	Membrane-Embedded Liner
MDOF	Multiple-Degree of Freedom
NPDC	New Product Development Center
NIT	Normal Incidence Tube
NUL	Non-Uniform Liner
ORNL	Oak Ridge National Laboratory
ρ_o	Density of Air
ρ_f	Density of Fluid
ρ_m	Density of Membrane
ρ_{rig}	Density of Rigid Frame
p_A	Ambient Pressure
POHC	Perforate Over Honeycomb
Pr	Prandtl Number
R_f	Flow Resistivity
R	Acoustic Resistance

s	Shear Wave Number (Stokes Number)
s'	Anisotropy Factor
S	Cross-Sectional Area of the Neck
S_{LS}	Side Length of Large Square Cell
S_{SS}	Side Length of Small Square Cell
SDOF	Single-Degree of Freedom
σ	Square Root of Prandtl Number
σ_f	Flow Resistance
t_m	Membrane Thickness
τ_{∞}	Tortuosity
γ	Ratio of Specific Heats
μ	Dynamic Viscosity
V	Internal Cavity Volume
W	Width
Wo	Womersley Number
W_R	Width of Rectangular Cell
ω	Angular Frequency
X	Acoustic Reactance
ζ_1, ζ_2	Surface Impedance for Two Test Samples
ζ_c	Characteristic Surface Impedance
ZKTL	Zwikker-Kosten Transmission Line

CHAPTER I

Introduction

1.1. Background and Motivation

Low-frequency airborne noise contains the ability to have detrimental effects in many aero structural applications. This type of spectral content can enable structural vibrations resulting in premature fatigue that leads to structural failure. Low-frequency noise stemming from aircraft causes discomfort to the communities which surround airports as well as the commercial passengers, leading to potential hearing loss or in some extreme cases psychological problems. This has resulted in the Federal Aviation Administration (FAA) imposing very strict noise emission regulations on airline companies [1].

An acoustic liner, in general, is a honeycomb structure used to mitigate noise radiated by aircraft engines. There are four main classes of acoustic liners: locally reacting, non-locally reacting, passive, and active liners. Locally reacting liners are those that rely on a resonance type response for its means of acoustic absorption. Non-locally reacting liners are bulk absorbers such as foam or fiberglass. The non-locally reacting liner takes advantage of tortuous paths comprised within the material to absorb sound. Passive liners can be either locally or non-locally reacting, most commonly they are manufactured to absorb a particular frequency or range of frequencies in any environment. Active liners can typically adapt to an environmental change to better mitigate a targeted noise spectrum.

There are two main types of sound absorbers found on aircraft, bulk absorbers like fiberglass or foam are typically used as the sound-absorbing treatment for the fuselage, and acoustic liners which consist of an aluminum or Nomex honeycomb sandwich panel located on the inlet and aft of the nacelle. The dimensions and material properties of the acoustic liner determine the range of frequencies in which the liner can absorb sound. For example, a liner that contains a thick liner can absorb lower frequencies, but a very thin liner will absorb higher frequencies. This is only one of the tunable parameters one can use in attempts to mitigate low-frequency noise (<1000 Hz), which is difficult without adding an extensive amount of weight or thickness. Not only does this result in a penalty of weight but also a penalty on the fuel burn due to the added mass and thickness.

Before designing an acoustic liner for an aircraft engine is it important to understand the underlying noise sources. In the past, aircraft engine pollution consisted of mid to high-frequency tonal content. However more recently ultra-high bypass ratio engines have been implemented for their advantages in thrust and efficiency. These types of engines produce low-frequency broadband content, of which the legacy engine liners are predominately ineffective. Thus, the noise content targeted in this thesis is low-frequency broadband noise produced by commercial aircraft. The main sources of noise produced by aircraft are engine turbofan noise, jet exhaust noise, and airframe noise. On take-off, the dominant noise sources are engine turbofan noise and jet exhaust noise, and during landing the turbofan, landing gear, airframe noise.
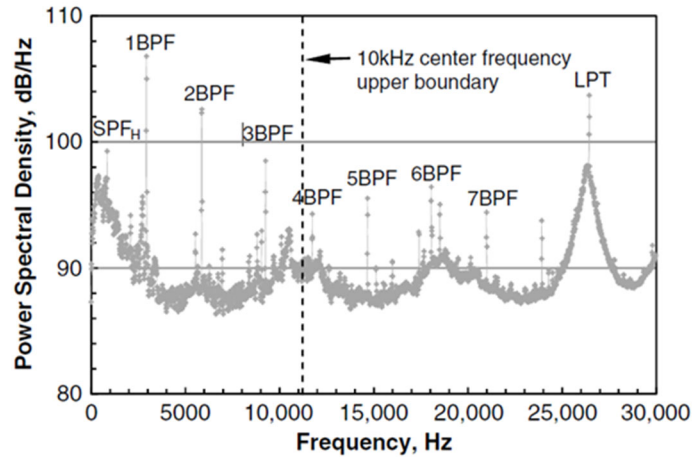
Figure 1: Power spectral densities for the NASA Glenn DGEN turbofan at 118 degrees from the inlet axis, operating at 96% of the maximum low-spool shaft speed

Figure 1 shows the noise content produced by the DGEN 380, which is a twin-spool, unboosted, separate-flow, geared turbofan manufactured by Price Induction, Inc. and has a static thrust of up to 570 lb at sea level [2]. These engines are primarily used for small twinjet applications such as the Williams International FJ33 and the Pratt and Whitney PW600.

When designing an acoustic liner concept, the feasibility of manufacturing must be taken into account. Thanks to the advent of additive manufacturing and alternative manufacturing techniques, novel liner concepts that were previously not considered, can now be evaluated for their acoustical feasibility in the aerospace industry. One of these liner concepts can be the key to unlock a new era of ultra-compact engine liners that can drive the future of acoustic footprint made by the commercial aircraft industry. Over the past couple of years, strides in passive acoustic liner technology have been made by NASA Langley Research Center by embedding mesh caps of a particular resistance value within the liner cavity to create a multiple degree of freedom liner concept [3, 4]. This design concept was implemented in a Boeing flight test in 2019 and resulted in noise reduction of between 4-8 dB at various flight settings [5]. This type of liner is designed by NASA Langley and fabricated Hexcel Corporation [6].

In the 1960s noise pollution increases and the United States declares that it is a significant environmental issue that needs to be addressed. Noise pollution, if not handled properly, could grow to a point where it endangers the health and wellbeing of the citizens of the United States, thus the Noise Control Act of 1972 was developed [7]. This federal act served with the intent to protect human health and minimizing the annoyance of noise to the general public. It established a mechanism to set emission standards for virtually every noise source, including aircraft. Engineers began experimenting with viable noise reduction and noise control techniques. In 1970, Mangiarotty was one of the first to classify different types of acoustic liners as a solution to the aircraft engine noise emission problem [8] and concluded that there were three basic types of acoustic lining suitable for acoustically treated engine ducts, the absorber type, the resonator type, and an absorber/resonator combination type.

Within this thesis, there are three different lightweight compact acoustic liner concepts investigated and tested for feasibility of use in the aerospace community or alike. First is a membrane-embedded acoustic liner that utilizes a nonrigid element as the primary source of noise attenuation. Next is a folded cavity liner concept, which essentially implements a series of long cavities folded together to create a compact, realistic, design configuration using aerospace-grade materials. Lastly, a non-graphitized carbon foam is investigated for its acoustic properties and then coupled with a membrane, similar to the first concept, which aims to combine the favorable acoustic properties of bulk materials with the low-frequency noise mitigation potential of a nonrigid element. Each of these concepts is discussed in more detail later in this chapter.

1.2. Literature Review

Back in the 1940s, community noise complaints started to increase and in the 1950s the NACA Glenn Center's acoustics research began using the Altitude Wind Tunnel and several full-scale

engine test stands to evaluate nozzle suppressors [9]. In the 1960s after Glenn became part of NASA, they began focusing on developing quieter engines and engines for short takeoff and landing. Because the noise complaints kept coming, in 1969 the FAA introduced regulations to limit aircraft noise pollution. Over the years these regulations have tightened up, and the noise threshold in which an aircraft could depart or return to an airport around communities became much more difficult to achieve.

In the 18th century the mathematician Taylor began to develop a mathematical theory for a vibrating string, with the basis of his mathematical solutions based on the theory of calculus which was developed by Newton and Leibniz [10]. Then in the mid-1700s, d'Alembert [11] derived the general solution for the wave equation. In the 19th century, the most important development is that of the vibrating plate and standing wave patterns. This development is brought by Chladni [12], known as the father of acoustics, and his most famous contribution to acoustics is called the Chladni plate experiment. The theory behind this is that given a square, rectangular, round, or some other type of flat plate that is secured in the middle, that when the plate is given some sort of excitation, some parts will vibrate and some parts will not. So, using dust or sand the plate will move the material to parts of the plate that are not vibrating. The frequencies in which the plate vibrates are called the natural frequencies, and all objects, including these Chladni plates, have multiple sets of natural frequencies or eigenfrequencies. This concept essentially allowed everyone to be able to visualize sound in a different way.
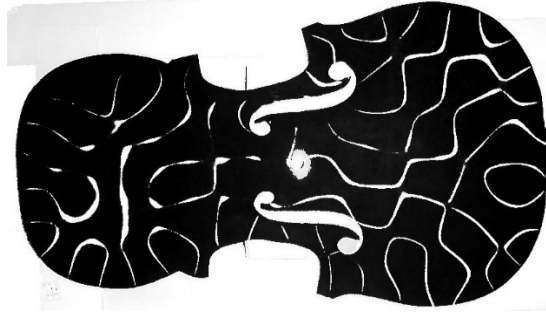
Figure 2: A photograph of a violin-shaped aluminum Chladni plate showing a Chladni pattern. (Image by Stephen Morris — Own work. Licensed under CC BY 2.0, via Flickr.)

Other significant contributors to the modern advances in acoustics are Helmholtz, Lord Rayleigh, and Kirchhoff. Helmholtz [13, 14] made significant contributions to understanding the mechanisms of hearing and in the psychophysics of sound and music. He came up with a mathematical formulation to describe the sound vibration of cylindrical tubes. In doing so, Helmholtz created a device, now called the Helmholtz resonator. This device is constructed so that one end would go in your ear and the other is open to a source, and if the sound frequency did not match that of the device, then the sound is muffled (see Figure 3) [15].

Figure 3: Helmholtz resonator, top inserted in-ear, bottom open to a sound source [15]

Rayleigh conducted an enormous amount of acoustics research and a good amount of it was published in his two-volume publications of the Theory of Sound [16]. Moving forward, Kirchhoff [17] made great advances based on Helmholtz's work to include thermal and viscous effects. Using a complex transcendental equation, Kirchhoff was able to develop an approximate

6

formulation that holds true for "wide" tubes, in which viscous dissipation becomes negligible. To make considerations for more narrow regions where the viscous losses cannot be ignored, in 1896, Lord Rayleigh developed an approximate solution for "narrow" tubes. After a critical examination of Kirchhoff's and Rayleigh's work, Weston [18] split up the problem into three different areas which separated 'narrow tubes', 'wide tubes', and 'very wide tubes'. Then in 1957, Zwikker and Kosten were able to derive analytical solutions to the simplified basic equations for the low-reduced-frequency case [19]. The solutions developed for the first time by Zwikker and Kosten, illustrate sound propagation through a cylindrical tube, as long as the low-reduced-frequency criteria (K_{bar}<<1 and K_{bar}/s<<1) is satisfied. The low-reduced-frequency case is valid for the designs discussed in parts of this study, so the solution obtained by Zwikker and Kosten was used to numerically predict liner performance.

About two decades later, Tijdeman [20] described the early solution approaches for the propagation of sound in gases (such as air) which are confined within a cylindrical tube, and determined that the solution was primarily governed by the propagation constant Γ. By rewriting the propagation constant in terms of the shear wave number and the reduced frequency, yields a simplified model to easily compare various solutions. As it turns out, he also determined that the problem of sound propagation through cylindrical tubes is governed by four parameters, the shear wave number (s), the reduced frequency (K_{bar}), the square root of the Prandtl number (σ), and the ratio of specific heats (γ).

Additionally, Zwikker and Kosten came up with one of the earliest models to describe porous materials constructed of a rigid frame [19]. The model was primarily defined by the complex density and bulk modulus

$$\rho_{rig} = \frac{\rho_f}{\varepsilon_p} \frac{1}{1 - \frac{2}{W_o\sqrt{-i}} \frac{J_1(W_o\sqrt{-i})}{J_0(W_o\sqrt{-i})}} \qquad Eq.\ 1.1$$

$$W_o = \sqrt{\frac{\omega \rho_f H_r^2}{\mu}}$$

$$\text{Eq. 1.2}$$

Where H_r is the hydraulic radius of the pores and W_o is the Womersley number. W_o is related to the ratio between viscous penetration depth and the hydraulic radius. ρ_f is the fluid density, J_0 and J_1 are the Bessel function of the first and second kind. The bulk modulus is given by

$$K = \frac{\gamma p_A}{\varepsilon_P} \frac{1}{1 + (\gamma - 1) \frac{2}{W_o \sqrt{-iPr}} \frac{J_1(W_o \sqrt{-iPr})}{J_0(W_o \sqrt{-iPr})}}$$

$$\text{Eq. 1.3}$$

$$\text{Pr} = \frac{C_p \mu}{k}$$

$$\text{Eq. 1.4}$$

Where p_A is the ambient pressure, Pr is the Prandtl number, μ is the dynamic viscosity and k is the coefficient of thermal expansion, γ is the ratio of specific heats. The combination of γp_A is the isentropic bulk modulus. This leaves the free parameters to describe the pores for this model to be the ε_p, the porosity, and the hydraulic radius.

As a continuation of Zwikker and Kosten's work, Keith Attenborough's porous media model is based on a cylindrical pore assumption and is a four-parameter semi-empirical model [21, 22]. This adds two more parameters, tortuosity (τ_∞) which accounts for the upper-frequency limit and is related to the orientation of pores relative to the propagation direction. The hydraulic diameter is replaced by an expression that includes the flow resistivity (R_f) and a fitting parameter (b) which is related to the anisotropy of the pores. The expression for the equivalent density of the rigid frame is altered slightly from the previous model to be the following expression.

$$\rho_{rig} = \frac{\rho_f}{\varepsilon_p} \frac{\tau_\infty}{1 - \frac{2}{s' \sqrt{-i}} \frac{J_1(s' \sqrt{-i})}{J_0(s' \sqrt{-i})}}$$

$$\text{Eq. 1.5}$$

$$= \frac{\gamma p_A}{\varepsilon_P} \frac{1}{1 + (\gamma - 1)\frac{2}{s'\sqrt{Pr}}\frac{J_1(s'\sqrt{Pr}\sqrt{-i})}{J_0(s'\sqrt{Pr}\sqrt{-i})}} \qquad Eq.\ 1.6$$

Where in this case s' is the anisotropy factor which is derived from various material parameters and related to the Womersley number.

$$s' = b\sqrt{\frac{8\omega\rho_f\tau_\infty}{\varepsilon_P R_f}} \qquad Eq.\ 1.7$$

The four free parameters needed are the porosity, the flow resistivity, the tortuosity, and the fitting parameter.

In the 1970s, Delany and Bazley [23] published their work related to the acoustics of fibrous absorbent materials such as porous open-cell foams. In general, the propagation of sound in isotropic homogeneous materials can be realized by the characteristic impedance and the propagation coefficient. Considering only plane wave propagation, they used the specific flow-resistance per unit thickness for the assessment which depends on the bulk density of the sample and the fiber size. They deduced that since most manufacturers do not publish data on the flow-resistance of their materials, it can be closely approximated by a simple power law equation. For the normalized real component of the characteristic impedance,

$$\frac{R}{\rho_o c_o} = 1 + 9.08 * \left(\frac{f}{\sigma_f}\right)^{-0.75} \qquad Eq.\ 1.8$$

Where R is the resistive component, $\rho_o c_o$ is the characteristic impedance of air, f is the frequency and σ_f is the flow resistance. For the imaginary component, we have,

$$\frac{X}{\rho_o c_o} = -11.9 * \left(\frac{f}{\sigma_f}\right)^{-0.73} \qquad Eq.\ 1.9$$

Where X is the imaginary component of the characteristic impedance.

For the absorption coefficient,

$$\alpha = 10.3 * \frac{\omega}{c_o}\left(\frac{f}{\sigma_f}\right)^{-0.59} \qquad Eq.\ 1.10$$

The propagation coefficient is given by,

$$\Gamma = \frac{\omega}{c_o}\left[1 + 10.8 * \left(\frac{f}{\sigma_f}\right)^{-0.70}\right] \qquad Eq.\ 1.11$$

The formulation of the sets of data presented by Delany and Bazley gives a good approximation for the theoretical and experimental values for the empirical flow resistance for various fibrous absorbents.

Switching gears away from bulk absorbers, in the late 1970s, NASA Lewis Research Center (presently known as NASA Glenn Research Center) began research on various mechanisms and theories related to fan noise reduction concepts [24]. This study consisted of investigating engines like the JT9D (the first high bypass ratio jet engine) as well as the CF6 and the RB211, where the noise produced by the fan stage is dominant. At the time some of the engine noise reduction concepts considered were eliminating the inlet guide vanes, altering the axial spacing between the rotor and stator, and specifically choosing the rotor-blade and stator-vane number to induce a cutoff of blade-passage tone according to Tyler-Sofrin cutoff theory [25]. Incorporating an of these typically resulted in a 3-6 dB reduction in noise. But the newer noise reduction concepts that were investigated consisted of a perforate-over-honeycomb as the inlet treatment, and for the exhaust duct utilized a multiple-degree-of-freedom design and a bulk absorbing material. Various other concepts are investigated in this paper, but for the sake of brevity are excluded. These designs were primarily chosen to suppress the turbine blade-passing frequency noise. It should also be noted that this investigation provided data supporting both, engine fans with subsonic tip speeds, as well as supersonic tip speeds.

Perforate-over-honeycomb (POHC) liners are typically found in the inlet of the engine nacelle around the outer walls as well as in the aft around the outer nacelle walls as well as around the engine core (see Figure 4).
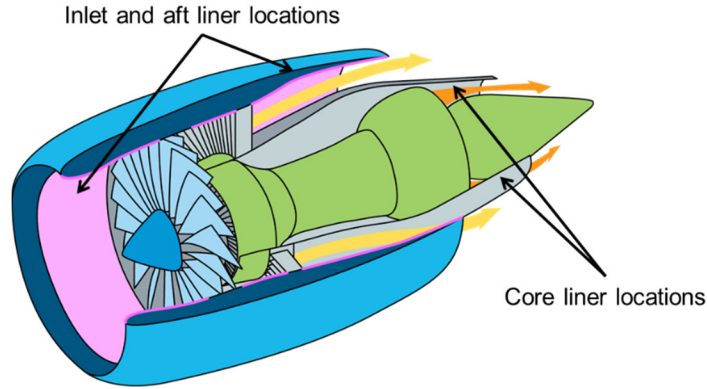
Figure 4: Liner locations on a typical turban engine [65]

These designs work by enabling the use of the POHC resonant frequency of the single-degree-of-freedom (SDOF) liner as the primary absorptive mechanism, but more recently with the use of a wire mesh septum embedded within the liner cavity. The addition of the resistive element inside the cavity creates more broadband absorption effects within the 2-degree-of-freedom (2DOF) liner. A comparison between a SDOF and a 2DOF liner is shown in Figure 5 [26].
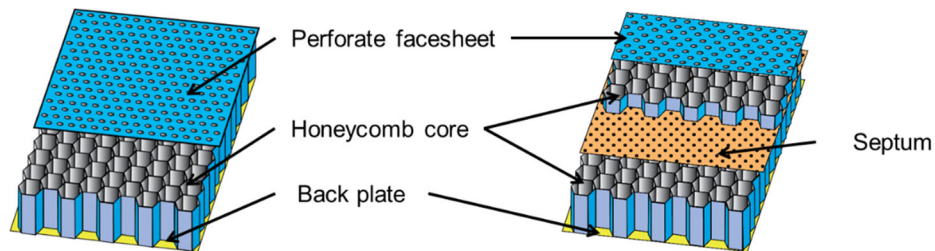
Figure 5: Comparison of a SDOF (left) and a 2DOF (right) liner configuration [26]

The absorption mechanism of a SDOF liner is resonant based and utilizes the Helmholtz resonance to mitigate noise at target frequencies. This method can be used to tune the liner for a

specific frequency or a range of frequencies by means of modifying various dimensional

parameters. A Helmholtz resonator can be represented as the most basic form of a SDOF spring-

mass system.
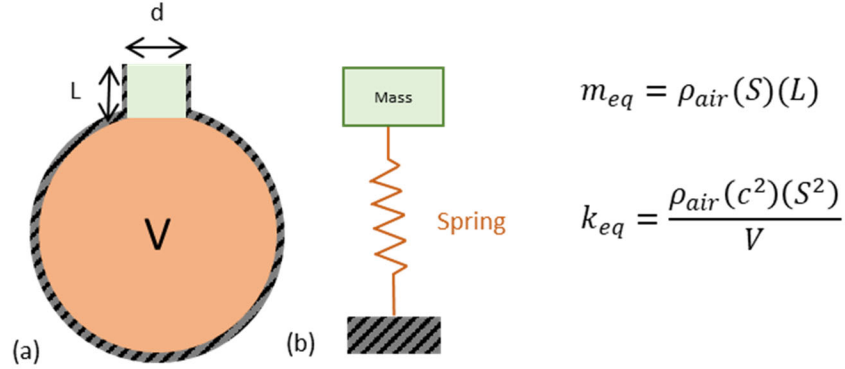
Figure 6: (a) Sketch of a trivial Helmholtz resonator and (b) an equivalent mass-spring system

In the example shown above, the air trapped within the neck (shaded in green) acts as the mass,

while the air trapped within the cavity (shaded in orange) acts as the spring. The frequency for

which this system will resonate is given by

$$f = \frac{c}{2\pi}\sqrt{\frac{S}{VL'}}$$

Eq. 1.12

Where c is the speed of sound in air, S is the cross-sectional area of the neck, V is the entrapped

volume of air inside the cavity, and L' is the effective length of the neck. L' contains an end

correction factor which accounts for the effects of the lip of the open cavity moving in

conjunction with the mass of entrapped air within the neck [27].

$$L' = L + 0.48 * S^2 \left(1 - 1.25\frac{d}{d_c}\right)$$

Eq. 1.13

Where the d is the diameter of the resonator neck, and d_c is the diameter of the cavity. This end

correction is valid for $\frac{d}{d_c} < 0.4$, and if this criteria is not satisfied, another end correction will be

required. Together, these equations make it possible to realize why low-frequency noise

mitigation is difficult to achieve. The main tuning mechanism utilized in a Helmholtz resonator is the volume of air entrapped within the cavity, increasing that volume makes it possible to resonate at low frequencies but comes with a penalty, weight and footprint of the liner within a nacelle.

1.3. Lightweight, Low-Frequency Liner Concepts

Over the past decade, there have been numerous attempts in novel acoustic liner designs with the aim to target the absorption of low-frequency noise mitigation. These designs range from liners that utilize a compact form factor, to a new species of liner which contains non-rigid materials that may lead to broadband noise mitigation. For instance, Ma [26] discusses various tunable concepts containing both rigid and nonrigid elements. This design consists of a rigid backplate and perforate facesheet, but the interior walls of the liner contain both rigid walls as well as a flexible damping wall. This configuration contains many manufacturing complexities, but in time, this concept may show enough benefit to justify the capital to produce it on a large scale. Naify et al. [28] investigates transmission loss of membrane-type acoustic metamaterials based on the mass law. They demonstrated that low-frequency sound insulation is possible across a narrow frequency range and can be tuned to a desired frequency. Additionally, Naify [29] investigated some 2DOF configurations using an acoustic mesh as septum to display increased transmission loss at low frequencies. On a much larger scale, Ang et al. [30] investigates plate-type acoustic metamaterials in attempts to attain low-frequency noise mitigation in a more urban environment around traffic and construction. They demonstrate that the various meta-panels in question were in fact viable for low-frequency noise control (80 Hz – 500 Hz). This is but another of many industrial applications which should be considered for similar noise control technology in the future. Lam et al. [31] investigates an elastic panel liner with a backed cavity configuration (changing the modifying the shape of the backing cavity beneath the facesheet) in the presence of

grazing flow, they conclude that the cavity size modifies the acoustic distribution within the cavity and thus the acoustic radiation by the panel. By modifying the acoustic distribution within the cavity by introducing an absorptive material at the reflective end of the cavity, greater absorption and less reflection than in the ordinary counterpart are achieved. Huang et al. [32] looks at a metaliner configuration where a perforated plate and a metasurface consisting of neck-embedded Helmholtz resonators is used to achieve efficient broadband impedance modulation. They verify this metaliner configuration experimentally and show high-efficiency and broadband sound attenuation performance under a grazing flow environment.

Another novel liner design is that of the reactive or resonant type with several modes of vibration excitable within a complex system of thin metal or plastic membranes. This liner type, proposed by Ackermann et al. [33], gets the vibrational energy from stimulated sound waves impinging on the acoustic lining brought about solely by frictional forces in bounded shear layers formed between spherically shaped membranes moving against one another and relative to the air volumes contained around them. The all-metal membrane construction proposed combines a baffled resonator with a Helmholtz resonator into a broadband membrane absorber without using any other sound-absorbing material. One example of this is provided in Figure 7 below.
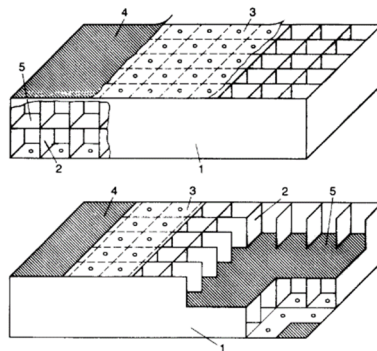
Figure 7: Ackermann Liner, 1, the frame of the splitter; 2, walls of the chambers; 3, perforated membrane; 4, covering membrane; 5, bearing plate [33]

This design can be understood in a conventional sense because the construction is similar to a strong spring-mass reactance created by the enclosed air cushion as the spring and the two

membranes as masses. This particular design shows very strong indications of good low-frequency broadband performance from just below 200 Hz to just below 400 Hz which is optimized for transmission loss. As what seems to be a follow-up to Ackermann's work, Frommhold [34] took a similar approach to the design for a low-frequency liner concept. This design consisted of a cylindrical tube with a length of 12 cm, a diameter of 10 cm, and a flexible perforated membrane glued to the surface of the cavity. The membrane had a thickness of 0.02 mm and had a peak resonance frequency of around 200 Hz. Analytical lumped element models for the acoustic response for this configuration were investigated here but did not yield sufficient agreement to claim strong accuracy when compared to experiments.

Acoustic metamaterial designs are another class is novel liner designs aimed at low-frequency sound absorption. One of these metamaterial designs was thought of by Fan et al. [35] which featured a stacked membrane coated perforated plate. This design showed promise for low-frequency mitigation but due to manufacturing complexities, only theoretical analysis and finite element simulations were investigated. Ma et al. [36] showed that a membrane-type acoustic metamaterial could actually reach noise mitigation below 500 Hz in practice. The proposed design utilizes four local resonators which are constructed using 0.2 mm thick latex rubber and had a radius of 12 mm. Affixed to the center of each membrane is a 70 mg circular disk, this disk allows the membrane to resonate at a lower frequency. Although this design was developed for a transmission loss application, it displayed a unique concept for low-frequency noise reduction technology. This particular configuration is shown in Figure 8 below.
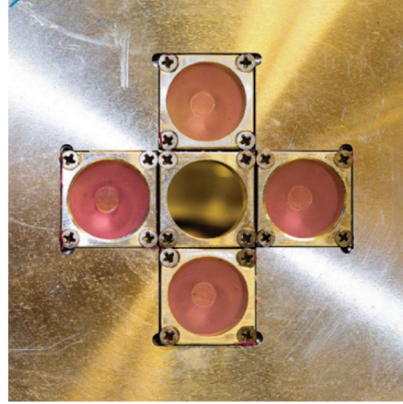
Figure 8: Membrane-embedded metamaterial absorber developed by Ma [36]

Huang et al. [37] discuss a similar design with the majority of their designs incorporating a mass attached membrane-type acoustic metamaterial. Deducing that the membrane performance is very sensitive to the tension, which is difficult to control and sustain over a long period of time. Another research project by Sui et al. [38] shows a configuration more closely related to one presented in this paper and will be talked about in more detail in Chapter 2. This design consists of a no-mass-attached membrane sandwiched between two honeycomb panels. Similarly, to the previous two cases discussed, Sui et al. is concerned with the sound transmission loss of this membrane-embedded acoustic metamaterial. As so, the results indicate excellent performance for a no-mass-attached membrane-type acoustic metamaterial at low frequencies. A similar concept using active noise control to tune a membrane-type acoustic metamaterial by altering its properties by applying an electric charge to achieve a negative mass density [39]. The result in this area of noise control could lead to a new series of low-frequency absorbing, ultra-compact acoustic metamaterials.

A theoretical model for a membrane is explored by Chen et al. [40] considering a simple unit cell of both a no-mass-attached and a mass-attached membrane. An exploration of the eigenvalue problem is considered to determine the natural frequencies of these special cases. Additionally, a vibroacoustic model was developed using COMSOL Multiphysics used as a validation of their

current model. A set of photos from the simulations are shown in the figure below for the mass-attached theoretical model.
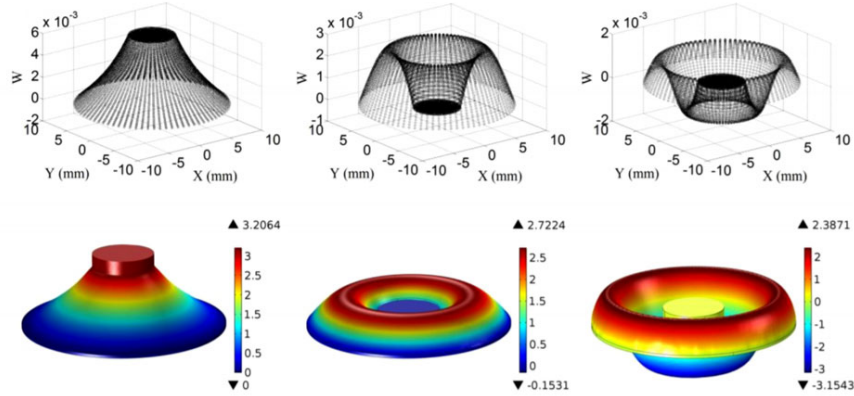
Figure 9: Mode shapes for the mass attached membrane's analytical solution (top) and COMSOL solution (bottom) developed by Chen et al. [40]

The results presented show very good correlation between the theory and the finite element model. Palma et al. [41] discusses a concept involving a membrane decorated with one or more resonant masses. The physical mechanism at play involves two parameters, ρ (the mass density) and κ (the bulk modulus), and by forcing one of these two parameters negative, one can obtain near-total reflection. Although this is not a desired acoustic characteristic for sound absorption, however, this is but one example of the characterization of mass attached resonators and this demonstrates the ability to be able to tune the reflections to minimize the overall sound signature of a source. To follow up, Langfeldt et al. [42] investigated inflated single and double membrane-type acoustic metamaterials by modifying the effective mass. By exploiting the geometrical stiffening which occurs naturally in a stacked configuration, an investigation adjusting the pressure backing the membrane to modify the eigenmodes and transmission loss of the overall configuration. Theoretical models using numerical and analytical models were used to identify the mechanisms responsible for the bulk of the modal shifting, experimental tests were conducted using an impedance tube that displays direct correlation with the theoretical model.

An alternative method in obtaining low-frequency performance is investigated by Guo et al. [43] looking at Helmholtz resonators with extended necks. Using a conventional Helmholtz resonator design and extending the neck inside the liner cavity has shown to result in a lower-frequency absorption peak than a conventional design. The liner design proposed contained a series of cavies with different extended neck lengths resulting in resonant frequencies which range from ~700 Hz – 1000 Hz, which was theoretically and experimentally verified.
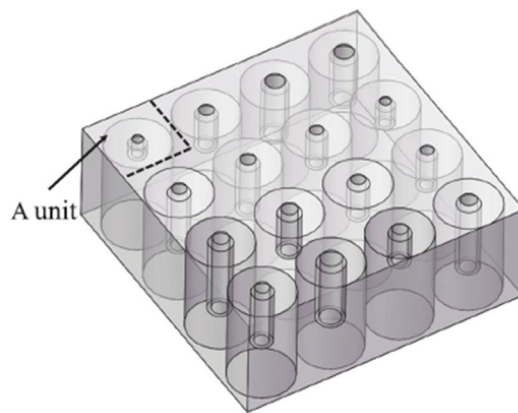
Figure 10: Acoustic liner concept developed by Guo et al. using acoustic liners with extending necks [43]

Using a shape memory alloy as a facesheet, the porosity can be altered or even seal off holes entirely, if desired [44]. This process uses a three-layer configuration with the middle layer having the ability to slide with respect to the top and bottom layer using a super elastic wire for actuating and generate a restoring force. A variety of liner concepts were produced and tested in the NASA Langley Grazing Flow Impedance Tube, with promising results and a proof of concept achieved. They demonstrated that by using this concept, better attenuating blade passage frequency tones through slight adjustments within the facesheet can be achieved. In a similar study, using a flexible foil combined with a rigid core structure as the honeycomb liner is discussed but to make up for the non-rigidity of the flexible foil may lead to concerns with the overall structural rigidity compared to conventional honeycomb design structures [45].

Determining the optimal cavity shape for an acoustic liner based on the Helmholtz equation including visco-thermal losses that target a specific frequency range was investigated by Tissot et al. [46] and by optimizing the cavity shape they claim to obtain perfect absorption. Using finite elements, an optimization was conducted to obtain the perfect impedance. The downside of this design is that the focus frequency range is very narrowband, so after the optimization, the perfect absorption was obtained but only for around a hundred Hz or less.

As the need for low-frequency absorbers increases, as does the creativity of researchers aimed at attacking this problem. A cavity that is at least 25.4 cm in depth is required to achieve a peak resonance below 500 Hz in a conventional Helmholtz resonator. However, due to space limitations in an aircraft engine nacelle, this is impractical. Yu et al. [47] attempts to attack this problem by considering an eight-chamber folding cavity Helmholtz resonator to provide the required cavity depth to mitigate noise at such a low frequency. Chambers et al. [48] attacked this design concept from a different direction. Using the convenience of 3D prototyping to his advantage, he designed (using Zwikker and Kosten's transmission line method) printed various liner concepts that demonstrated broadband absorption at frequencies well under 500 Hz with a total thickness of 3.969 cm. Chambers went a step further by developing a program that, given a set of parameters, would determine the most efficient way to pack 3D folded cavities into a given volume.
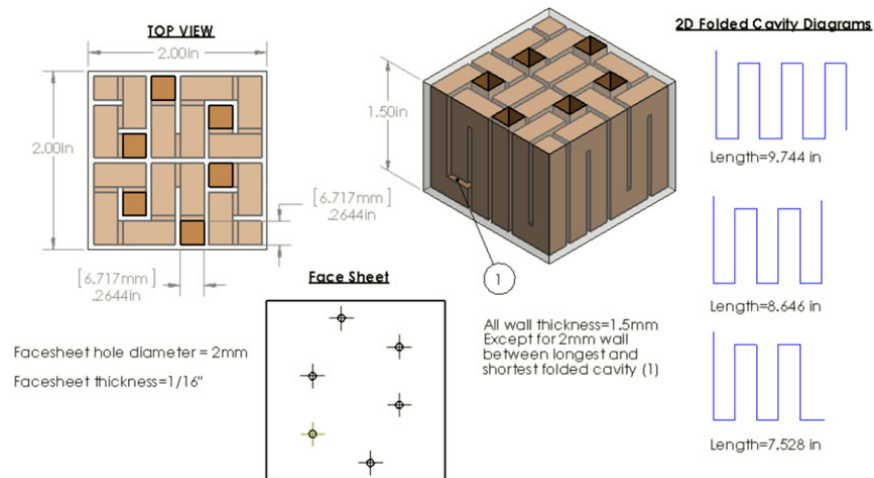
Figure 11: Folded-cavity liner concept developed by Chambers [48]

A similar design concept was investigated by the folks at NASA Langley where they investigated a variable depth liner concept and its effects on the impedance with and without the presence of grazing flow [49]. They concluded that their predictions were most favorable compared to the experiment with the presence of flow, but at Mach 0.0 were less favorable. Another folded-cavity packing optimization code was developed at NASA Langley with a similar purpose in mind as Chambers, the basis for this code is by using a randomized trial and error approach to place each cavity in a representation of the liner sample until the code found a match [50].

As discussed earlier in the literature review, foams are typically known for their bulk properties as well as their broadband attenuation characteristics. Various investigations have been done over the recent years to determine the feasibility of using rigid foams as a source of aircraft engine noise reduction. In particular, these types of liners have been evaluated for use over the rotor and have shown significant acoustic performance of up to 4 dB [51]. Sutliff and Jones [52] attacked this problem by first determining the acoustic characteristics using the Normal Incidence Tube at NASA Langley and then designing a foam-metal liner based on the known acoustic character of a low-speed fan.

Figure 12: Foam metal liner (developed by Sutliff and Jones) installed in an engine test stand [49]

This investigation was continued by combining the foam-metal liners placed over the rotor with soft vanes. Soft vanes are fan exit guide vanes with a porous surface that enables some relief to the pressure fluctuations at the vane surface and the resonant chambers below. The result of the soft vane concept allowed for a 1 to 2 dB fan noise reduction.

When considering an open-cell foam for its acoustic properties, knowing the parameters required to model the foam is critical [53]. Duan et al. [54] studied the effects of a sintered porous ceramic material called zeolite, more concerned with the material properties of the porous foam, they observed an absorption peak around 1000 Hz in a test sample which was 2.8 cm in thickness. Comparing the experiment with theoretical models to evaluate the acoustic performance, this sintered material was best modeled with the Johnson-Allard model. The properties of open-cell foams can be characterized in two ways, by determining the macroscopic properties such as the relative density and Young's modulus [55]. Alternatively, using the microscopic properties, such as pore size, in order to characterize an open-cell foam can potentially lead to a better understanding of a particular mechanism required for sound absorption [56]. In the late 1960s, Oak Ridge National Laboratory (ORNL) developed the first dedicated process to produce foams with a certain structure and material properties [57]. Now, ORNL has a patented process for

making what they now call Carbon-Graphite foam [58]. Gaeta [59] conducted an investigation

attempting to characterize the effect of the bulk acoustic properties, looking at the effect of

density, metallic coating, and bulk temperature on the sound absorption performance.
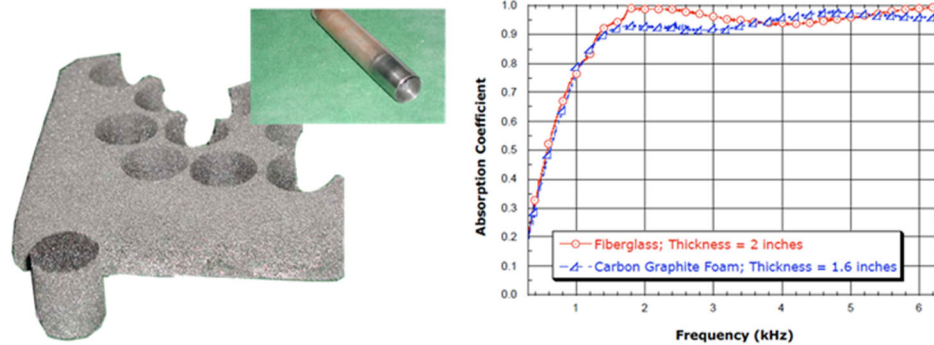
Figure 13: Carbon graphite foam as tested by Gaeta (left) and the acoustic performance of the carbon graphite foam compared with fiberglass (right) [59]

He determined that the temperature does not significantly affect the sound absorption and that the

Carbon-Graphite foam is an excellent sound absorber above 1000 Hz with absorption coefficients

ranging from 0.8 to 0.9.

1.3.1. Membrane-Embedded Liner

The first acoustic liner considered in this paper is a Multiple Degrees of Freedom Liner (MDOF)

by means of an elastic membrane sandwiched between two pieces of honeycomb. This type of

liner is unique because typically the materials used in an acoustic liner are all rigid but in this

case, the membrane is a non-rigid material that introduces n-number of natural frequencies. This

feature enables these multiple natural frequencies to attenuate broadband noise more efficiently.

Additionally, because the membrane is a flexible structure that resembles a drumhead, it may be

tuned to absorb numerous frequencies. Another advantageous artifact for this particular MDOF

liner design is that the membrane may allow for a much more compact engine liner that mitigates

low-frequency broadband noise better than traditional liners.

This type of MDOF liner configuration is not a new thought up design, however, from the literature it appears that there is a lack of data that experimentally test such a nonrigid material, not only embedded within a liner but which also investigate effects on the acoustic response in relation to the location of a nonrigid element within the liner cavity; and also which modify the nonrigid element geometry as well as the cavity geometry in order to obtain a desired acoustic response. Chapter 2 aims to alleviate this lapse in experimental testing and data of the aforementioned cases.

1.3.2. Folded-Cavity Liner

The folded cavity liner concept is the next configuration investigated in this thesis as a continuation of the work presented by Chambers. To follow up with the dozens of validated tests conducted between 2016-2018 by Chambers using 3D printed materials, the next step is to manufacture this type of liner out of aerospace-grade materials. This proof of concept could potentially enable the liner community and aerospace industry to take this technology to the next level and hopefully begin manufacturing and testing the folded cavity liner concept within a live engine nacelle. This follow-up and progression of this concept led to the design, manufacturing, and testing of a folded cavity liner which targets and achieves a specific frequency range designed for a specific low-frequency performance factor.

1.3.3. Carbon Foam Liner

Lastly, an investigation into a carbon foam and a membrane-embedded carbon foam is considered. Although acoustic performance of carbon foams and other rigid open-cell foams is not a new concept, there are many different types of rigid foam out there that have not been studied for their acoustic properties. These foams may contain information about a particular

mechanism that could lead to new technology. Additionally, research conducted on rigid open-cell foams containing nonrigid elements lumped in a similar way manner to that discussed in Chapter 2 is sparse or nonexistent. The bulk absorption characteristics of carbon foam at high frequencies are very favorable, however, at frequencies below ~1500 Hz, it typically performs poorly without the addition of extraneous volume. The research on membrane-embedded acoustic liners discussed in Chapter 2 shed some hope on gaining better low-frequency performance. By uniting these two liner concepts, a unique membrane-embedded carbon foam design is considered. The acoustic performance of this foam is characterized, modeled, and embedded with a tensioned membrane located a certain distance down the cavity to produce a liner that contains the favorable low-frequency performance of the nonrigid element as well as the favorable bulk properties of the foam taking care of the mid to high-frequency range.

1.4. Potential Applications

It is clear that there are various potential industries that benefit from advances in noise mitigation technology. In this study, the primary focus industry is aviation. However, membrane-type noise suppressor technology and other bulk material (such as fiberglass and other limp or rigid foams) technology can have potential applications in the automotive, industrial, building acoustics as well as many other industries. Supersonic commercial aircraft like the Concord may see the light of day in our life as long as the noise restrictions put in place by the FAA are met. But as measured back in 1977, the 119.4 dB (a clap of thunder is roughly 120 dB) produced by the Olympus 593 engine at takeoff will not meet the current noise standards. This is just one of many reasons that this technology is vital to the future of aviation. More recently, NASA has been interested in new liner concepts which target reducing engine core noise using rigid metal open-cell foams placed over the rotor [60, 61]. To the extent that membrane-embedded and folded cavity liners can be implemented in practice, opportunities exist to mitigate hitherto unaddressed

yet significant low-frequency contributors to acoustic noise in several applications such as in aerospace, HVAC, and civil infrastructural domains. It is obvious that the environment located so close to the rotor and stator will require a material that can withstand the harsh pressures and temperatures as well as provide impact damage mitigation. Following suit with NASA, the open-cell, carbon foam investigated within Chapter 4 of this thesis could be a contender for that application. Additionally, the internal combustion engines on unmanned aerial vehicles which requires high torque with low RPM could benefit from this technology. With the current engineering needs in mind, there is potential that carbon foam could be considered as an acoustic insulator for numerous aerospace applications as well as industrial applications where multifunctionality is desirable due to their excellent thermal and mechanical properties.

1.5. Chapter Overviews

Chapter 1 discusses the motivation and a brief history of noise reduction technology along with a summary of some of the relevant work conducted by other researchers in the field of noise attenuation. Additionally, lightweight, low-frequency liner concept designs are discussed as a prelude to what will be investigated within this thesis. A brief overview of the membrane-embedded, folded-cavity, and carbon foam liner concepts is given as an introduction to what is to come in the following chapters.

Chapter 2 introduces a compact liner concept with a structurally resonant element – the membrane-embedded liner, and goes into detail about each of its design concepts and fabrication techniques used to build these liners. The test cases used to explore the mechanisms involved are presented. Next, the finite element modeling done using COMSOL Multiphysics is discussed for various membrane-embedded liner concepts. Then, the experimental methods used to capture the acoustic response are discussed followed by a discussion of the results and a chapter summary.

Chapter 3 presents another low-frequency liner concept, the folded-cavity liner, which envisions packing long acoustic paths within a compact volume. This chapter begins with an overview of the liner concept followed by a discussion of the concepts and designs. The analytical modeling of the folded cavity using the Zwikker and Kosten lumped element model is discussed followed by a discussion of the experimental methods. This is followed up by a discussion of the results and comparison of the simulations with the experiments and a chapter summary.

Chapter 4 introduces a potentially multifunctional liner concept, the carbon foam liner, and begins with an overview and a discussion of the design concepts. Next, the COMSOL Multiphysics poroacoustics model used to represent the foam is discussed as well as an analytical formulation used to capture the acoustic properties of the foam. This is followed by the experimental methods and a discussion of the experimental and simulation results, and a chapter summary.

Chapter 5 gives an overview of the significant conclusions from each of the design concepts and offers a few recommendations for future work to be conducted in further exploring new low-frequency acoustic liner concepts.

CHAPTER II

Membrane-Embedded Liner

2.1. Overview

The Membrane-Embedded Liner (MEL) concept is the first design investigated in this thesis and contains an extensive number of tests and test results. Overall, the design form-factor is packaged together using a somewhat similar design configuration as described in Figure 7. Although this is not a new idea, there is little supporting data covering non-rigid elements embedded within an acoustic liner. The basis for MEL design is to utilize the low-frequency resonance of a tensioned membrane which is embedded within a liner cavity to provide not only the standard cavity resonance but an infinite amount of resonances produced by the membrane. By controlling the tension applied to the membrane and also controlling other parameters that affect the membrane resonance such as the length and width dimensions of the membrane, membrane thickness, and (as discovered later on in this thesis) the location of the membrane within the cavity, a tunable design is attainable. Many of the MEL design concepts investigated within this chapter have been presented in 2018 and 2019 [62, 63].

2.2. Concepts and Designs

The first set of acoustic liner configurations investigated is the membrane-embedded liner. The MEL consists of top and bottom cavity sections and two septum plates which encapsulate a pre-tensioned membrane. Because a tensioned membrane consists of n-number of resonance's, this is considered a multiple-degree of freedom liner (MDOF). Figure 14 describes this configuration in better detail.
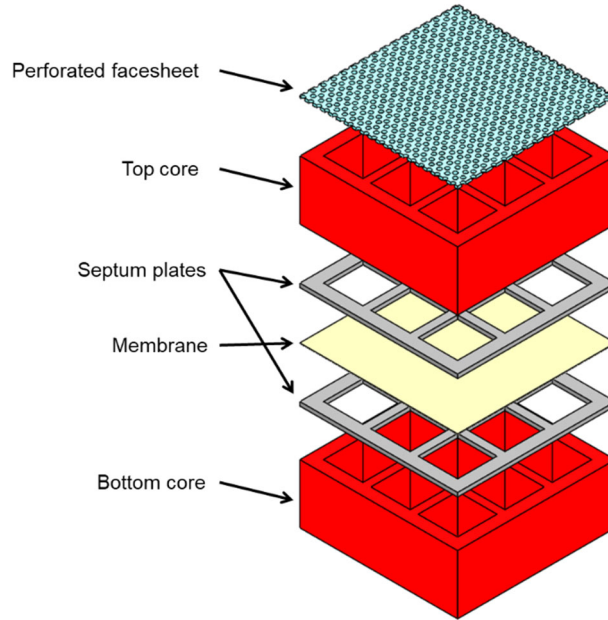
Figure 14: Experimental test article configuration for the MEL

In order to tune the natural resonance frequency of the membrane, a custom rig was used to apply a state of uniform tension to the membrane using traction weights before incorporating it into the test article. Under the assumption of uniform tension and homogeneous membrane material, the modal frequencies for a square membrane with fixed edges are given by

$$f_{mn} = \frac{c_m}{2}\sqrt{\left(\frac{m}{a}\right)^2 + \left(\frac{n}{b}\right)^2} \qquad\qquad Eq.\ 2.1$$

where m and n are the mode numbers in the principal directions, a and b are the side lengths of the cell being considered and c_m is the speed of sound through the membrane given by

$$c_m = \sqrt{\frac{m_t g}{\rho_m t_m}} \qquad\qquad Eq.\ 2.2$$

where m_t is the membrane tensioning mass, g is the acceleration due to gravity, ρ_m is the areal density of the membrane and t_m is the thickness of the membrane. Parametric studies were conducted to understand the effects on modal frequencies. Figure 15 below shows the variation of the first 5 nonrepeating modes comparing the cavity side length and the applied tension per unit length.
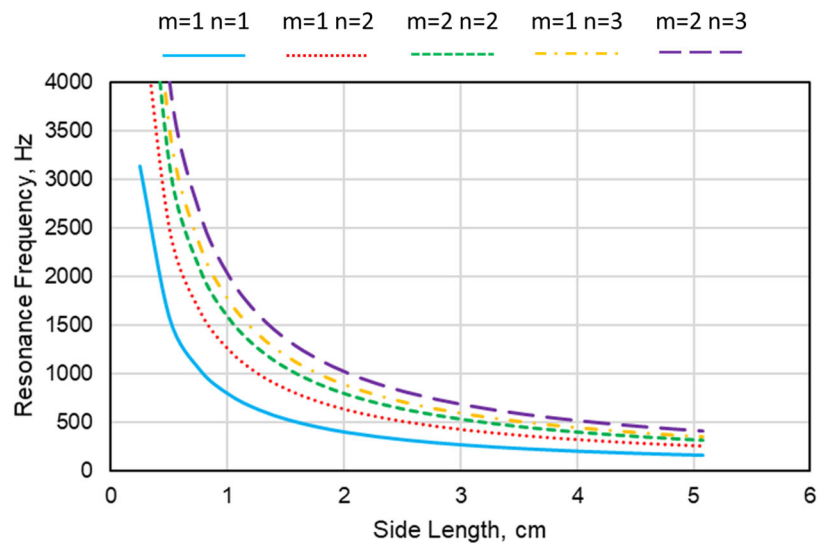
Figure 15: Example of a parametric study conducted on the membrane side length vs resonant frequency

In this case, the membrane tension is set to 1930 N/cm, the density is ~1 g/cm³, and a thickness of 0.015 cm. Increasing the cavity side length decreases modal frequencies whereas increasing the tension increases the modal frequencies. The influence of the lowest mode dominates in the structural-acoustic response. Fixing the cavity size, the tension was used as a tunable parameter to control the resonance of the membrane-embedded within the septum. The design of the baseline and membrane-embedded test articles are similar to conventional liners, with the addition of minor simplifications to facilitate modular fabrication for testing. The components of the test article are shown in Figure 14. The cores of various thicknesses are additively manufactured.

The MEL liner has outer dimensions of 5.08 cm x 5.08 cm, a thickness of 4.11 cm, the inner walls are 1.27 cm x 1.27 cm, and the inner wall thickness is 0.254 cm. The initial set of test articles utilize a constant liner total thickness, cell size, and wall thickness with the membrane placed at three different locations within the liner. Additionally, a 4% open area facesheet is used with low, medium, and high nominal tensions. Additional tests are conducted without the use of a facesheet with a high-tension membrane. All of these tests were run using an overall sound pressure level of 140 dB measured from the reference microphone. Table 1 describes the experimental test configurations in further detail.

Table 1: Initial MEL configurations

Case Number	Membrane Height from Top, cm	4% Open Area Facesheet Included	Membrane Tension, N/cm
LC1	0.635	Yes	0
MC1	0.635	Yes	1931
HC1	0.635	Yes	3862
LC2	1.270	Yes	0
MC2	1.270	Yes	1931
HC2	1.270	Yes	3862
LC3	1.905	Yes	0
MC3	1.905	Yes	1931
HC3	1.905	Yes	3862
HC4	0.635	No	3862
HC5	1.270	No	3862
HC6	1.905	No	3862

The results from this study led to questions about the particular physics involved with respect to the membrane location within the liner. So, in order to investigate the effect that the membrane has on the acoustic response with respect to location, a membrane height study was conducted. The membrane's location varied starting from the back-plate (bottom) towards the incident side (top) in increments of 1.27 cm while maintaining a total liner thickness of 7.62 cm. For this study, all cases have a high state of tension of 3862 N/cm and a sound pressure level of 140 dB. To eliminate higher-order effects, no facesheet was used. Table 2 outlines the experimental test cases for the MEL height study.

Table 2: MEL test cases considered for the membrane height study

Case Number	Membrane Height from Bottom, cm
H1	0.635
H2	1.270
H3	1.905
H4	2.540
H5	3.175
H6	3.810
H7	4.445
H8	5.080
H9	5.715
H10	6.350
H11	6.985

After analyzing the results from the previous two studies, a hypothesis was formed that the volume of air entrapped between the membrane and the back-plate may be a leading factor in the acoustic propagation. By conducting a set of experiments where the length of the bottom cavity is held constant and the length of the top cavity is increased, the interaction of this volume of entrapped air can be realized. So, to round out this set of experiments on the MEL, a final case study was conducted to ascertain the relative influence of the air column in the top cavity versus the bottom cavity on the absorption performance of the MEL. To do this, the thickness of the bottom cavity below the membrane is held constant while increasing the cavity thickness above the membrane. These tests were conducted using the high-tension membrane, without the interference of a facesheet, and at an overall sound pressure level of 140 dB (measured from the reference microphone). Table 3 outlines the test cases for this investigation.

Table 3: MEL test cases with height variation of top cavity core length

Case Number	Top Cavity Depth, cm	Bottom Cavity Depth, cm
T1	0.635	1.905
T2	1.270	1.905
T3	2.540	1.905
T4	3.810	1.905
T5	5.080	1.905

Following this series of tests is a MEL configuration which includes a mass addition of small adhesive dots. These configurations implement the same configuration as test cases HC4-HC6. The mass addition consisted of neoprene rubber adhesive dots which are 0.3 cm in diameter and

have a thickness of 0.15875 cm. Relative to the estimated weight of the membrane within each

cavity there is a roughly 40% increase in mass due to the adhesive dots. The experimental

configurations are shown in Table 4.

Table 4: MEL test cases with neoprene mass addition

Case Number	Membrane Height, cm	Membrane Tension, N/cm
HCM1	0.635	3862
HCM2	1.27	3862
HCM3	1.905	3862

The next MEL study stems from the initial parametric studies where the cavity lengths are altered

in order to tune the liner for a particular range of frequencies. This liner design has a similar build

configuration to that of the previous test case. The varying cavity sizes for the 5.08 cm x 5.08 cm

membrane-embedded test article (see Figure 16) are designed and the following figure shows

the final design along with the first theoretical natural frequency for each differing cavity.
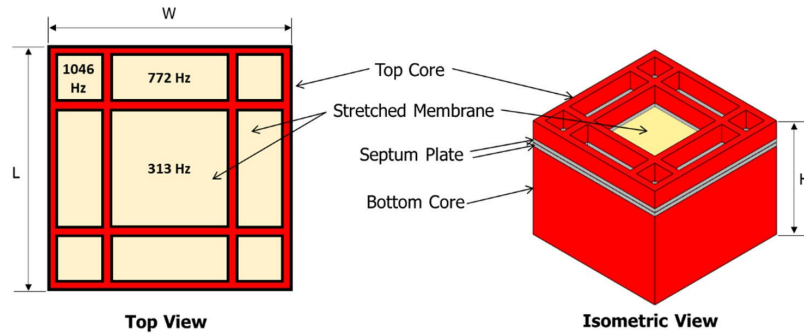
Figure 16: Top view (left) and isometric view (right) of the non-uniform MEL

The material properties for this liner design are summarized Table 5.

<div align="center">Table 5: Summary of properties for the non-uniform MEL</div>

Property	Symbol	Value
Length	L	5.08 cm (2 in)
Width	W	5.08 cm (2 in)
Total Height	H	4.11 cm (1.62 in)
Membrane Density	ρ	0.940 g/cm^3
Membrane Thickness	t	0.017 cm (6.69×10^{-3} in)
Tensioning Mass	m	1000 g
Side of Large Square Cell	S_{LS}	2.54 cm (1 in)
Side of Small Square Cell	S_{SS}	0.760 cm (0.3 in)
Length of Rectangular Cell	L_R	2.54 cm (1 in)
Width of Rectangular Cell	W_R	0.760 cm (0.3 in)

Table 6 outlines the test cases investigated for the non-uniform MEL. It is noted that the initial set

of tests were conducted with no facesheet and then with various meshes in order to get the

optimum resistance to result in the optimum acoustic performance. A 27 CGS Rayl mesh was

found to result in a resistance very close to 1 and thus all test cases presented for this set of tests

contain that mesh as a facesheet.

<div align="center">Table 6: Non-uniform MEL test cases with a 27 CGS Rayl mesh as facesheet</div>

Case Number	Mem Height from Bottom, cm	SPL, dB	Active Cavities
NUL1	0.635	120	All
NUL2	0.635	140	All
NUL3	3.175	120	All
NUL4	3.175	140	All
NUL5	3.175	120	Large Square
NUL6	3.175	140	Large Square
NUL7	3.175	120	Small Squares
NUL8	3.175	140	Small Squares
NUL9	3.175	120	Rectangles
NUL10	3.175	140	Rectangles

The next test sample is a slanted cavity design where essentially the baseline MEL with a total

height of 4.11 cm is sliced along the diagonal. The purpose of this design is an attempt to take

advantage of both, membrane closest to the surface of the liner to result in better low-frequency

performance and also the membrane closest to the bottom of the liner to give broadband

performance. This design only was tested in two different forms, with and without a 4% open

area facesheet, and so a table of test cases is not provided. It should be noted that the membrane is no longer a square, but due to the slanted nature of the septum plates, the rectangular area is greater and thus should have a lower fundamental resonance. Figure 17 is provided below to illustrate the design.
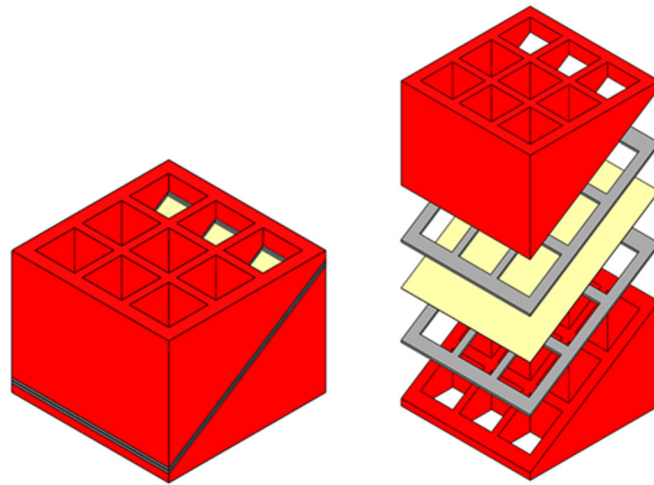
Figure 17: Slanted core design CAD model

The next set of MEL test cases incorporates the addition of an added mass to the center of the membrane. Due to the testing capabilities of the NIT, smaller cavities were used in case the mass addition onto the membrane drops the resonant frequency below the testing capabilities. Thus, a 5x5 array of square cells with a side length of 0.762 cm was created and 3D printed. As seen from the previous test case, the resonance frequency for a square membrane with a side length of 0.762 cm is just over 1000 Hz. A schematic illustrating the experimental test configurations is shown in Figure 18 below.
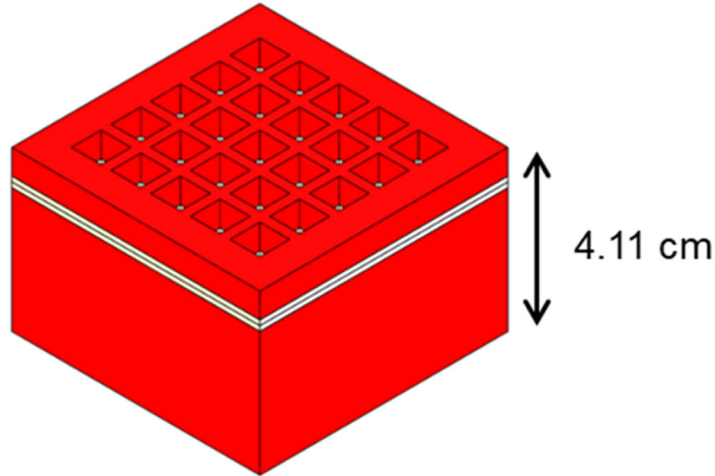
Figure 18: 5x5 experimental configuration for membrane with added mass cases

When considering potential added masses, it is desirable to use an add-on that has a small volume, is symmetrical, and lightweight compared to the mass of the membrane. After many considerations, the final decision ended up being quartz crystals used for electronic PCB boards. This was the best choice for the time because of accessibility and funding. Three different weights are considered, 0.027 g, 0.035 g, and 0.102 g. Along with the three different weights of added mass, three different membrane heights are considered as well, no facesheet is used in these tests but the 27 CGS Rayl mesh is used to obtain the optimum performance. The test configurations are presented in Table 7 below.

Table 7: 5x5 MEL test cases

Case Number	Membrane Height from Bottom, cm	SPL, dB	Added Mass, g
BL1	0.635	140	None
BL2	1.270	140	None
BL3	1.905	140	None
AM1	0.635	140	0.027
AM2	1.270	140	0.027
AM3	1.905	140	0.027
AM4	0.635	140	0.035
AM5	1.270	140	0.035
AM6	1.905	140	0.035
AM7	0.635	140	0.102
AM8	1.270	140	0.102
AM9	1.905	140	0.102

2.2.1. Fabrication

The MEL designs were first designed using SolidWorks and then 3D printed using a Prusa i3 extrusion type 3D printer. The MEL design utilizes the sample holder's 1.27 cm thick backing as the back-plate. The membrane is tensioned using a customized, hand-built tensioning rig. Overall, the tensioning rig is a large 35.56 cm x 35.56 cm square where the membrane is fixed on two perpendicular sides and then placed over rollers on the other sides. To add tension, there are weights that are placed on the two edges that drape over the two rollers. Once the weights are affixed to the membrane, the weights are then hung off of the corner of a table. To clarify this further, a diagram is shown below in Figure 19.
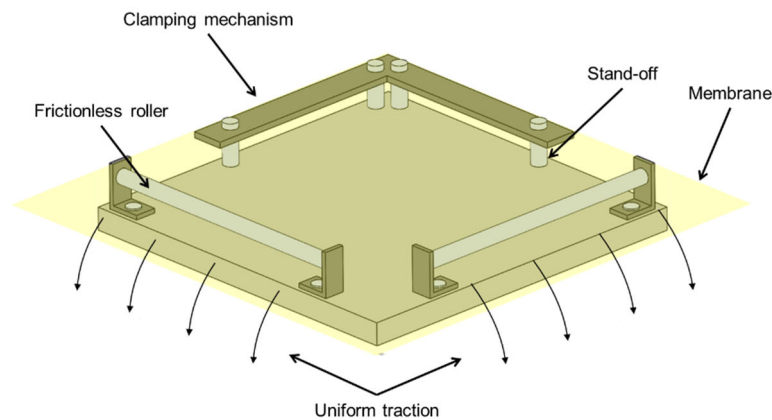
Figure 19: Membrane tensioning rig configuration

Once the tension is set, the two septum plates are 'painted' with a light coat of adhesive on one side ensuring that there is no adhesive spillover when sandwiching the membrane. Once the septum plates are in place a flat piece of aluminum is placed on the outermost septum plate along with a 2270 g weight to ensure that there is a good bond between the membrane and the septum plates. The septum plates and membrane are then left for 24 hours as per the adhesive manufacturer's recommendation for cure time. After the adhesive has had time to properly cure, the septum plates are cut out with scissors, and then any overhanging membrane is trimmed off using a razor blade.

Once the septum and tensioned membrane have been fabricated and have had ample time to cure, the additional liner pieces are 3D printed to produce the top cavity (incident to the sound source) and the bottom cavity (closest to the rigid back-plate) as well as any other extra pieces needed in order to run all of the testing configurations. Figure 20 shows photos of the completed experimental test articles including the tensioned membrane.
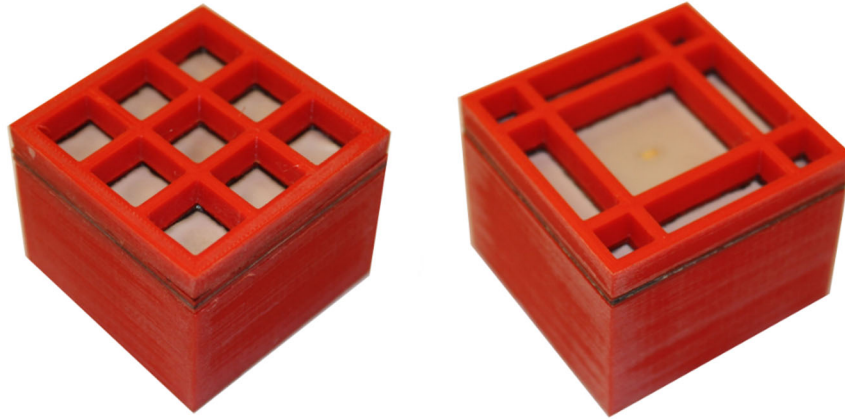
Figure 20: Experimental test configurations for the baseline MEL (left) and the Non-Uniform MEL or NUL (right)

2.3. Modeling

To design a MEL, an investigation on the natural frequency of a membrane was conducted. A series of finite element simulations were developed using COMSOL Multiphysics to simulate an impedance tube environment following the ASTM 1050-12 [64]. The program is set up using the Pressure Acoustics, Frequency Domain, model using a stationary study. The study includes non-linear stress and strain due to the pre-stressed tension in the membrane. Integrations points are used in the model to compute the sound pressure at the three reference microphone locations that are required by the standard. Symmetry is also utilized for computational efficiency. The walls of the model and the impedance tube are modeled to have an infinite impedance. Because of this lack of resistance in the simulation, there will also be a small margin of error associated with it.

Figure 21 illustrates the simulation configuration as it is modeled in COMSOL. The plane wave is applied at the source followed by the square acoustic domain used as a waveguide. Next are the measurement microphone locations, followed by the acoustic liner modeled with the embedded membrane.
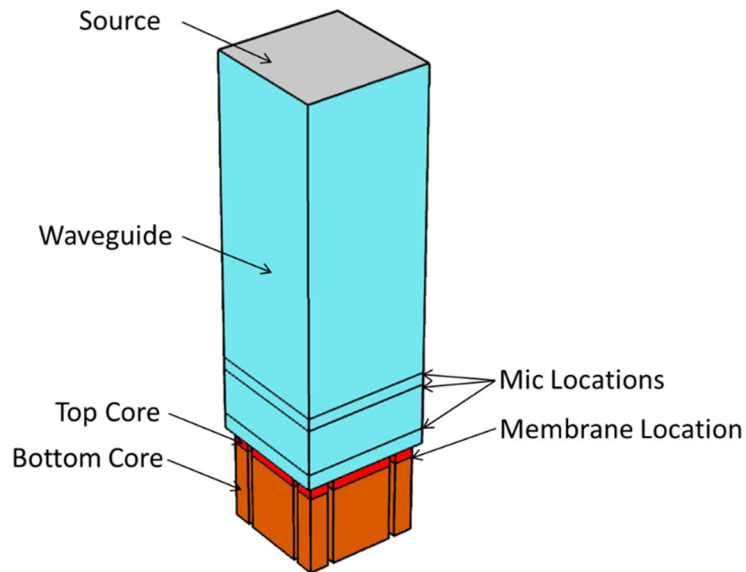
Figure 21: COMSOL simulation model

A mesh convergence study was conducted to ensure that the acoustic mesh was completely resolved. Using a grid resolution of 8 elements per highest wavelength (i.e. 3000 Hz) for the entire frequency sweep. Although only 5 elements is required for second order shape functions, in various places within literature 8 elements per wavelength is often used. The following plot demonstrates the mesh convergence study comparing the use of 5 elements per highest wavelength and 8 elements per highest wavelength.
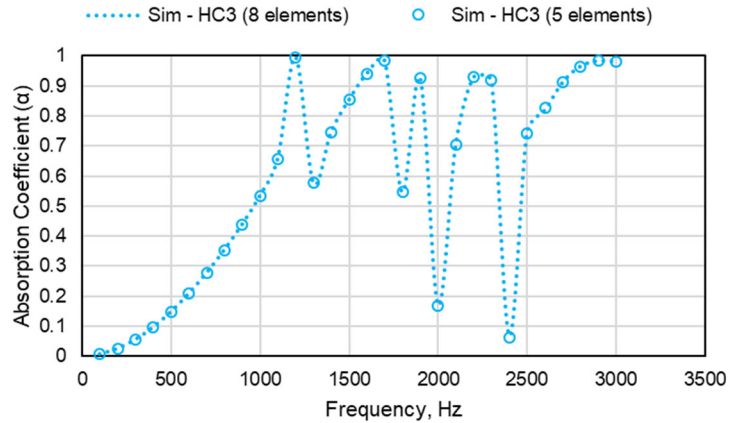
Figure 22: Absorption coefficient plot for the COMSOL simulation mesh convergence study comparing 8 elements per highest wavelength (dotted line) and 5 elements per highest wavelength (circles)

The bandwidth between frequencies for this study is 100 Hz to reduce the computation time for the simulation. It is clear that there is not a difference in the absorption coefficient when using 5 or 8 elements per highest wavelength. Thus, the grid resolution used for the all of the COMSOL simulations is sufficiently fine to capture the acoustic response of the design concepts presented within this thesis.

2.4. Experimental Methods

The experiments presented in this thesis are conducted at two different locations, Oklahoma State University and NASA Langley Research Center. The experiments at Oklahoma State University were done using an impedance/transmission loss tube. At NASA Langley Research Center, the experiments were conducted using the Normal Incidence Tube (NIT). Both impedance tubes were verified previously against one another [48]. It should be noted that all impedance data presented in this thesis is normalized with respect to air, and within this chapter are conducted using the NASA Langley NIT as described in the following section.

2.4.1. NASA Langley Normal Incidence Tube

The NIT uses ASTM Standard E1050-12 for measuring the absorption coefficient and impedance of acoustic materials using a two-microphone method and a digital frequency analysis system. The results from this tube are valid for frequencies from 500 Hz – 3200 Hz. The 5 JBL pressure drivers result in the maximum overall sound pressure level of about 140 dB. It should be noted that most NIT tests were conducted at sound pressure levels of 120 dB and 140 dB, but for brevity, only the 140 dB test results are shown in the body of this thesis as nonlinearity is not the main focus of this investigation. Figure 23 illustrates a schematic of the NASA Langley NIT.
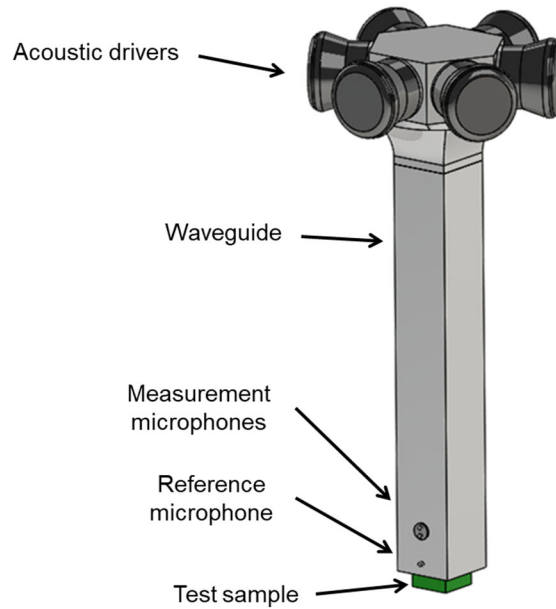
Figure 23: Schematic of the NASA Langley NIT

2.5. Discussion of results

2.5.1. Uniform Membrane-Embedded Liner

2.5.1.1. Baseline Membrane-Embedded Liner

The results of the baseline MEL tests outlined in Table 1 are presented in Figure 24 below

followed by the corresponding results for other tests of interest for the uniform MEL.
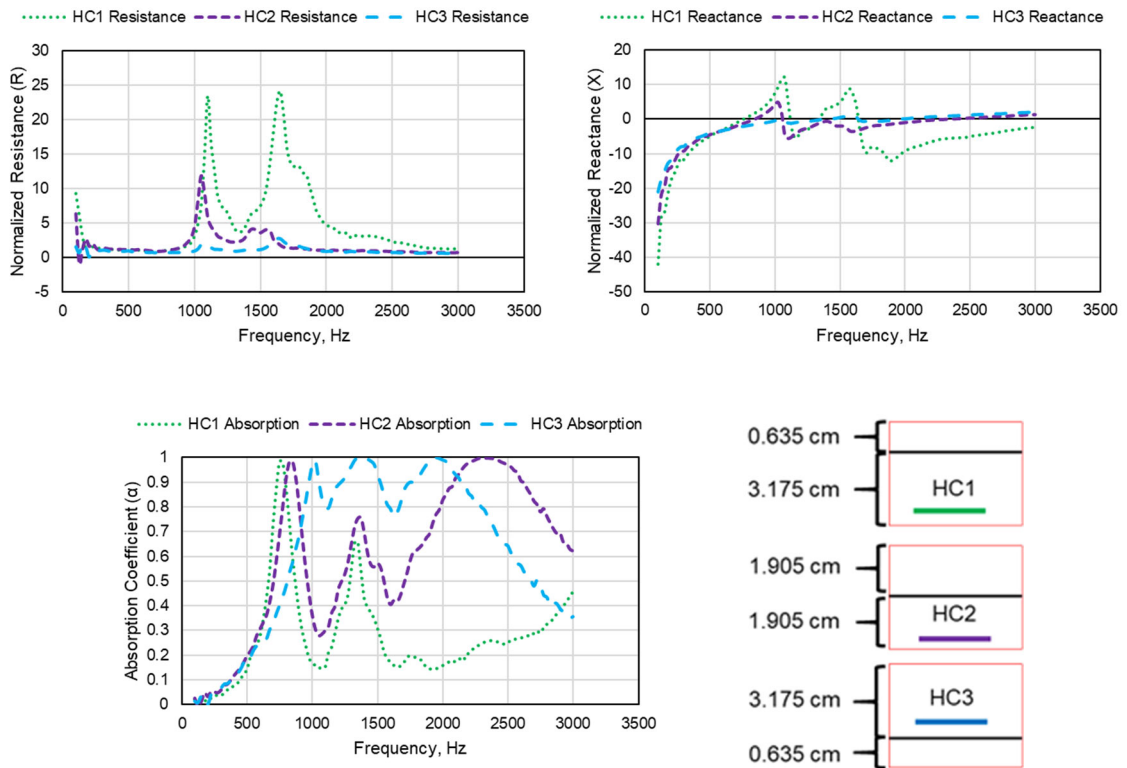
Figure 24: Resistance (top left), reactance (top right), absorption coefficient (bottom left), and configuration schematic (bottom right) plots for high tension tests conducted at 140 dB with a facesheet included

When the membrane is located towards the top of the cavity (HC1) yields a concept that has a

resonant peak at around 800 Hz with a secondary, weaker, peak around 1300 Hz. HC2 behaves

similarly with the third broad resonance peak showing up around 2200 Hz. Shifting to the third

configuration where the membrane is located towards the bottom of the cavity (HC3), there are 3 clear peaks that occur resulting in broadband absorption from about 850 Hz to 2500 Hz. Along with these observations, the resistance and reactance curves are rough in HC1 but moving the septum down the cavity yields smoother curves. These smoother curves clearly result in better broadband performance likely due to the optimum impedance (resistance and reactance), relative to that of air, being achieved.

2.5.1.2. High-Tension Membrane-Embedded Liner

The following (Figure 25) are the test results for the high-tension test case with no facesheet included.
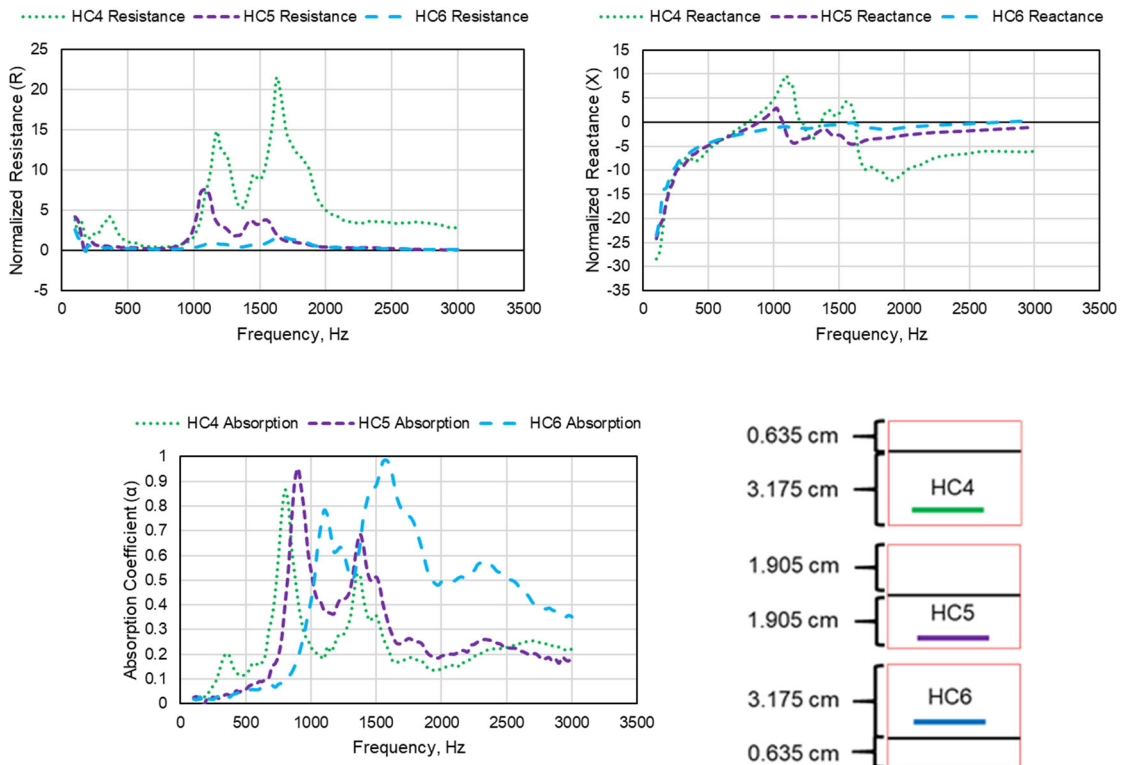
Figure 25: Resistance (top left), reactance (top right), absorption coefficient (bottom left), and configuration schematic (bottom right) plots for the high tension tests conducted at 140 dB with no facesheet included

Similar to the previous test case, HC4 and HC5 behave in a similar fashion, with HC6 resulting in acoustic performance to HC5 but with the peaks shifted slightly. It appears that the lack of resistance due to a facesheet took a slight hit on the performance.

2.5.1.3. Membrane-Embedded Liner Height Study

The next set of results (presented in Figure 26) are for the height study that is outlined in Table 2, however for this case only the odd-numbered test cases are shown to help alleviate the confusion of having 11 data sets presented on one graph. The rest of the data left out for brevity can be found in the appendix in Figure A1.3.
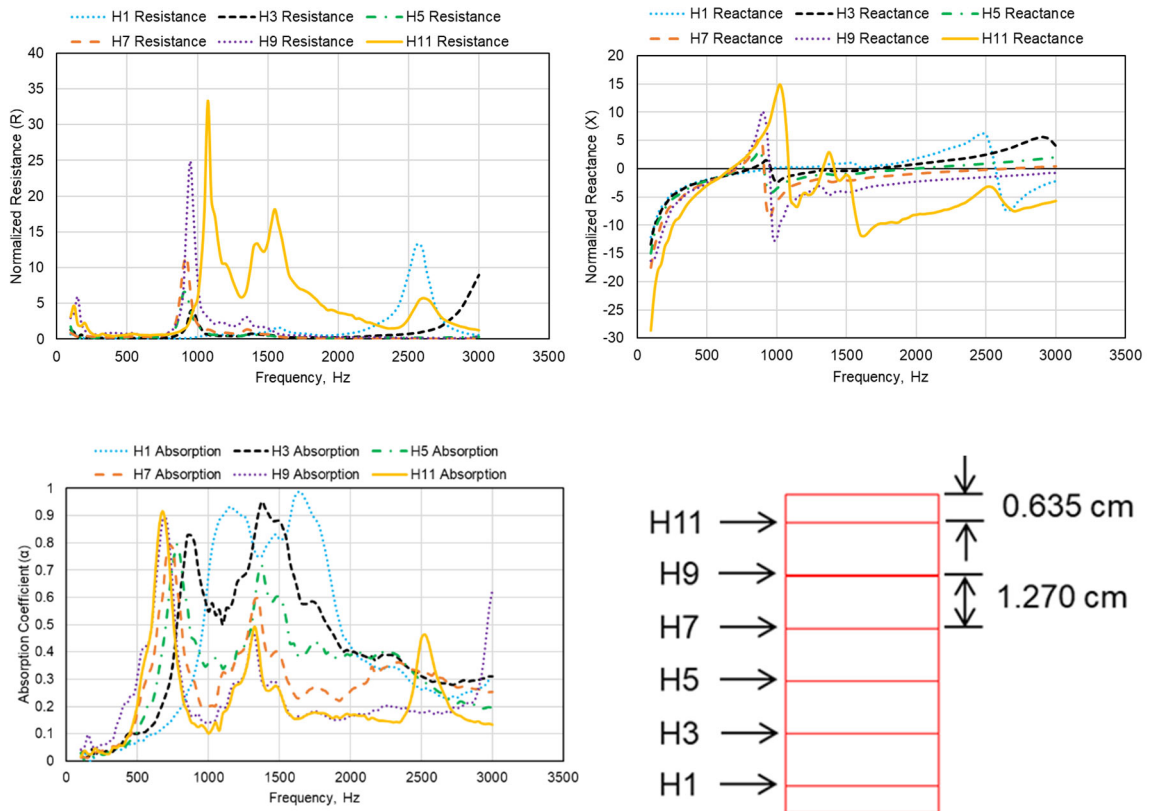
Figure 26: Height study resistance (top left), height study reactance (top right), height study absorption coefficient (bottom left), and configuration schematic (bottom right) plots for the high tension tests conducted at 140 dB with no facesheet included

The previously stated hypothesis regarding the impedance spectra smoothing out when the membrane is located near the bottom of the cavity holds true for this height study. There is a clear correlation between the membrane height and the first absorption peak; the closer the membrane is to the top of the cavity the lower the absorption peak, or the closer it is to the calculated theoretical value of the first membrane resonance. The bottom cavity acts as a stiffening mechanism on the membrane, yielding a higher resonance than what is calculated. The second resonant peak in the absorption follows that of the second zero crossing of the reactance. This resonant peak initially appeared to correspond with potentially the second resonant peak but can conclusively be identified as the quarter-wave cavity resonance. So the membrane is essentially acting as a hard wall not allowing the acoustic wave to resonate with the actual full cavity length. To dig a little deeper into the mechanism at play here a few targeted cases were run through a propagation code that incorporates the convected Helmholtz equations to examine the standing wave with respect to the membrane and resonant frequency at the surface of the liner [65]. As this is not the main goal of this investigation more details can be found in the appendix.

2.5.1.4. Top Cavity Height Study

Holding this stiffening parameter constant allows the influence of the top cavity length or volume to be isolated as the only changing variable. In the previous investigations, the initial thought was that the only changing variable was the membrane height. The next set of charts display the results from the test cases outlined in Table 3.
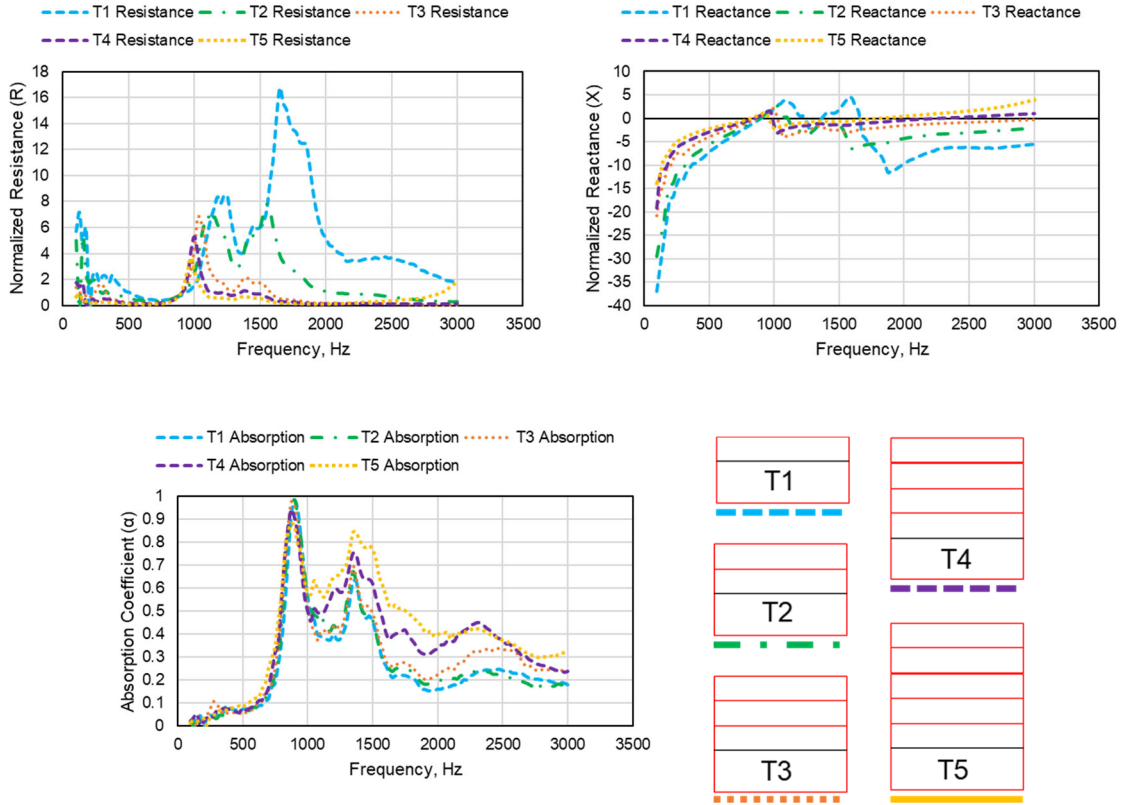
Figure 27: Constant bottom cavity study resistance (top left), constant bottom cavity study reactance (top right), and constant bottom study absorption coefficient (bottom left) plots for the high tension tests conducted at 140 dB with no facesheet included

By holding the distance that the membrane is from the bottom of the cavity constant and increasing the length of the top cavity yields very similar absorption spectra for each test case. The longer the top cavity is, it appears to flatten out the normalized impedance curves (R and X) which enables slightly better performance after the initial membrane resonance. In each test case within this study, the plot of the absorption coefficient shows that the first peak located at 875 Hz is sustained throughout. The location of the second peak at 1400 Hz is also constant although the magnitude of that peak displays some dependence on the length of the cavity above the membrane.

45

2.5.1.5. Uniform MEL with Neoprene Mass Addition

Figure 28 shows the results for the uniform MEL with the neoprene mass affixed to the center of the membrane located in each cavity.
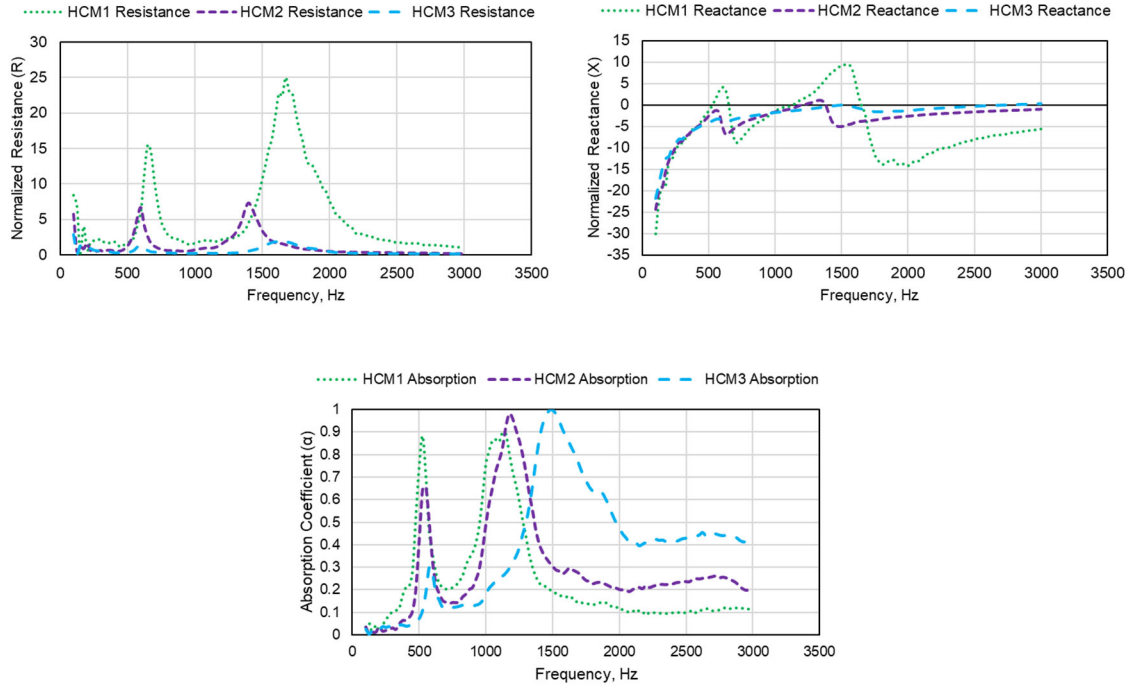
Figure 28: Uniform neoprene mass addition MEL resistance (top left), reactance (top right), and absorption coefficient (bottom)It is clear that the addition of the neoprene dots results in an influence in the acoustic spectra, for HCM1 the first absorption peak

It is clear that the addition of the neoprene dots results in an influence in the acoustic spectra, for HCM1 the first absorption peak has shifted from around 800 Hz (from the HC4 test case) to the lower frequencies by about 350 Hz. Additionally, that peak is much narrower and located around 500 Hz, and the second resonance peak located at 1100 Hz is more pronounced and shifted to the lower frequencies by about 200 Hz with respect to the corresponding HC4 test case. HCM2 follows a similar trend as HCM1 along with the transition between HC4 and HC5. As for the last test case HCM3, the magnitude of the first peak (which is not the dominant peak in HC6) is reduced and shifted to the lower frequencies by about 500 Hz. The second more dominant peak

shifts to the lower frequencies by only about 100 Hz. Overall, this mass addition results in a lower resonance without a huge penalty in the overall acoustic performance.

2.5.1.6. Uniform MEL Simulation Comparisons

Figure 29 shows the simulation comparison for HC1-HC3 experimental test cases.
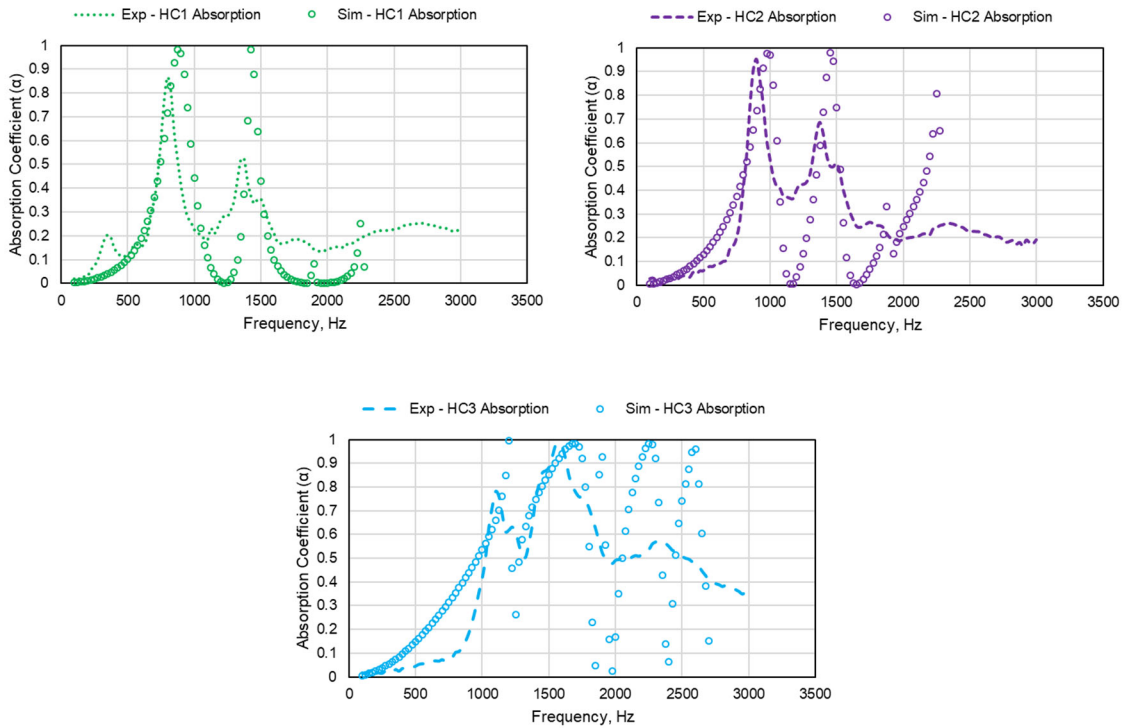
Figure 29: Comparison between experiments and simulations for HC1 (top left), HC2 (top right), and HC3 (bottom)

Although the graphs do not match up perfectly due to a lack of losses taken into account by the structural elements in the fluid domain, the trend that occurs in the experiments is still captured by the simulation. Additionally, for the most part, the primary resonant peaks observed in the experiment are accounted for in the simulation and are located relatively close together.

2.5.2. Non-Uniform Membrane-Embedded Liner

2.5.2.1. Baseline Non-Uniform Membrane-Embedded Liner

The next set of charts display the test results for the non-uniform MEL, the full set of test cases are outlined in Table 6.
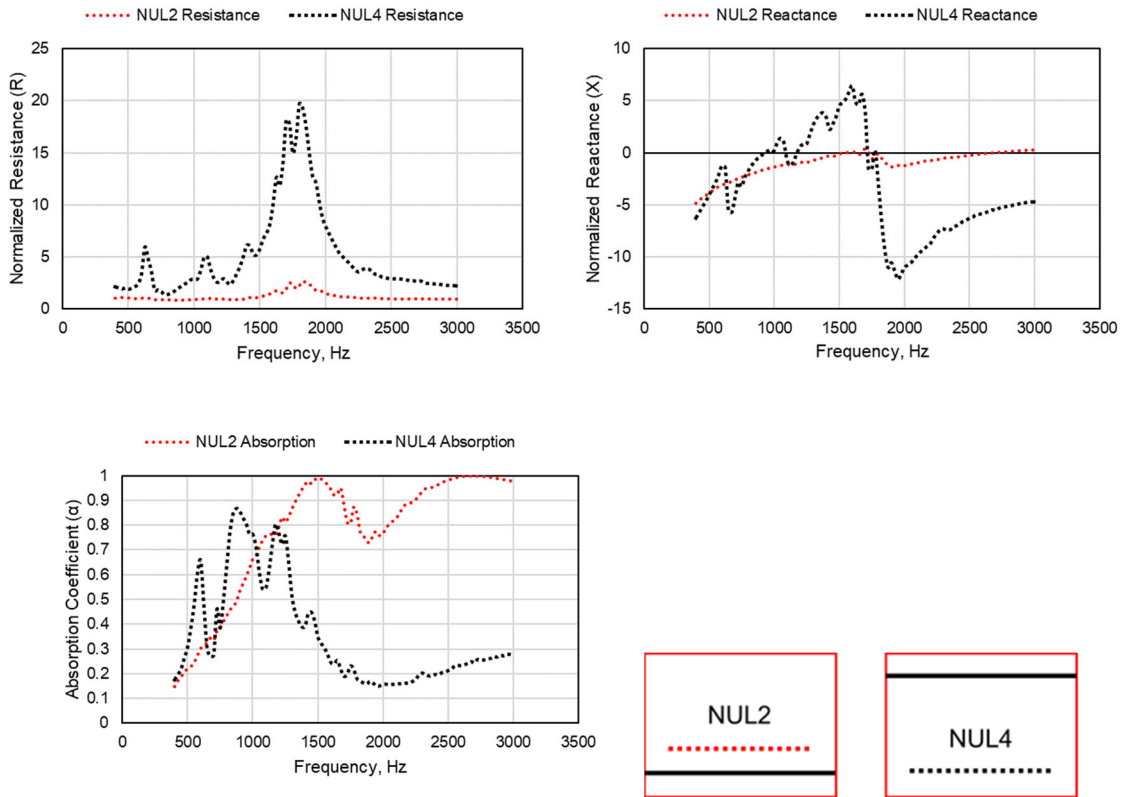
Figure 30: Non-uniform MEL resistance (top left) and reactance (top right), non-uniform MEL absorption coefficient (bottom left), and configuration diagram (bottom right)

The non-uniform MEL yields the targeted acoustic response in both cases, by changing the geometry of the membrane (and as a result the cavity), tuning the liner to a particular frequency range can be achieved. In this case, the trend observed in HC1-HC3, HC4-HC6, and H1-H11 is observed here. When the membrane is located near the surface of the liner, low-frequency absorption peaks are clearly seen around 600 Hz with some mid-frequency performance between 800 Hz – 1300 Hz. Moving the membrane near the bottom of the cavity results in an acoustic

response that is shifted to slightly higher frequencies with much better broadband performance

from ~900 Hz extending throughout the rest of the test frequency range. However, the many

resonant peaks that occur in NUL2 result in a lower-frequency broadband performance than in the

similar configuration HC4 test case. The question now is which resonant peaks correspond to

which cavities?

2.5.2.2. Non-Uniform Membrane-Embedded Liner Cavity Influence

The next set of test results (in Figure 31) presented are that of the investigation that was

conducted on the cavity influence for the non-uniform liner. The schematic in the following

figure is a provided as a visual aid to denote which cavities were active. For example, the yellow

rectangles indicate that for the NUL10 test case, all other cavies are blocked off using 3D printed

inserts as well as aluminum tape in an attempt to minimize the losses due to the plastic inserts.
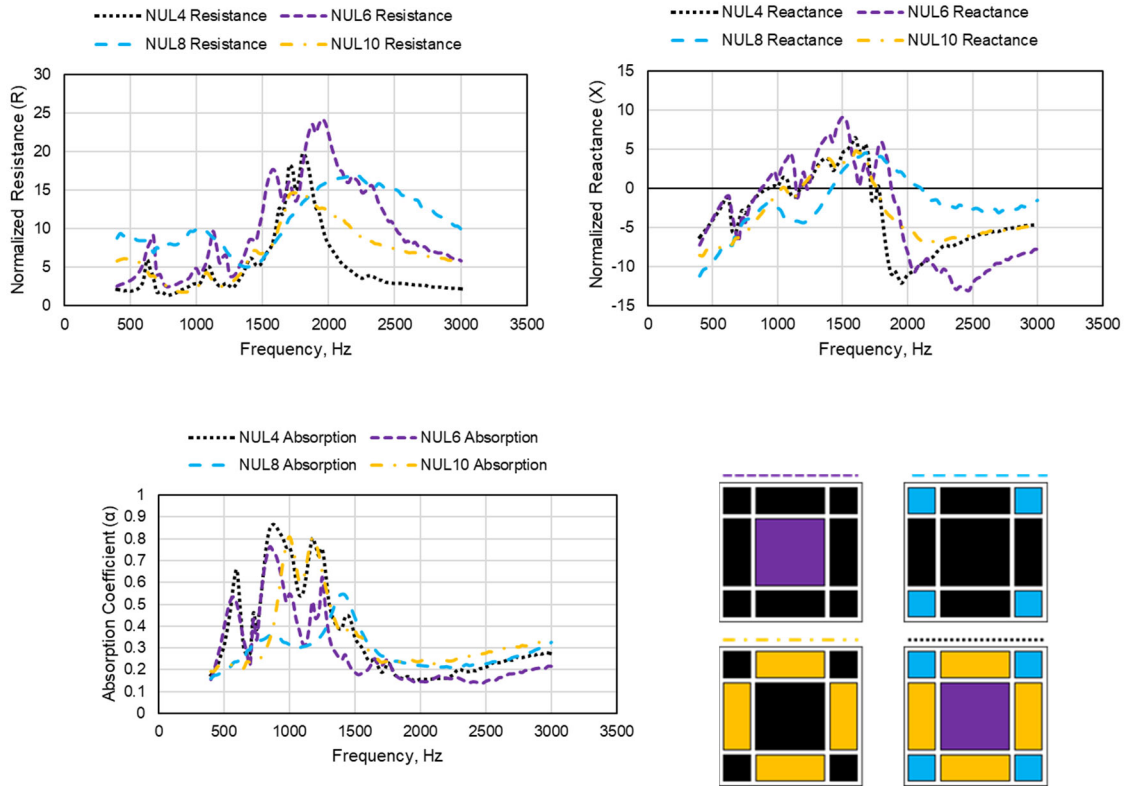
Figure 31: Cavity influence resistance (top left), cavity influence reactance (top right), cavity influence absorption coefficient (bottom left), and schematic (bottom right)

It is very clear that the large center square cavity is responsible for both of the first two peaks (located at 550 Hz and 875 Hz) as shown by NUL6. NUL8 seems to result in minimal to no performance benefit in this configuration. Looking at NUL10, the rectangular cavities do add some benefits to the overall performance. The second resonant peak at 875 Hz shown in NUL6 appears to have merged with the first peak shown in NUL10 located at 1000 Hz to result in a slightly more broadband peak. The second absorption peak at 1200 Hz seen in NUL10 looks like it is joined by the third peak seen in NUL6 (albeit with no added performance by NUL6).

2.5.2.3. Uniform vs. Non-Uniform Membrane-Embedded Liner

For completeness, a comparison of the absorption coefficient and normalized impedance between the uniform MEL and non-uniform MEL is presented in Figure 32.
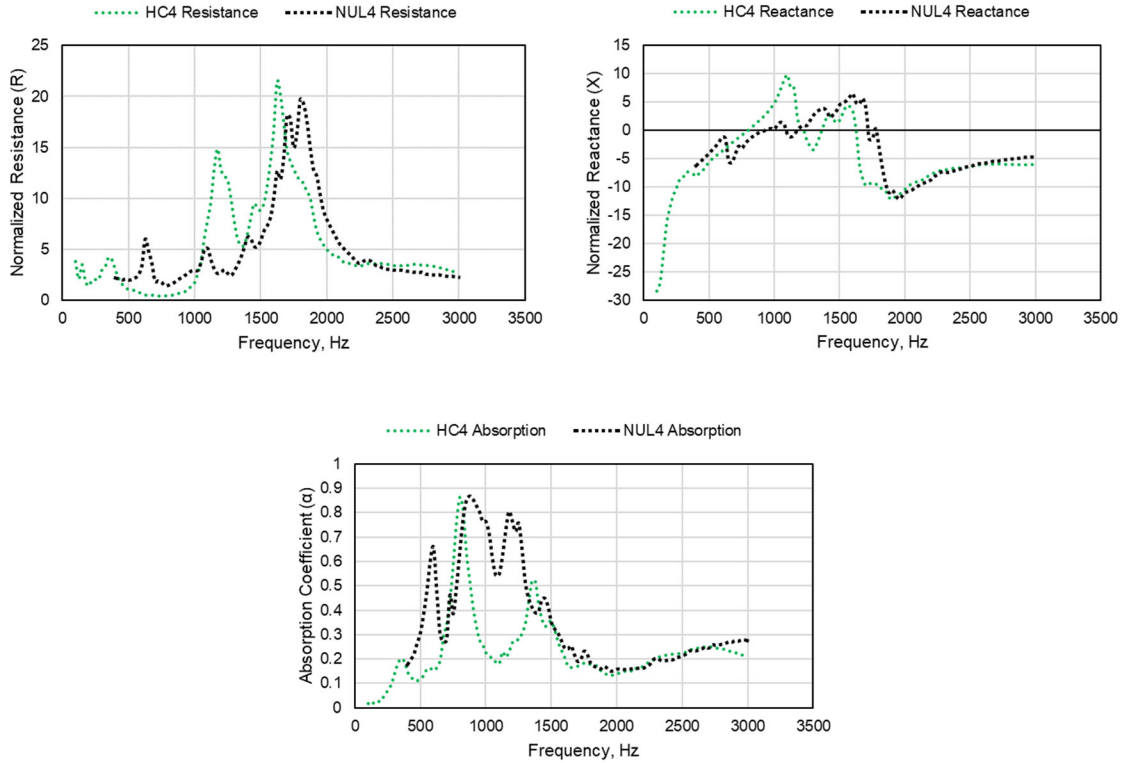
Figure 32: Comparison between the uniform and non-uniform MEL impedance (left) and absorption coefficient (right)

The low-frequency performance benefits obtained by the non-uniform MEL configuration are clearly seen when comparing to a similar uniform MEL configuration. The NUL concept shows an absorption peak at ~575 Hz with more broadband peaks following from ~800 Hz and extending to ~1300 Hz. The HC concept shows one dominate peak at ~750 Hz with a second, much smaller peak, at ~ 1400 Hz. By altering the membrane geometry in order to tube the liner for a particular frequency range, one can achieve a low-frequency attenuating broadband absorber in a relatively compact form factor.

2.5.2.4. Non-Uniform MEL Simulation Comparisons

The following charts show a comparison of the NUL2 and NUL4 test cases with simulations.
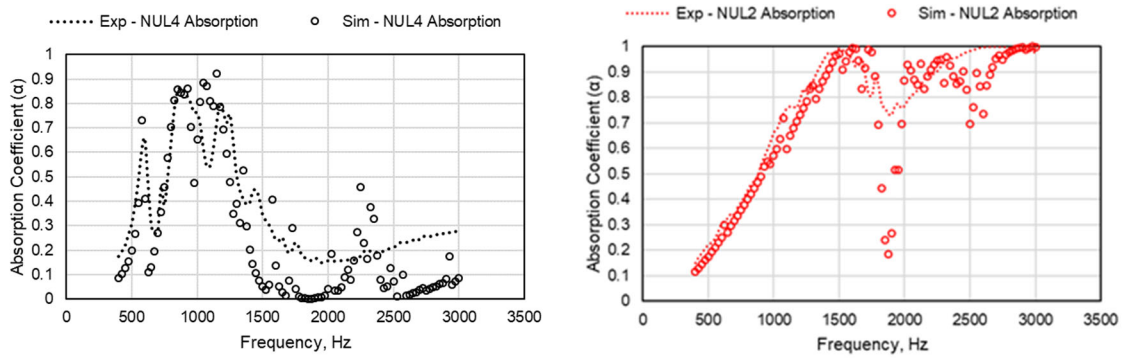
Figure 33: Comparison between simulation and experiment for non-uniform membrane-embedded liner

Figure 33 shows that the simulations for non-uniform MEL agree with the experiment very well, as the majority of the absorption peaks are captured. The absorption peak in the simulation occurring around 2300 Hz is likely a product of the lack of viscous losses incorporated within COMSOL simulations. In general, the trends in the absorption coefficient are achieved.

2.5.3. Slanted MEL

Figure 34 compares the slanted MEL with and without a 4% open area facesheet.
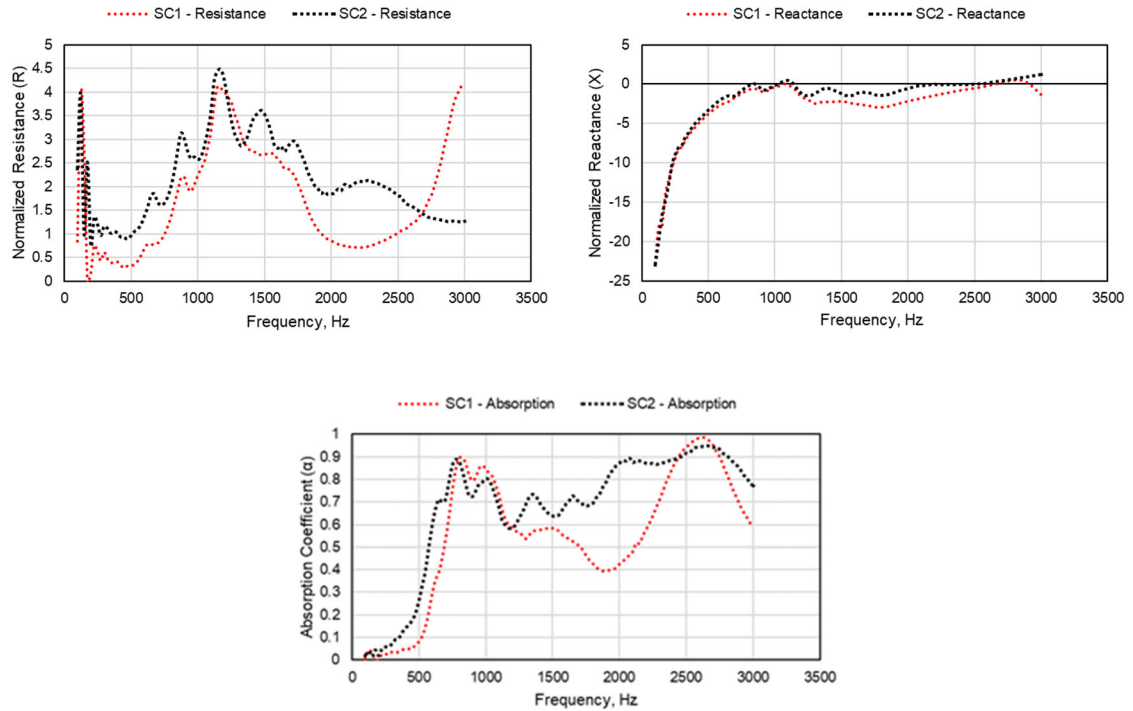
Figure 34: Slanted cavity acoustic response where SC1 test cases contain no facesheet, and SC2 test cases contain a 4% open area facesheet. Resistance (top left), reactance (top right), and absorption coefficient (bottom)

The hypothesized benefits for developing a slanted cavity test sample are confirmed as seen in the figure above. The low-frequency benefits are seen with a resonance peak at ~800 Hz with adequate broadband performance in both test cases with and without a facesheet included. The performance range for this variable depth membrane-embedded concept starts around 575 Hz and extends throughout the rest of the test frequency range.

2.5.4. 5x5 Membrane-Embedded Liner

2.5.4.1. Baseline 5x5 Membrane-Embedded Liner

The baseline 5x5 MEL experimental test results and the mass-attached 5x5 MEL test results are

presented in Figure 35.
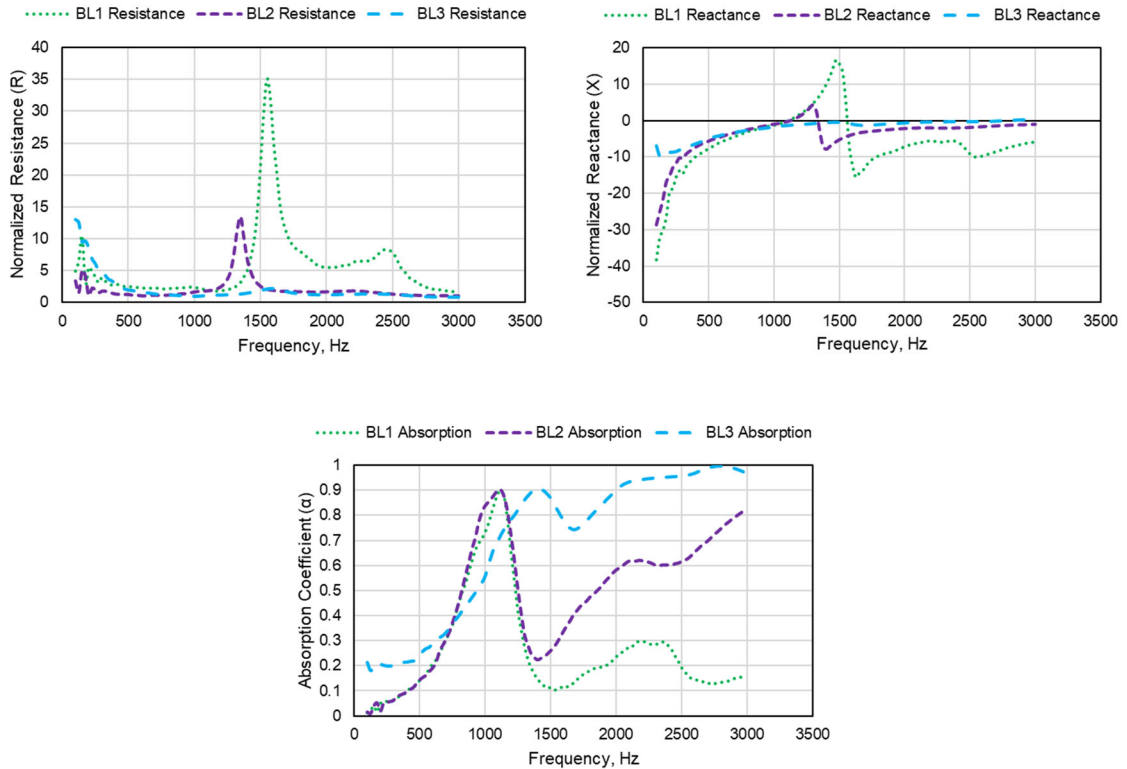
Figure 35: Baseline experimental test results for the 5x5 MEL, resistance (top left), reactance (top right), absorptions coefficient (bottom left)

Similar to the sister 3x3 uniform MEL test case, the same trends are observed with nothing out of

the ordinary occurring. Both BL1 and BL2 contain the same absorption coefficient spectra as

shown in HC4 and HC5 with a similar occurrence for the BL3 as shown in HC6. The normalized

resistance and reactance follow the same trend seen in the corresponding HC4-HC6 test

configurations.

2.5.4.2. Added Mass 5x5 Membrane-Embedded Liner

The following chart (Figure 36) is a comparison of the acoustic performance when an added mass is affixed to the center of each cavity. Recall there are three different masses that are being tested in this section.
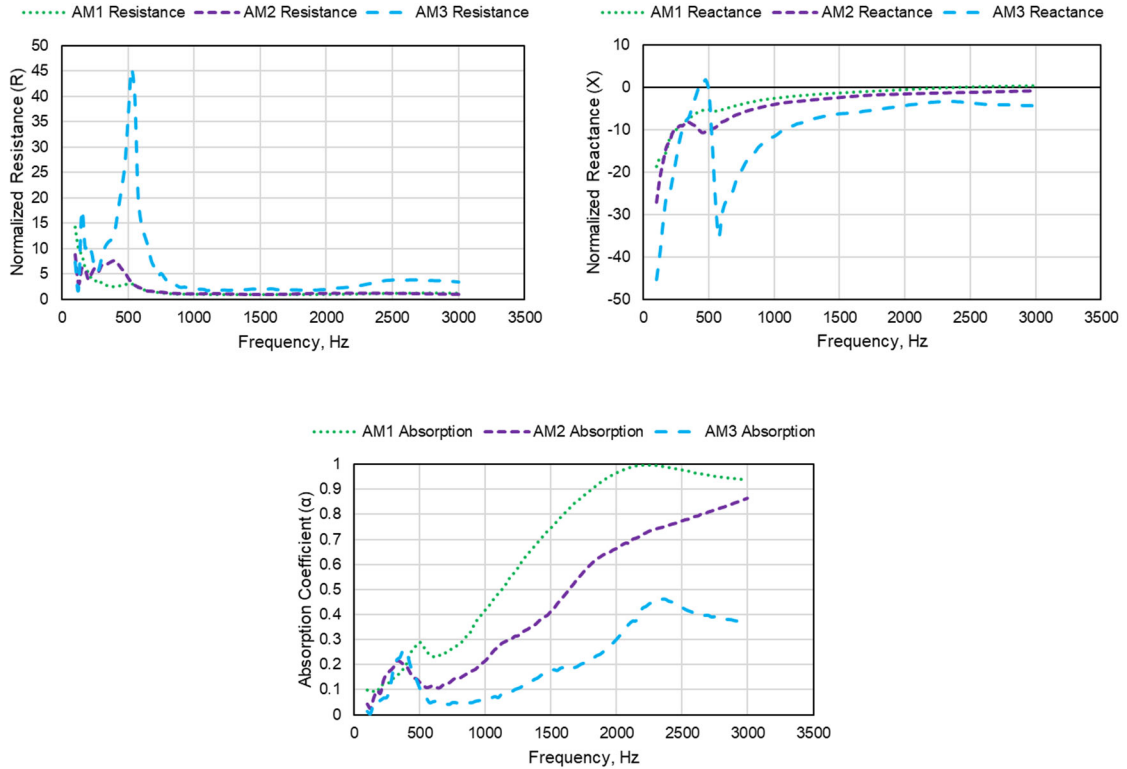
Figure 36: Experimental test results for the 0.027 g added mass case, resistance (top left), reactance (top right), absorption coefficient (bottom left)

By adding the 0.027 g mass to the center of the membrane in each cavity, an absorption peak is seen around 400 Hz for AM1 and AM2 with a gradual increase in the performance thereafter. AM3 retains an absorption peak at 500 Hz with a similar increase in performance as AM2. This mass addition yields a significant low-frequency performance hit likely due to the weight of the added mass relative to the membrane.
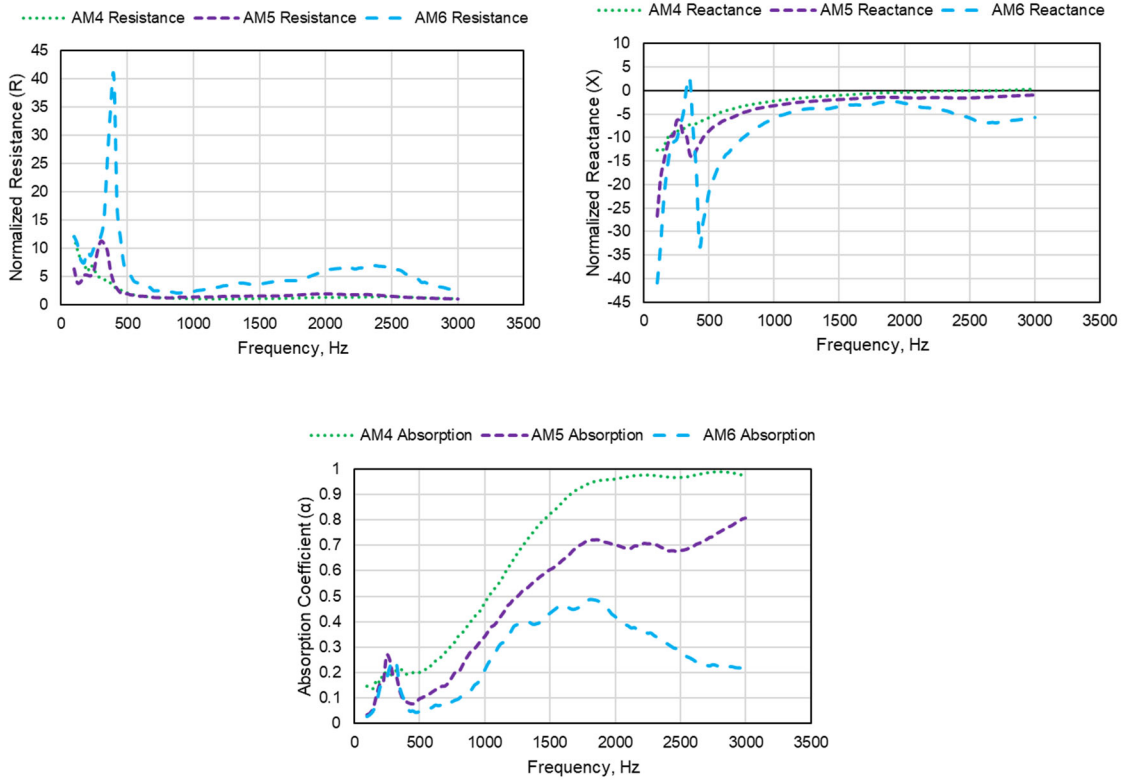
Figure 37: Experimental test results for the 0.035 g added mass case, resistance (top left), reactance (top right), absorption coefficient (bottom left)

Increasing the weight of the added mass to 0.035 g results (Figure 37) in an absorption peak

located at 325 Hz for all three configurations, with the higher frequency performance (after the

initial peak) following a similar trend as in the previous test case for the 0.027 g.
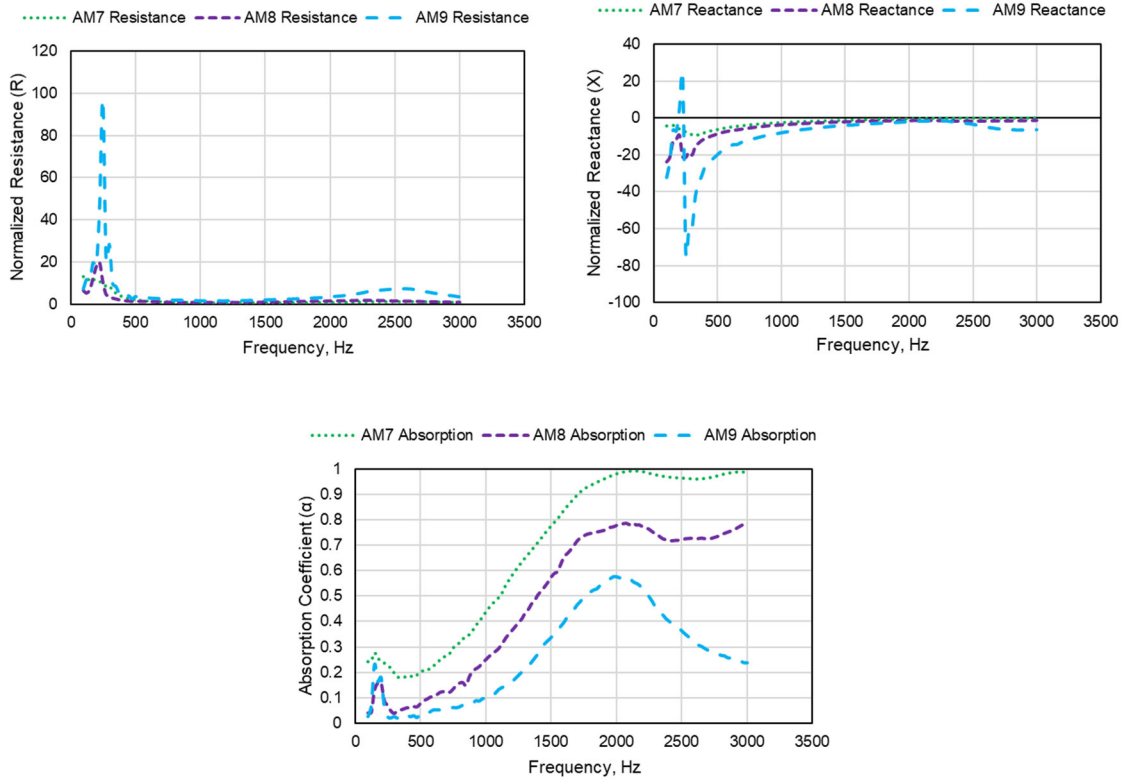
Figure 38: Experimental test results for the 0.102 g added mass case, resistance (top left), reactance (top right), absorption coefficient (bottom left)

For this last configuration (Figure 38) using a 0.102 g attached mass to the center of the membrane in each cavity, the absorption peak shifts even more as expected using the heavier mass and yields an initial absorption peak for all configurations at 200 Hz. Like the previous two datasets, after that initial peak, there is an upward trend in the absorption performance. It is very clear that the result of the added mass for these three datasets results in too great of an impact on the low-frequency acoustic performance. However, the initial hypothesis that using incrementally heavier masses lead to lower and lower initial resonant peaks is confirmed.

2.5.4.3. Added Mass 5x5 MEL Simulation Comparison
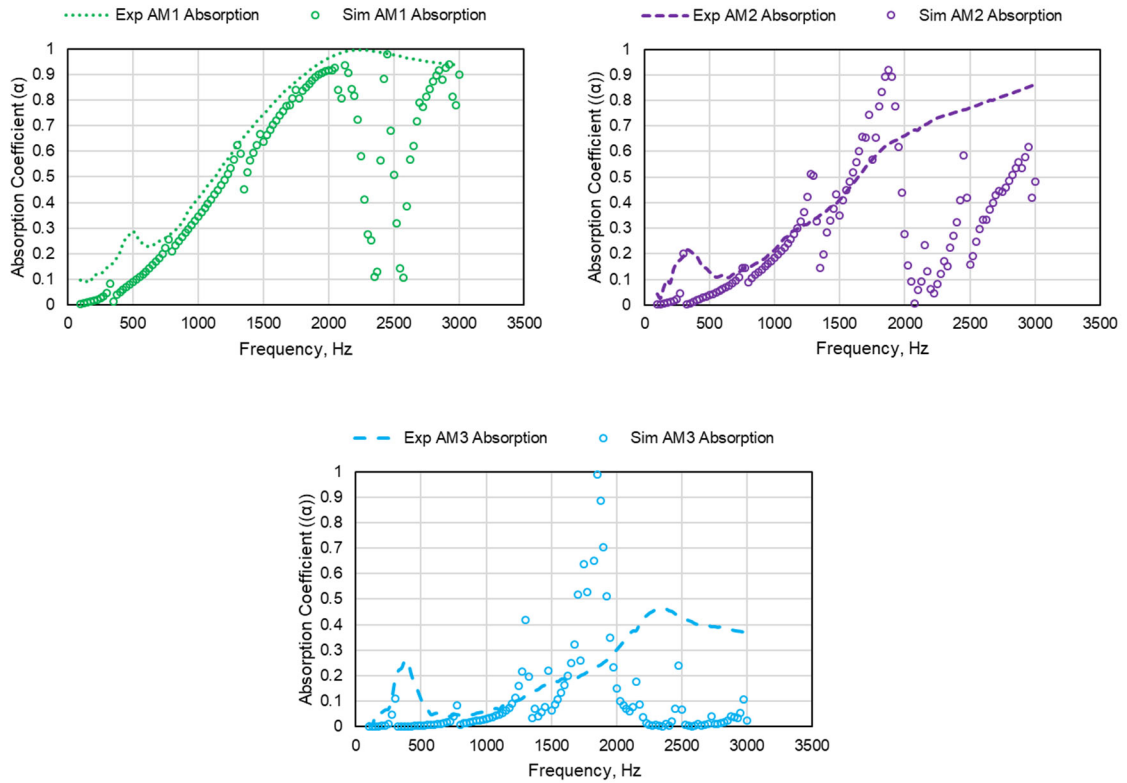
Figure 39: 0.027 g added mass simulation comparisons for configurations AM1 (top left), AM2 (top right), and AM3 (bottom)

Attempts were made in order to model the added mass test cases AM1-AM3. This complex system was difficult to model but made possible using the solid-structural Multiphysics interface between the pressure acoustics physics interface and the membrane module which includes the capability to implement an added mass. The simulation model for AM1 more closely matches the experiments than the other two (AM2 and AM3). Although the simulations for AM2 and AM3 don't match perfectly, they do seem to follow a similar trend as the experiments.

2.6. Chapter Summary

Chapter 2 provides a detailed description of the membrane-embedded liner experimental tests and simulations conducted to evaluate the low-frequency acoustic performance of this liner concept. A description of the membrane tensioning process is discussed as well as a validation for the analytical membrane tension calculation using experiments and simulations. Three different models are developed using COMSOL Multiphysics, one for the uniform MEL, one for the non-uniform MEL, and one for the added-mass MEL. Each of the relevant simulation design concepts is compared to the corresponding experimental test and display good agreement. The added-mass case utilized the software's multi-physics capabilities to couple the acoustic-structure interaction, and overall, captures many of the general characteristics of the absorption coefficient curve that are observed in experiments although large modal excursions are seen in the simulations; which is explained due to the lack of simulated losses that inevitably occur in the actual experiment. Additionally, efforts were successfully made to verify the proof of concept using a mass-attached membrane within an acoustic liner in order to obtain a much lower fundamental membrane resonant frequency.

A traditional SDOF or 2DOF liner concept with a total height of ~3.81 cm should have a resonant frequency of around 2250 Hz (according to quarter-wave theory). The MEL provides multiple low-frequency peaks (<~1000 Hz) broadband noise mitigation above $\alpha = 0.6$ given the same total thickness.

The influence on membrane height within a cavity is seen to have a notable impact on the acoustic performance and can be used as a tuning mechanism. If a more broadband response is desired, placing the membrane towards the bottom of the cavity is desirable, but if a low-frequency tonal response is desired, placing the membrane near the surface of the liner will suffice. But if both, low-frequency and broadband noise mitigation is desired, using a NUL

configuration with the membrane located near the surface of the liner will give that response. For a visual comparison of the MEL and NUL see Figure 32. Discoveries are made on the effects on the location of the membrane height throughout a liner cavity. When the membrane is near the surface of the liner, the acoustic particle velocity is nearing zero, in other words, the pressure is nearing a maximum and the membrane's modal resonant response is more clearly seen. Furthermore, in attempts to take advantage of placing the membrane near the top as well as near the bottom, a slanted cavity design and manufactured and tested. Results indicate that this configuration does in fact display the acoustic characteristics desired. More information on this mechanism can be found in Appendix A1. This enables potential optimization of future liner MEL designs for a particular application requiring either low-frequency tonal noise mitigation or broadband mid- or low-frequency noise mitigation.

Various similar configurations were discussed throughout the literature review and using the theoretical designs and experimental data in membrane-embedded liner concepts, an extensive investigation into the underlying mechanism is commenced.

CHAPTER III

Folded-Cavity Liner

3.1. Overview

The folded-cavity liner (FCL) concept consists of multiple sets of resonators of different lengths which are folded together in a convoluted manner in order to obtain an ultra-compact liner concept. The basis for the liner concepts was developed using quarter-wave theory for an acoustic resonance through a duct, which is then verified using the propagation wave model outlined in the next section. Throughout this section, there are 4 different design concepts that were manufactured and experimentally tested, and then analytically verified.

3.2. Concepts and Designs

The Zwikker-Kosten Transmission Line (ZKTL) model is an impedance prediction code that is used in this case to evaluate the performance of the FCL concepts [66, 67]. This wave propagation code is equipped to handle a variety of liner configurations due to the nature of its architecture [68, 69]. The ZKTL model in this study is implemented using MATLAB. For example, a liner that consists of a facesheet, honeycomb, and a back-plate can be modeled using the ZKTL code with 2 layers. The code essentially splits the liner into layers, where each element that the acoustical sound waves encounter within the acoustic liner will be accounted for starting from the back-plate and up to the surface of the liner. This method begins with the assumption that the backplate is rigid, thus it is known that the particle velocity is 0, and the pressure is assumed to be 1 (at the backplate). Next, working through the transfer function for an empty duct, up to the next layer which for conventional designs could be a perforate facesheet or a wire mesh, computing the transfer matrix for either of those layers reaching the surface of the liner, the surface impedance can then be found. This method has been extensively used and validated by the folks at NASA Langley [70].

Using ZKTL to model several variations of FCL concepts, a series of ultra-compact liner configurations are optimized and chosen for low-frequency broadband performance. The methodology to developing ultra-compact liners implements a 1.27 cm aluminum honeycomb core and a facesheet and back-plate. The honeycomb core is manually altered to allow the passage of sound between multiple connected cells. This is essentially folding one or multiple long cavities until they reach the desired cavity length. In these cases, a special facesheet is designed to prevent sound from escaping or creating a non-local reacting liner. Instead of having a facesheet with a nominal areal porosity across the entire surface, the first cell of the multiple connected cells has an areal porosity and the other cells are closed off. Using this method, low-frequency broadband noise mitigation (<1000 Hz) is possible for such a compact configuration.

62

The first FCL concept is primarily designed to target specifically low frequencies between 500 Hz and 600 Hz. This design has 3 sets of resonators which have a resonant frequency of 519 Hz, 562 Hz, and 613 Hz, respectively. Set 1 contains 3 groups of interconnected cavities, sets 2 and 3 contain 2 groups of interconnected cavities. The second FCL design concept targets a more low-frequency broadband frequency range with hopes to obtain adequate absorption between 500 Hz and 900 Hz. This concept contains 5 sets of resonators that resonate at 422 Hz, 519 Hz, 675 Hz, 844 Hz, and 896 Hz, respectfully. Sets 1 and 5 contain 1 group of interconnected cavities and sets 2, 3, and 4 have 2 groups of interconnected cavities. The third FCL design went through a few iterations in an attempt to optimize the magnitude of the absorption coefficient for as low of a frequency range as possible and the resulting frequency range targeted is between 500 Hz and 700 Hz. This design concept, which consists of 4 sets of resonators, with target frequencies of 536 Hz, 574 Hz, 636 Hz, and 698 Hz, respectively. Set 1 contains 3 groups of cavities, set 2 has 1 group of cavities, and sets 3 and 4 both have 2 groups of interconnected cavities. The fourth and last FCL design considered in this case study targets broadband absorption which peaks around 1000 Hz. This design, like design 3, also has 4 sets of resonators which target 536 Hz, 784 Hz, 1040 Hz, and 1224 Hz, respectively. The first and second set of interconnected cavities for FCL design 4 only has 1 group, the third set contains 5 groups of joined cavities and the last set has 7 groups of connected cavities. Each of the FCL concepts are outlined in Table 8.

Table 8: FCL test configurations

Case Number	Target Frequency Range, Hz	Number of Resonator Types
FC1	500 - 600	3
FC2	500 - 900	5
FC3	500 - 700	4
FC4	500 - 1200	4
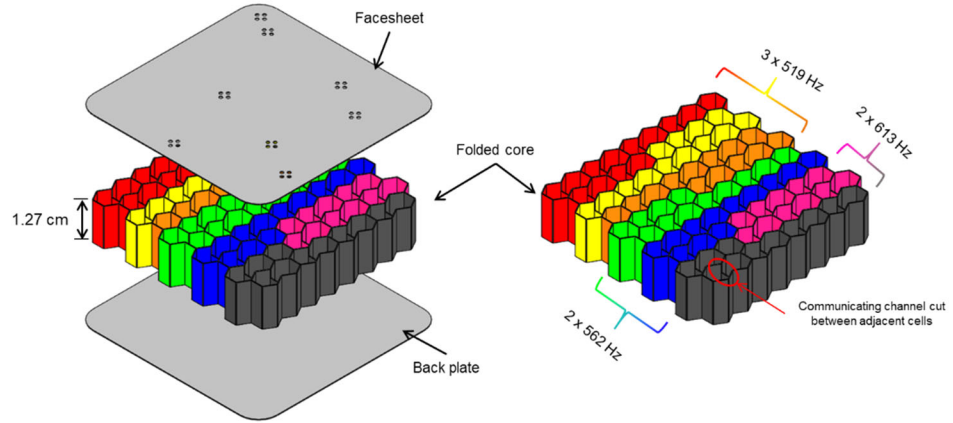
Figure 40: Design details for folded-cavity liner design-1 (FC1)
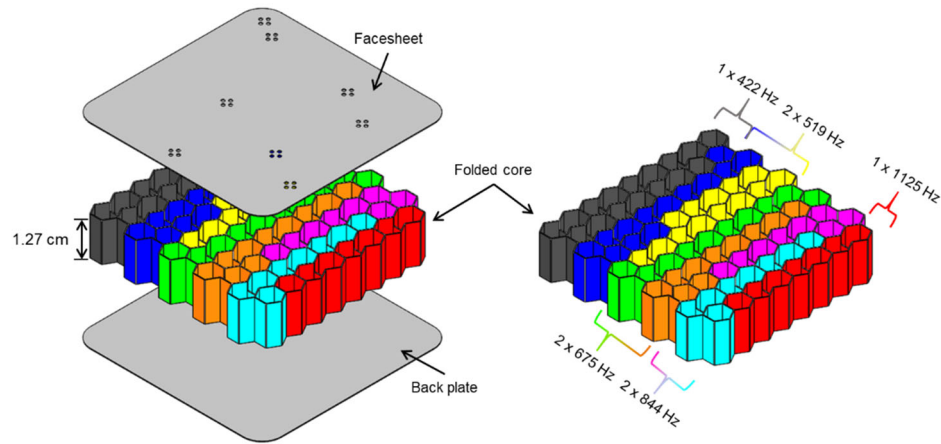
Figure 41: Design details for folded-cavity liner design-2 (FC2)
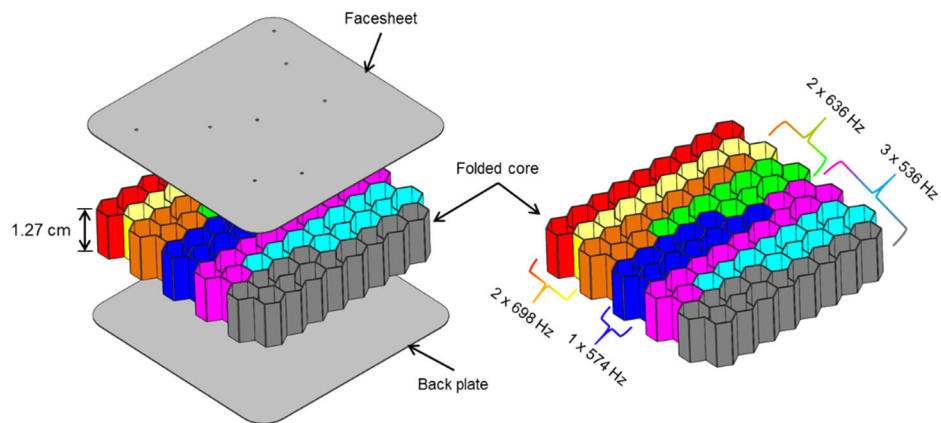
Figure 42: Design details for folded-cavity liner design-3 (FC3)
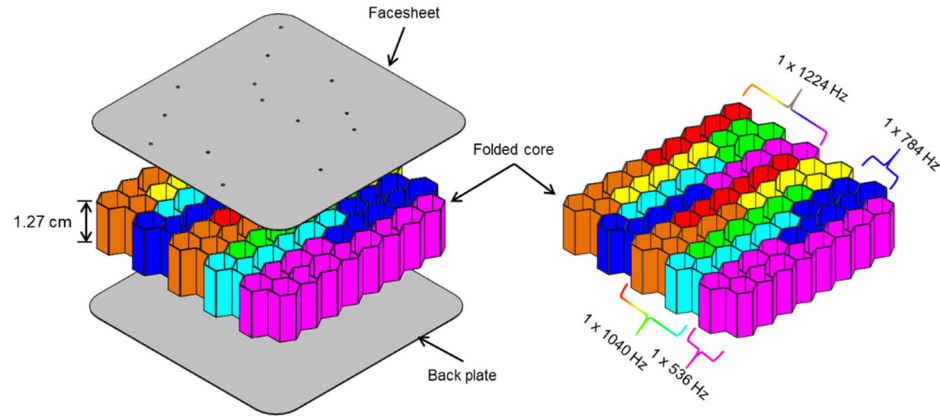
Figure 43: Design details for folded-cavity liner design-4 (FC4)

3.3. Modeling

Numerous ultra-compact designs are investigated within this paper. Initially, a simple proof of concept is desired to ensure that nothing obscure happening within the quarter-wave calculation for the resonance frequency. Additionally, to ensure that all of the physics are being captured properly, each design is modeled within ZKTL and the data is extracted to be compared with future experiments. In practice, to test the liner designs for a 1.27 cm thick honeycomb which has a nominal cavity diameter of 0.635 cm, the bulk material must be cut into 6.35 cm x 6.35 cm sections to account for the maximum test sample size in the impedance tube at Oklahoma State University. There are nominally 85 open cells within that area, so each configuration must use 85 cells so that there is no wasted space.

3.4. Experimental Methods

The FCL concept designs were experimentally tested using the impedance tube located on campus at Oklahoma State University.

3.4.1. Oklahoma State University Impedance Tube

The tube at Oklahoma State University uses ASTM E2611-09 for the method for measurement of normal incidence sound transmission of acoustic materials based on the transfer matrix method [71, 72]. For this configuration, the upper-frequency limit is about 2700 Hz based on the cross-sectional dimensions of the tube and the lower frequency limit, which depends on the microphone spacing, is calculated to be 68 Hz. But in practice, and with the particular equipment used the working frequency range which we are interested in is from 200 Hz – 2500 Hz. The Kicker driver allows a partial overall sound pressure level of about 110 dB. The data acquisition is done using a LABVIEW program which is connected to a DAQ and a signal generator to produce the random noise used for all of the testing in this section. The data acquisition is done using a LABVIEW program which is connected to a DAQ and a signal generator to produce the random noise used for all of the testing in this section. The microphone data obtained from LABVIEW is processed using a program written in MATLAB, following the aforementioned Standard, to compute the acoustic properties. A schematic of the entire setup is provided in the following figures as well as a photograph of the actual tube in the configuration used for impedance measurements.
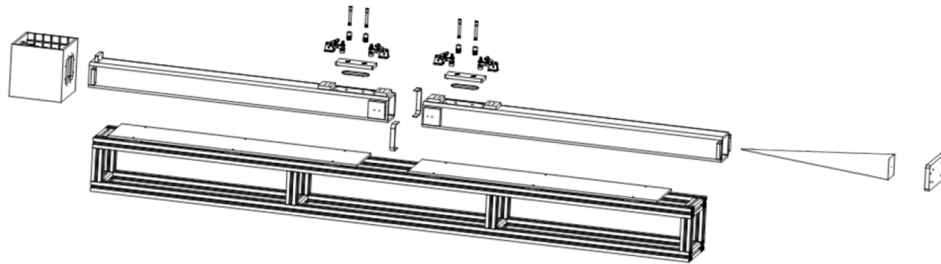
Figure 44: Schematic of the OSU impedance tube (in its complete form)

It should be noted that the setup described in Figure 44 is setup to do transmission loss measurements. However, for the tests conducted in this thesis, the right half of the tube is not applicable but the schematic can be used to better describe the actual photo of the impedance setup in Figure 45.

Figure 45: OSU Impedance Tube

Since the facesheet used for these experiments is not a typical facesheet, special consideration is taken to ensure that the orientation of the liner does not have a significant effect on the acoustic performance. In doing so, each liner is first marked at the top corner where the "first" set of interconnected cavities starts. A test is performed and then the liner is removed from the sample holder, rotated 90-degrees, and then tested again. After extracting the acoustic response for the liner orientation of each case, the data is compared and then averaged. That data is then compared to the simulations in the next section.

3.4.1.1. Estimation of OSU Impedance Tube Repeatability Error

In order to better understand the various uncertainty in repeatability that is involved with the data acquired by the OSU impedance tube, multiple tests were conducted on design concept FCL1 at the time of testing. On another day, a retest of FCL1 was conducted as to better determine the repeatability uncertainty that may occur between testing days. There are a few variables that can contribute to the uncertainty between tests when running these experiments, these variables can be separated into two categories, environmental factors and human factors. The environmental variables are related to the local temperature, humidity, and pressure. A description of the human factors are as follows, one of these errors involves the actual insertion of the test sample and how

the sample holder is fitted flush against the waveguide. On the same note, the back-plate of the sample holder can be adjusted to account for various sizes of test samples, if the back-plate adjustment is altered between tests this could contribute to the repeatability error. On the sample holder there are 4 bolts that are used to mount it to the waveguide, which gives an opportunity to leave a very small air gap that can lead to slight variations in measurements at the upper and lower frequency limits and add additional noise to the measurement. One other factor that is specific to the FCL designs is the orientation of the sample, because each of the FCL designs contains a non-uniform facesheet, the orientation of the test sample relative to the measurement microphones is a crucial factor. For example, if the sample is placed with more perforation holes near the measurement microphones then the sample is rotated 180 degrees, this may lead to irregularities in the measured surface impedance. Another potential source for error to occur is the microphones, to ensure that the microphones are operating properly and can retain a proper calibration, the microphones and the piston-phone sound level calibrator would need to be sent to a metrology lab.

Within the same run, consecutive tests on a test sample have shown to produce minimal error as shown in the appendix of Chambers [48] thesis. To reconfirm these results, a similar plot is provided where FCL1 is tested twice where both datasets (i.e. FCL1 Test 1 and FCL1 Test 2) are shown. Additionally, that data was averaged, and error bars were added to represent the uncertainty in measurements between these consecutive runs.
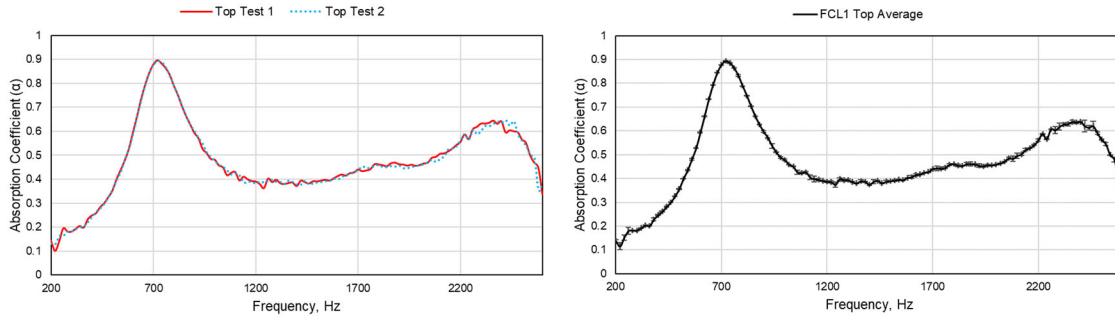
Figure 46: Comparison of consecutive tests on FCL1 in the top orientation conducted back-to-back (left), averaged test data with the consecutive-test error bars included (right)

In the analysis of the test data shown by Chambers, the measurement uncertainty for consecutive tests was seen to be around 1.7%. For the comparison of FCL1 test 1 and test 2, the averaged uncertainty over the 200 Hz to 2600 Hz bandwidth is around 1%. The difference for this comparison is the frequency bandwidth in question. Chambers used the resonance bandwidth for the sample in question, if the same is done for the test case shown above, the measurement uncertainty for the resonant bandwidth (500 Hz – 1000 Hz) is less than 0.5%. Therefore, there is very little error in the experimental absorption coefficient data attributing to variations within consecutive trials.

As mentioned earlier in this section, the orientation of the test sample can have an influence on the computed acoustic spectra. Thus, a series of tests were conducted by rotating the FCL1 test sample 90 degrees, for these tests there were two consecutive tests averaged together and shown in the figure below.
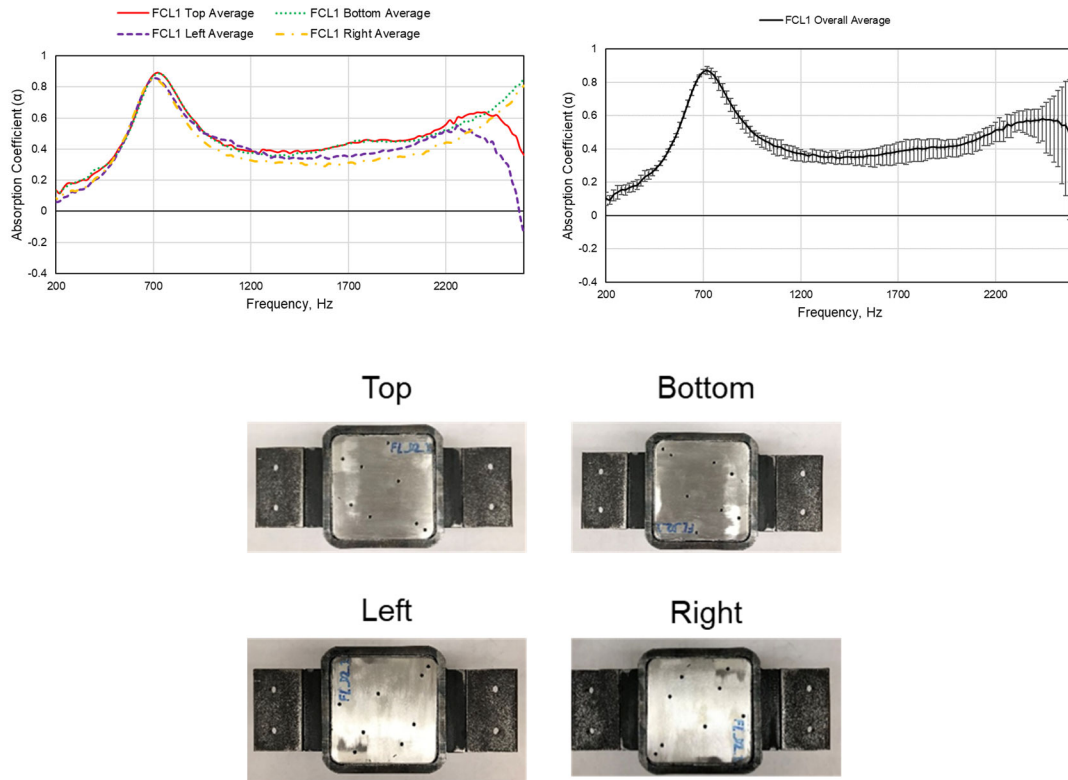
Figure 47: Comparison of the averaged orientation tests for FCL1 (top left), overall average for the FCL1 with error bars produced from the orientation tests (top right), schematic of the test sample orientation (bottom)

These four test cases shown in Figure 47 on the left were averaged and shown in one line in the plot on the right, with error bars placed on the data series to represent the potential error due to the orientation of the test sample. Around the resonance (500 Hz – 1000 Hz) the uncertainty in the measurement is just over 2%.

Taking the averaged data shown in Figure 47 on the right, a retest of FCL1 in the top orientation was conducted on a different day to investigate the uncertainty in the day to day acoustic measurements.
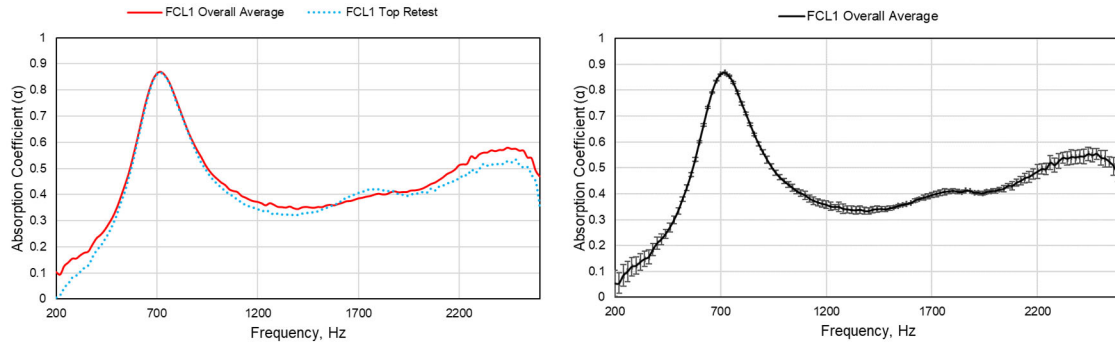
Figure 48: Comparison of the overall averaged data from the orientation study compared against a retest of FCL1 in the top orientation (left), and the overall averaged data with error bars (right)

The comparison shown in Figure 48 yields an overall averaged error for the entire bandwidth shown to be around 1.5% but for the resonance range (500 Hz – 1000 Hz) the averaged error is again less than 1%.

Through the analysis of the potential run to run error for the OSU impedance tube, it became clear that the main factor that effects the measurement for these samples is the orientation. This is but one example of why it is crucial to have a consistent testing regimen in hopes to minimize all of these potential errors. Throughout the rest of the data shown that was taken using the OSU impedance tube, a consistent testing regimen is implemented to ensure minimal uncertainty.

3.4.2. Fabrication

To validate simulation results with experiments, test samples were designed and manufactured by an off-campus affiliate, the New Product Development Center (NPDC). These test samples are manufactured by hand so inevitably there will be some margin of error associated with the impedance eduction testing. These liner concepts are made out of a 1.27 cm-thick, 0.635 cm-diameter, aerospace-grade aluminum honeycomb. Additionally, the facesheet and back-plate are constructed out of 0.15875 cm-thick aerospace-grade aluminum. The method used by the NPDC to machine out part of the wall to create the adjoining cells is by using a small pair of sewing

71

scissors. To ensure that the interior cuts are roughly the same length, a template is 3D printed that contains nubs (of a certain length) which are inserted into the honeycomb, from there the cuts can be made. Figure 49 shows an example of the aforementioned 3D printed template. Once the cells have been modified (as shown in Figure 50) the aluminum facesheet and back-plate can be bonded to the corresponding sides of the honeycomb (as shown in Figure 50).
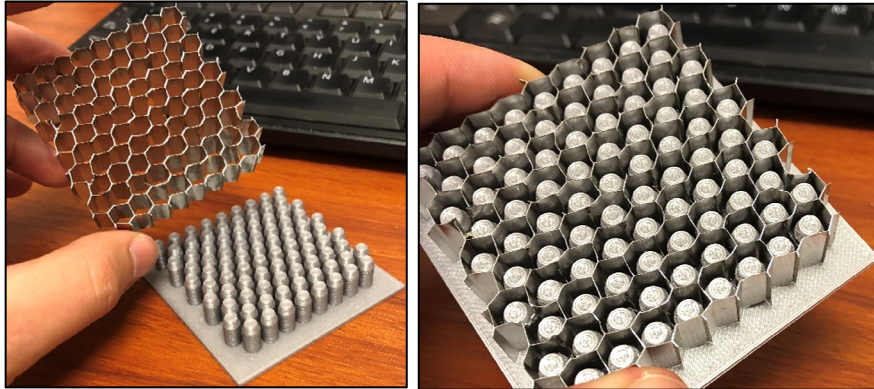
Figure 49: 3D printed template used to house the honeycomb when modifying cell walls, separated honeycomb and template (left), honeycomb placed on the template (right)
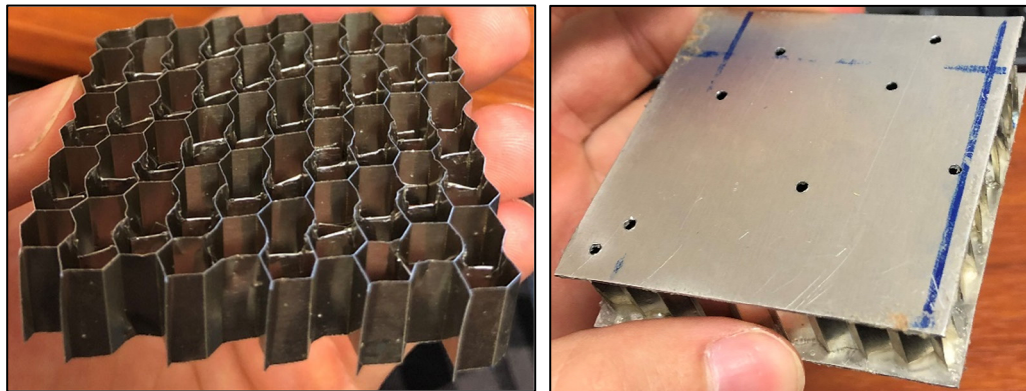
Figure 50: Folded cavity manufacturing sample, example of the cut-outs utilized to adjoin consecutive cavities (left), finished product with perforated facesheet (right)

Photos of the as-tested FC3 and FC4 designs are shown in Figure 51 below. Again, FC3 is targeting a frequency range between 500 Hz – 700 Hz, and FC4 targets a frequency range of 500 Hz – 1200 Hz. The internals of these two test samples is shown in Figure 42 and Figure 43.
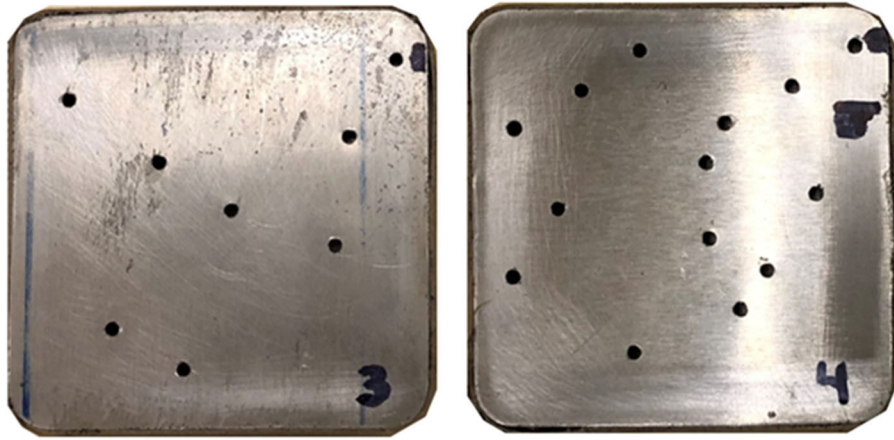
Figure 51: Photographs of the folded-cavity liner test articles FC3 (left) and FC4 (right)

3.5. Discussion of Results

As mentioned in a previous section, the simulated folded cavity absorption coefficient is compared with the averaged experimental absorption coefficient over multiple tests for each test configuration. The comparison is provided in the following 4 plots (Figure 52) in this section.
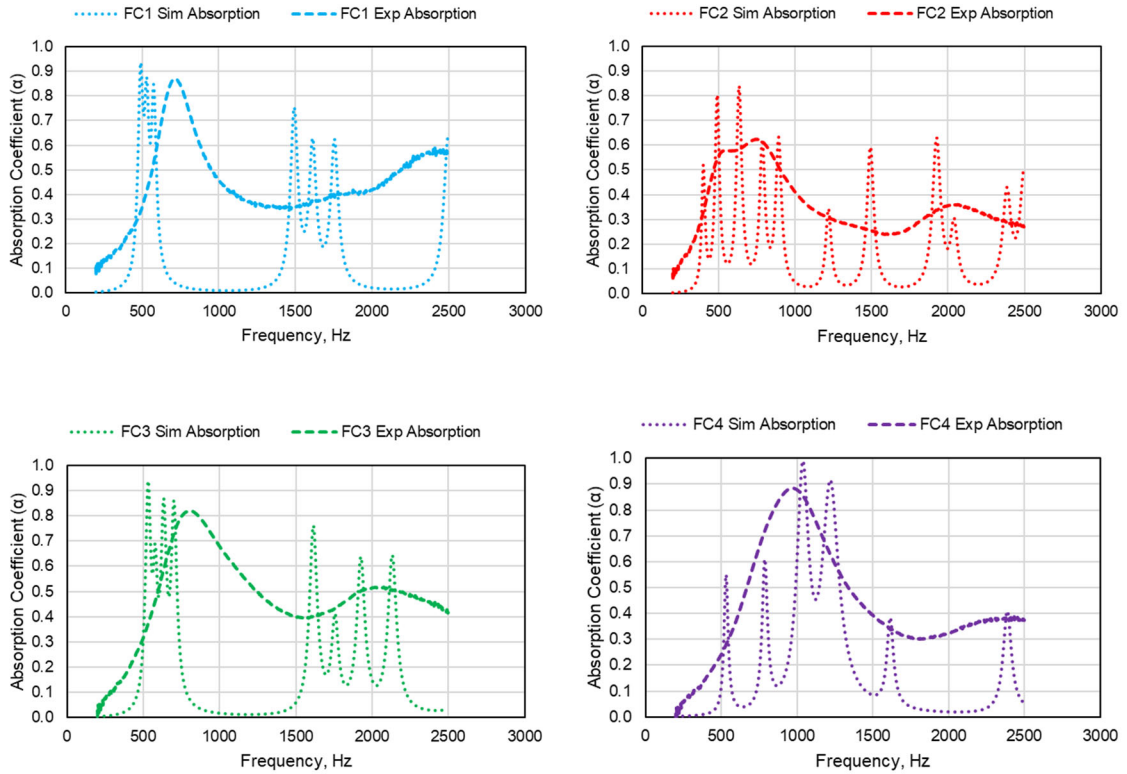
Figure 52: Experimental vs simulated absorption coefficient for FC1 (top left), FC2 (top right), FC3 (bottom left), and FC4 (bottom right)

For FC1 the simulations appear to be missing the peak location by about 200 Hz compared to the experiments, each of the individual peaks was not expected considering some of the results observed in Chambers thesis. However, there is an extra source of error that can be associated with the FC1 test sample. During the manufacturing of this test sample, the cutouts that were made to adjoin each of the sets of cavities together were not completely removed. Since this was somewhat of a test run for the manufacturability of the test articles, the manufacturing process was still being optimized. So, to join all of the cavities together, there were slits cut on each side of the wall and the piece that should be removed was crimped down flat. This extra piece of material may be adding an extra bit of resistance which may result in the mismatch in the simulation. For FC2-FC4 the aforementioned material was removed from the liner by means of a Dremel tool. By removing the extra material, the experiments much more closely match the predicted acoustic response.

74

3.6. Chapter Summary

Chapter 3 provides a detailed description of each of the folded-cavity liner (FCL) design concepts considered in this study. These designs are modeled using the Zwikker-Kosten Transmission Line model for predicting the impedance and absorption for various FCL concepts. Using information obtained from the work that Chambers [48] conducted on folder cavity liner concepts, a new series of ultra-compact, low-frequency absorbing, liner configurations with performance optimized for low-frequencies was considered. Thus, based on modeling, four ultra-compact designs were chosen for manufacturing via an off-campus affiliate and experimentally test using the Oklahoma State University Impedance Tube. The ZKTL model compares favorably with the experiments with these ultra-compact liner designs with the exception of the first concept (FCL1) which displays a more notable difference between the experiment and the simulation than the other configurations. This source of error likely stems from the manufacturing process, whereas the process to modify the honeycomb was still in a beta process and the material that is removed from the other test cases remains in FCL1. This added resistance promotes additional viscous losses resulting in the discrepancies between the experiment and the simulation. The other experiments for test cases FCL2 – FCL4 more closely match the predicted acoustic response. This displays with some certainty that it is possible to target a specific frequency bandgap and design a liner that will resonate closely to that target.

With a total thickness of 1.27 cm, broadband absorption is achieved in the frequency range of 500–1000 Hz. For the FCL, which relies on creating convoluted acoustic paths within a confined liner volume, an optimal combination of resonator frequencies and facesheet porosity is essential to maximize low-frequency absorption performance. The ability to tailor the absorption peaks for low-frequency bandwidths and retain broadband mitigation characteristics using folded-cavity liners is shown using experiments and verified by comparing the results with the simulation predictions.

CHAPTER IV

Carbon Foam Liner

4.1. Overview

Rigid open-cell foams have been studied and utilized in various industries for decades, but in the more recent years, the benefits of their potential acoustic properties, if designed and manufactured right, can result in a great bulk absorber. If designed with particular properties, low-frequency absorption below 1000 Hz is possible within a compact form factor. Among the many types of foams used in structural-acoustic applications, Carbon-based foams offer several multifunctional advantages. In addition to their acoustic properties, fire resistance, low density, and high strength, their excellent thermal properties make them well-suited for structural applications with an emphasis on heat management. This section presents the investigation of the influence of thickness, spacing, and membrane interaction on the acoustic properties of rigid, open-cell carbon foam. The carbon foam used in testing was sourced from CFOAM LLC. The foam produced by CFOAM and used in the studies presented in this chapter is a non-graphitic carbon-based foam [73]. The advantage of this structure compared to a graphitic foam for the application of potential acoustic liner concepts is the mechanical strength. A non-graphitic foam typically will have much higher mechanical strength compared to a graphitic foam. This foam is made from coal and on a large scale making it fairly affordable, when sourcing the foam, CFOAM happily donated some extra pieces of bulk material they had laying around.

4.2. Concepts and Designs

Two different classes of foams from CFOAM were evaluated for their acoustic properties, CFOAM 25 and CFOAM 30. The main difference between the two is the bulk density, which is 0.4 g/cm^3 and 0.48 g/cm^3, respectively. These foams are cut to length from bulk blocks using a band saw. Initially, the length and width dimensions considered are 5.08 cm x 5.08 cm to alleviate accounting for a specific fillet required for the experimental sample holder apparatus. For these cases, a sample adapter is inserted into the sample holder to account for the change in sample size. It is noted that the acoustic performance will take a slight hit, but the overall trend of the acoustic response will still be correct. To prove this, more time is taken to manufacture a select few 6.35 cm x 6.35 cm samples with the fillet to compare with the smaller cross-section test samples. Thicknesses of 0.635 cm, 1.27 cm, and 2.54 cm are considered to evaluate the influence of sample thickness. A summary of these baseline test cases is presented in Table 9 below.

Table 9: Summary of baseline carbon foam test cases

Case #	Description	Foam Thickness (t), cm	L x W, cm
BL – AC1	CFM25	0.635	5.08 x 5.08
BL – AC2	CFM25	1.27	5.08 x 5.08
BL – AC3	CFM25	2.54	5.08 x 5.08
BL – AC4	CFM30	0.635	5.08 x 5.08
BL – AC5	CFM30	1.27	5.08 x 5.08
BL – AC6	CFM30	2.54	5.08 x 5.08
BL – AC7	CFM25	1.27	6.35 x 6.35
BL – AC8	CFM25	2.54	6.35 x 6.35

Next, a few extra 0.635 cm thick CFM25 samples are cut to evaluate the influence of sample spacing. For these test cases, a 0.254 cm, 0.508 cm, 0.762 cm, or 1.27 cm air gap is established and maintained using tape for the acoustic testing. A description of these test cases is presented in Table 10.

Table 10: Summary of carbon foam spacing tests

Case #	Description	Spacing, cm	L x W x t, cm
S – AC1	CFM25	0.254	5.08 x 5.08 x 0.635
S – AC2	CFM25	0.508	5.08 x 5.08 x 0.635
S – AC3	CFM25	0.762	5.08 x 5.08 x 0.635
S – AC4	CFM25	1.27	5.08 x 5.08 x 0.635

To investigate the effect of the interaction of the carbon foam and a flexible membrane, using a drill press 4 holes are drilled into the carbon foam using a 1.27 cm drill bit. Additionally, to house a pre-tensioned membrane, septum plates are used to sandwich the membrane. The septum plates were designed in SolidWorks and then 3D printed in a similar fashion to the MEL septum plates. The tensioning rig is used to apply a semi-uniform tension to the membrane. Once the septum plates were affixed to the membrane, the unit was then placed between two 1.27 cm carbon foam test samples. Special consideration was taken into account for this complex membrane-embedded carbon foam system by cutting the 0.635 cm samples to the maximum length and width dimensions of 6.35 cm x 6.35 cm. To investigate the performance of this liner due to the membrane interaction, a test is conducted with the two carbon foam pieces sandwiching a set of blank septum plates. The tests conducted for this membrane-embedded investigation are outlined in Table 11.

Table 11: Membrane-embedded carbon foam test cases

Case #	Description	L x W x t, cm
M – AC1	CFM25 – Membrane	6.35 x 6.35 x 1.27
M – AC2	CFM25 – Blank Septum	6.35 x 6.35 x 1.27

4.3. Modeling

There are many modeling options when considering the acoustic properties of rigid open-cell foams, for this case, the Attenborough model, which is implemented in COMSOL Multiphysics, is used to simulate the porous media. This model is a continuation of the Zwikker-Kosten poroacoustics model and is based on a cylindrical-like pore assumption. Four parameters are used

to define the material for this semi-empirical model; porosity, flow resistivity, tortuosity factor, and a fitting parameter. Since this type of open-cell foam has not been studied extensively for its acoustic properties, these parameters are unknown and will have to be estimated based on other similar foams tested using this model. The initial guess is first made and then a parametric sweep is conducted by varying each of these parameters independently and then once the solution began to converge to the experimental results, some fine-tuning is done in order to obtain the final determination of the material parameters and presented below in Table 12.

Table 12: Material parameters for carbon foam used in COMSOL simulations

Parameter	Value
Porosity	0.95
Flow Resistivity, Pa.s/m^2	120000
Tortuosity Factor	30
Fitting Parameter	0.21

It should be noted that for the determination of these values, the 1.27 cm foam is first evaluated in the COMSOL simulations. Since the method used to obtain these properties is non-conventional, the validity of these parameters needs reinforcement. To alleviate these concerns, the same properties are used to simulate the 2.54 cm foam and compared with the experiment.

In case this is not sufficient evidence that the material properties are valid, the characteristic impedance of the carbon foam is computed using the 1.27 cm foam and the 2.54 cm foam. The Two-Thickness method is used to compute the characteristic impedance [74], this is a well-established model used to educe the intrinsic properties of bulk absorbing structures. Using the following equations as the core of the method:

$$\zeta_1 = \zeta_c \coth(\Gamma d_1)$$

Eq. 4.1

$$\zeta_2 = \zeta_c \coth(\Gamma d_2)$$

Eq. 4.2

Where ζ_1 and ζ_2 represent the impedance measured at the surface of two separate test samples with a thickness of d_1 and d_2. For this analysis, if d_2 is assumed to twice that of d_1, the analysis is

greatly simplified. The characteristic impedance and propagation constant can then be simplified

into the following equations:

$$\zeta_c = \sqrt{\zeta_1(2\zeta_2 - \zeta_1)}$$

Eq. 4.3

$$\Gamma = \Gamma_r + I\Gamma_i = \frac{1}{2d_1} log\left(\frac{1+a}{1-a}\right)$$

Eq. 4.4

$$a = \sqrt{\frac{2\zeta_2 - \zeta_1}{\zeta_1}}$$

Eq. 4.5

As long as the parent foams are sufficiently uniform when educing the characteristic impedance,

the impedance ζ_s of a third sample with thickness d_s can be determined using:

$$\zeta_s = \zeta_c coth(\Gamma d_s)$$

Eq. 4.6

This method was implemented using MATLAB and is presented in the appendix.

To ensure that the characteristic impedance is computed correctly, it is used to compute the

surface impedance and compared to the measured values for the two thicknesses used to educe it,

as a further check.

The application of these two models used to evaluate the performance of the carbon foam of

thicknesses that were not measured is examined. For these model comparisons, thicknesses of

1.905 cm and 3.81 cm is used.

4.4. Experimental Methods

The same method for computing the experimental impedance of the liners in the previous section is used for computing the impedance of the carbon foam liner concepts.

4.4.1. Fabrication

To fabricate the carbon foam test samples, bulk blocks of carbon foam were measured and marked so that cuts could be made using a bandsaw. Due to the rigidity of the material, no fragility complications were encountered. Once the foam was cut, finer modifications could be made using coarse sandpaper. The test samples were tapped against a rigid surface to knock loose any of the powdered carbon produced during the fabrication process. The fabricated test samples for AC1-AC6 are shown in Figure 53.
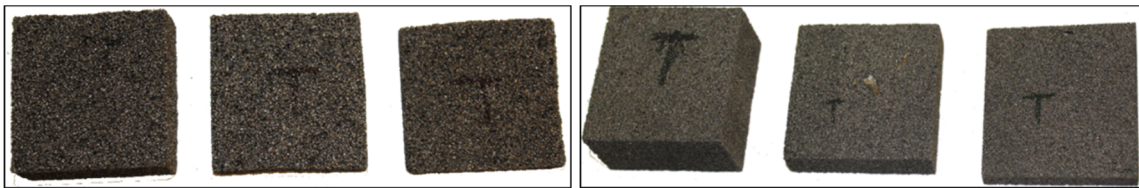
Figure 53: CFM25 (left) and CFM30 (right), post-fabrication

4.5. Discussion of Results

4.5.1. Carbon Foam Thickness Variation

The experimental impedance and absorption coefficient for the carbon foam liner concepts are shown in the figures below. As mentioned before, some of these experiments are chosen to compare with simulations. For all of these test cases, a 'top' and 'bottom' were assigned to each

CF sample and multiple tests were conducted on both sides to ensure that the properties of the foam throughout the sample were mostly uniform. A comparison of these results can be found in the appendix. For the sake of brevity, only one of the tests for each sample is provided in this section.
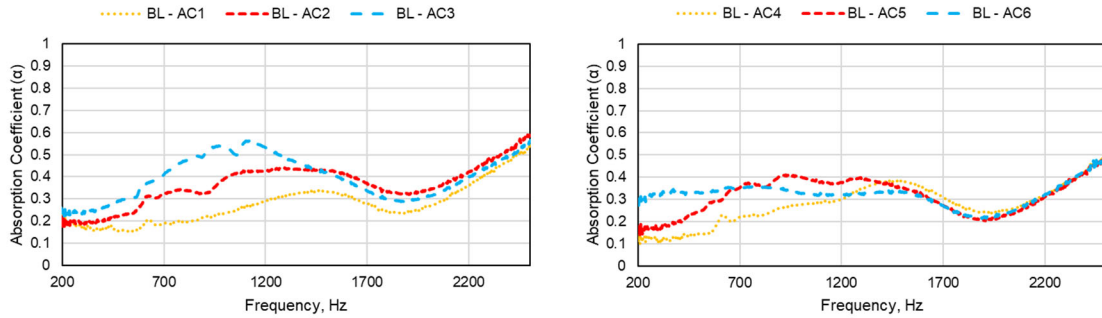
Figure 54: Baseline absorption coefficient results for CFM25 (left) and CFM30 (right) test samples. The yellow line represents the 0.635 cm thick sample, red is the 1.25 cm sample, and blue is the 2.54 cm sample

Comparing the thickness of the CFM25 foam shown in the chart on the left (in Figure 54), it is clear that with the increase of foam thickness there is a bump in the low-frequency (<~1200 Hz) acoustic performance. However, moving to the CFM30 test samples, the bump in the acoustic performance is reduced but can still be observed below 700 Hz, but above 700 Hz each of the datasets seem to begin to converge to a single line. This indicates that the performance of this type of foam with a bulk density nearing 0.5 g/cm^3 decreases the pore size to a point where the bulk of the acoustic wave is reflected rather than propagating throughout the medium.

4.5.1.1. L x W Dimension Comparison
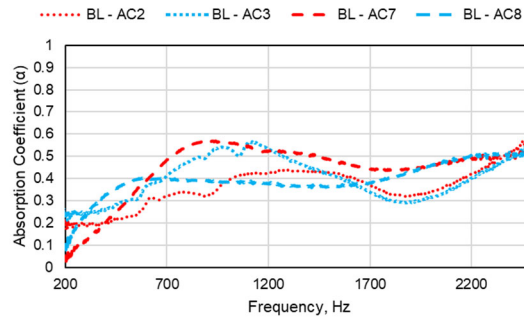
Figure 55: Absorption coefficient comparison for the L x W dimension testing. AC2 and AC3 have a side length of 5.08 cm while AC7 and AC8 have side lengths of 6.35 cm

It is very clear that there is a notable amount of performance to be gained by using the maximum dimensions (shown in Figure 55), however, after looking at this comparison another trend is a little more clearly seen. There is a peak that shifts to the lower frequencies when increasing from a 1.27 cm thick sample to a 2.54 cm thick sample. A deeper evaluation of this trend is required to further understand if this is an expected phenomenon or if there is a mistake in the testing of these CF liner samples.

4.5.2. Carbon Foam Spacing Comparison

The following test results (shown in Figure 56) are that from the spacing testing of the 5.08 cm x 5.08 cm samples.
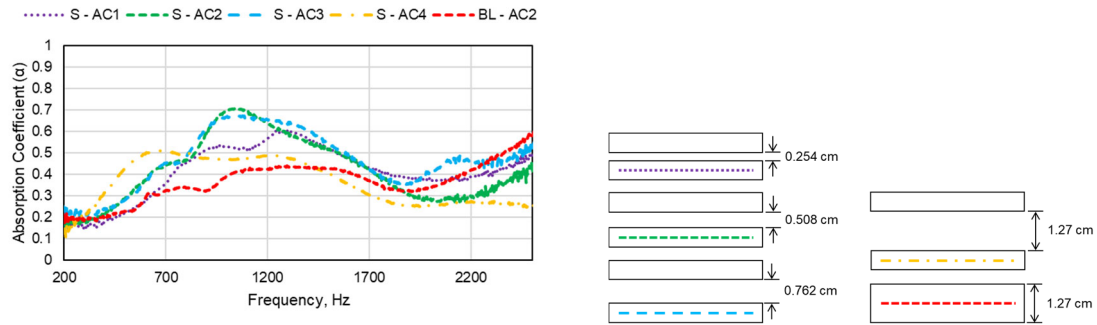
Figure 56: Comparison of the absorption coefficient for Carbon foam spacing tests (left), visual outline of test cases (right)

It is clear that with an increase of sample spacing from 0.254 cm to 0.508 cm, however increasing from 0.508 cm to 0.762 cm there appears to be little to no difference in the absorption peak or in the broadband performance. Lastly, increasing the spacing to 1.27 cm, there appears to be a low-frequency peak around 700 Hz with slightly increased sound mitigation at those lower frequencies below ~760 Hz. However, above this limit, the performance is decreased below each of the smaller induced air gaps. This indicates that there may be a limit to which the benefits of sample spacing are overpowered by the bulk of the absorption performance falling below the other test cases.

4.5.3. Membrane-Embedded Carbon Foam

The next and last set of experimental test cases is the membrane-embedded carbon foam test cases. Figure 57 is a comparison of the test cases referenced in Table 9.
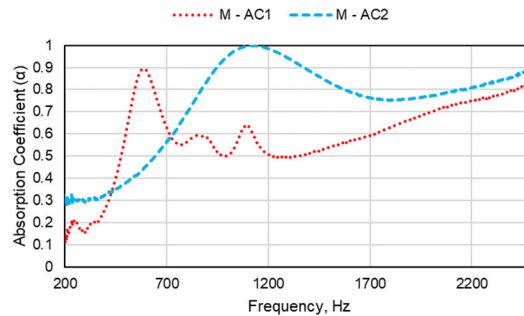
Figure 57: Comparison of the membrane-embedded carbon foam test cases, AC1 includes a membrane-embedded septum, AC2 includes a septum but no membrane

When considering the AC1 test case, the membrane clearly has a very good effect on the acoustic performance at 600 Hz with the first resonant mode of the membrane being excited. Overall, it appears that this design modification enables the carbon to have a drastically different low-frequency performance as well as the high-frequency performance than the other cases tested thus far. Switching to AC2, the peak that approaches unity at around 1150 Hz is an artifact of the quarter-wave resonance frequency. Introducing this perforation within the foam clearly has its benefits, but because of scope is not studied further in this paper.

4.5.4. Carbon Foam Modeling

Using the parameters outlined in Table 12, the following comparisons are made between COMSOL simulations and experiments. For these tests, the impedance (which is normalized with air) is provided along with the absorption coefficient. The first case presented in Figure 58 shows a comparison of the AC7 experimental test case compared with the corresponding simulation.
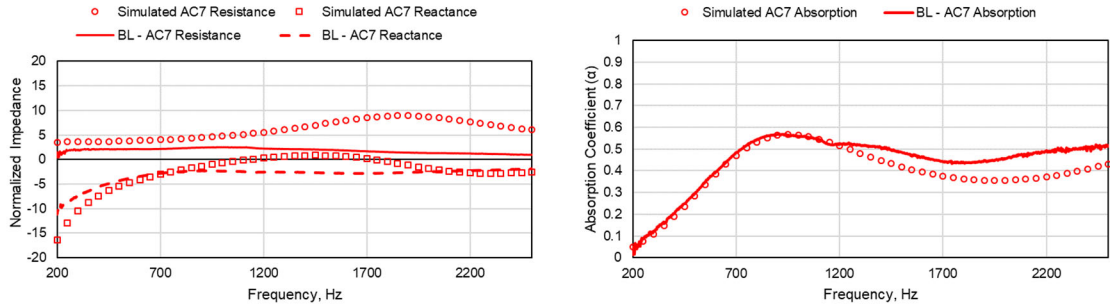
Figure 58: Comparison of the COMSOL simulated impedance vs the experiment (left) and the COMSOL simulated absorption vs experiment (right) for the baseline test case that is 1.27 cm thick

This being the pioneer case in attempts to determine the correct material parameters for the model inputs (i.e. there are no other published papers which attempt to describe the acoustic properties required to model this specific type of foam), the two datasets appear to match very well in the absorption coefficient, and other than the resistive portion of the impedance which is higher than the experiment, the impedance also has a good correlation to the experiment.

Figure 59 is the same comparison as in the previous figure but in the AC8 configuration.
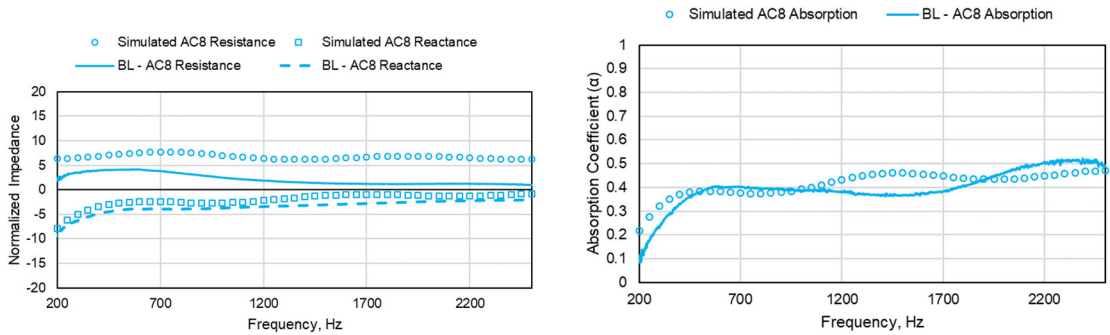
Figure 59: Comparison of the COMSOL simulated impedance vs the experiment (left) and the COMSOL simulated absorption vs experiment (right) for the baseline test case that is 2.54 cm thick

Moving to the increased 2.54 cm thickness sample which is twice that of the previous case, the absorption coefficient plot looks to agree for the most part. The impedance again holds to a similar trend as the previous test case. This is a good indication that the material properties that are implemented using the Attenborough poroacoustics model are accurate. As another

86

validation, the characteristic impedance is computed by using the two-thickness method. Using

the characteristic impedance, the surface impedance can be computed for any foam thickness.

The following plots are the comparisons for the 1.27 cm test case and the 2.54 cm test case to

check to ensure that the deduction of the characteristic impedance was successful. It should be

noted that the data used in the computation was geometrically smoothed using a 3-value moving

average of the original data.
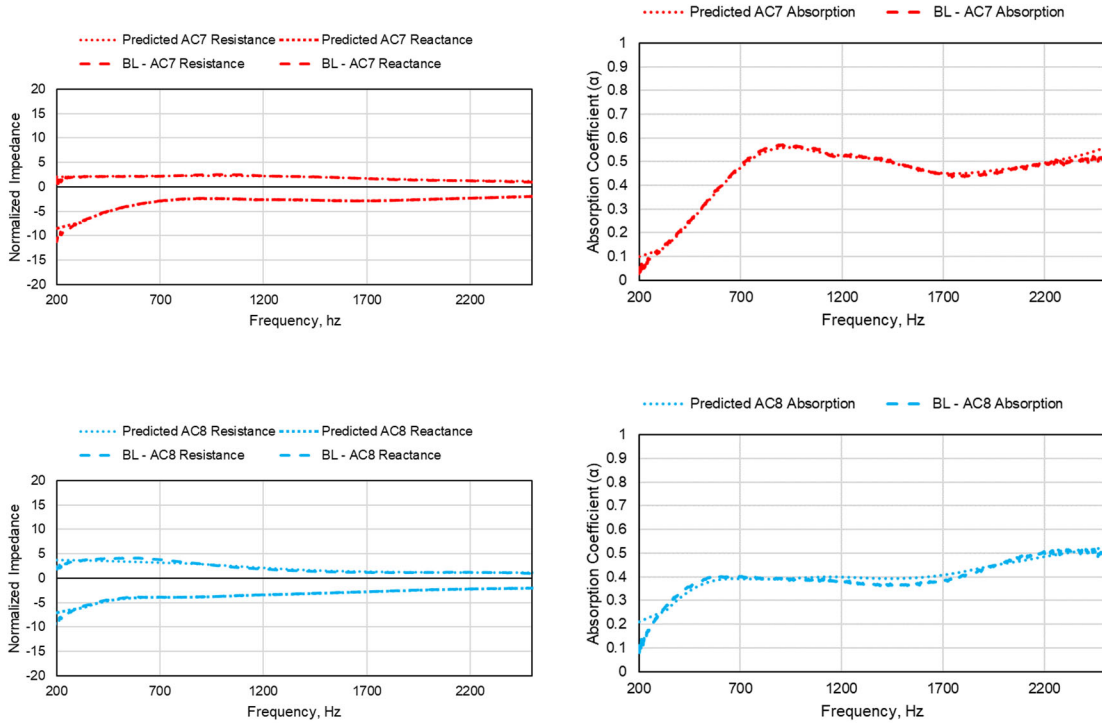
Figure 60: Comparison of acoustic performance predicted using the characteristic impedance

Figure 60 is a comparison of the acoustic performance predicted using the characteristic

impedance. Clearly, the match is nearly spot-on as the computation of the characteristic

impedance was from the experiment. With this being the case, using the characteristic impedance

and the Attenborough model in COMSOL, the surface impedance, and the absorption coefficient

is predicted at heights of 1.905 cm and 3.91 cm and then compared to one another.

Figure 61 displays a comparison of both of the prediction methods used to compute the

normalized surface impedance and absorption coefficient at two thicknesses that were not

experimentally tested.
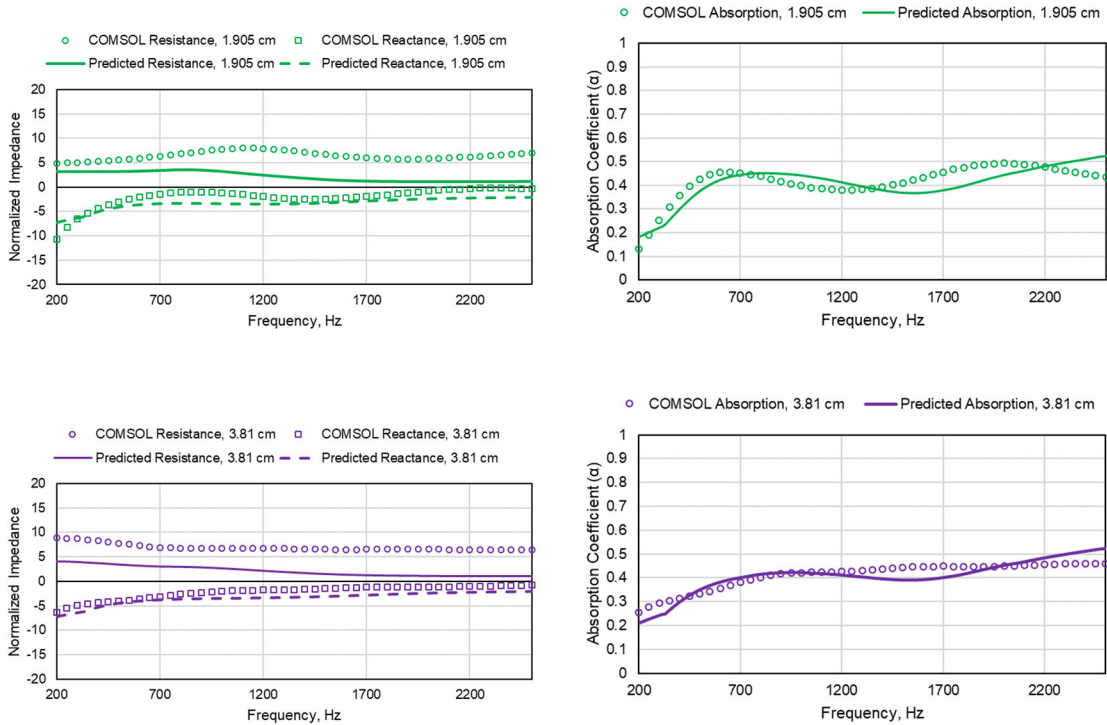
Figure 61: Comparison of the COMSOL simulation prediction and predicted acoustic response using the characteristic impedance

Both prediction models for the foam seem to agree very well with one another which indicates

that the properties used in the COMSOL simulation are accurate.

4.6.   Chapter Summary

In Chapter 4, carbon foam in various forms were tested and evaluated for their acoustic

performance. First, carbon foams of three different thicknesses were tested and results showed

that when the thickness of the foam is increased, the peak in the absorption coefficient peak is

shifted to lower frequencies. This is explained similar to how an empty cavity's resonance

frequency decreases when increasing the length, except in this case the medium is not air and instead interactions with a bulk material occur. Also, because the actual mechanism for absorption in rigid open cell foams is viscous dissipation, the addition of mass due to the increase overall length of the sample contributes to the observed result. Next, a comparison is made to determine the loss in the acoustic performance by using a decreased sample length and width dimensions. A series of tests are then conducted on the acoustic performance of an air gap is introduced between two samples of equal spacing. An increase in the air gap appears to increase the acoustic attenuation up to a certain point for mid frequencies after which the increase in air gap shows a slight decrease in the foam's resonance peak but also results in an observable decrease in the performance in the high frequencies. Overall, the spacing (air gap) variation tests demonstrate that significant improvement (>~50%) in mid-range absorption can be obtained. The final series of experimental tests was on the influence of a tensioned membrane that was sandwiched between two pieces of carbon foam. The test concluded that the inclusion of a membrane decreased the first resonant peak (due to the membrane) and increases the liner's overall acoustic performance. It is found that a significant absorption peak is obtained in the vicinity of the natural frequency (~600 Hz) of the tensioned membrane. Compared to the absorption for a carbon foam core with a blank septum, the membrane-embedded sample can deliver tunable low-frequency absorption improvement while retaining the broadband absorptive characteristics obtained for the carbon foam at higher frequencies. This indicates the potential of combining carbon foam-based acoustic absorbers with structurally resonant elements such as the tensioned membrane to obtain enhanced low-frequency absorption suitable for multifunctional applications.

In the literature review, many open-cell foam concepts are discussed [51-61], most of which require a significant thickness in order to absorb low frequencies. Various low-frequency absorbing configurations are presented in this thesis with various orders of absorption. It is clear

that there are still some optimizations that could be utilized for future testing to produce a better

absorbing carbon foam and will be discussed in Chapter 5.2.

CHAPTER V

Conclusions

5.1. Summary of Conclusions

Three lightweight, compact, low-frequency acoustic liner concepts were investigated using experiments and simulations in this study. These are the membrane-embedded liner (MEL), folded cavity liner (FCL), and the carbon foam liner (CFL). Special attention was paid to augmenting the absorption spectra below ~1000 Hz where conventional POHC and bulk acoustic liners are known to be inadequate. It is demonstrated that by incorporating a tensioned membrane that is embedded within a liner's mid septum can drastically increase the low-frequency noise mitigation potential compared with legacy SDOF and 2DOF liner concepts. Material, geometry, tension, and location of the membrane are used as tunable parameters. It is found that by increasing the height of the acoustic cavity below the membrane, the absorption peaks are shifted to lower frequencies. By altering the liner's cavity dimensions from a uniform cavity configuration to a non-uniform configuration, low-frequency (<~1000 Hz) broadband attenuation is achieved due to the generation of multiple absorption peaks corresponding to the different cavity sizes. The location of these peaks can be tailored to enhance absorption for specific low-frequency bandwidths. Simulations that were developed using COMSOL Multiphysics for the MEL display a very good match when comparing to the experiments. Affixing a mass to the center of the membrane within each cell was shown to decrease the overall resonance frequency of the embedded membrane, and for these test cases, the fundamental frequency is reduced to

between 300 and 500 Hz. Attaching a mass to the center of each cell is but one of many methods available to use as a tuning mechanism for the MEL configuration. By altering the geometry of the membrane (and as a consequence the corresponding cavities) low-frequency broadband attenuation is achieved. COMSOL simulations agree very well with the experiments. Further, perforated membranes, which allow both for frequency modification and communication between the top and bottom cavities of the core, or slanted core geometries that enables variation of the top and bottom cavity heights for different cells with in the same core can be used for additional tunability and operational utility for membrane-embedded liners. Next, an investigation is conducted into the optimization of an ultra-compact folded-cavity liner (FCL) concept to determine the bandwidth of appreciable absorption that can be engineered using this approach. Utilizing previous methodologies that were developed for the design and analysis of FCL, simulations utilizing the ZKTL method implemented in MATLAB are used to evaluate various compact configurations and select the most optimal ones for manufacture. Low-frequency tonal (as low as ~450 Hz) as well as broadband (in the 500 – 1000 Hz range) noise mitigation is achieved experimentally using a liner that is only 1.27 cm thick. Comparisons between the simulations and experiment agree well demonstrating the ability to target tunable low-frequency bandwidths or tones without any weight or volume penalty while retaining an ultra-compact form factor.

Finally, commercially-sourced carbon foam-based liner designs are evaluated to ascertain low-frequency attenuation potential. Carbon foams are known to have desirable thermal and mechanical properties which are advantageous for applications such as for liners for aircraft turbofan engine core-noise reduction. Parameters such as foam type, thickness, spacing, and membrane interaction are examined using experiments. Tailoring the spacing between the foam samples was found to significantly (>~50%) improve mid-range absorption. A low-frequency absorption peak is obtained in the vicinity of the natural frequency (~600 Hz) of the tensioned

membrane embedded within the CFL sample, indicating the potential of combining carbon foam-based acoustic bulk absorbers with structurally resonant elements such as the tensioned membrane to bolster low-frequency absorption. Simulations using COMSOL Multiphysics's Attenborough poroacoustics model as well as the two-thickness method are conducted using parameters estimated from experiments and compare well with each other. With current additive and hybrid manufacturing technologies attaining critical commercial maturity in recent times, it is indeed an opportune time to explore new and innovative liner designs that could enhance aerospace mission capabilities and contribute to sustainable global aviation.

5.2. Recommendations for Future Work

While this thesis has been focused on advancing the understanding of various lightweight and compact, low-frequency liner concepts and mechanisms aimed at improving the performance of acoustic liners, there is much scope for follow-on research. There are many different areas of potential research for each of the liner concepts that could be explored further. To start with, the membrane-embedded liner (MEL) concepts, the non-uniform liner concept, which displayed favorable broadband low-frequency performance, may have even more low-frequency performance left on the table. The specific design of the non-uniform core can be optimized so that the frequency responses of different cells are tuned to provide the best broadband, low-frequency absorption spectra within a given set of design constraints. Additionally, it may be possible to utilize customized ultra-thin plates instead of stretched membranes to create a more robust, adaptable, and durable structurally-resonant element for such liners. Stamped or machined ultra-thin plates can reduce fabrication complexity arising from embedding tensioned membranes and provide ease of tunability via customizing local thickness of the plates or introducing perforations in it within each cell to alter mass, stiffness, and structural-acoustic interaction. This approach may be more compatible with industry-standard materials and processes.

The folded-cavity liner investigation demonstrated proof-of-concept using aerospace-grade materials, however, another driving factor in the actual feasibility of the approach is the verification that there is no prohibitive degradation of the structural stiffness and strength of the core due to the cuts made in it to create the folded cavities. An initial effort was made to determine the reduction in the structural properties due to the internal cuts made in order to combine a series of cavities by conducting compression tests (which are presented in the appendix). However, this is only one type of honeycomb core tested while there are several different types used within an engine nacelle, say. An extension of the compression test presented in the appendix also to include additional types of structural tests for more core types such as Nomex cores would be helpful in establishing the potential of this type of design actually making its way onto future aircraft.

The investigation into carbon foam liner study is based on the commercially available CFOAM product. It may be possible to source or create carbon or carbon-graphite foam samples that are more optimized for low-frequency acoustic noise mitigation applications while retaining desirable thermal and mechanical properties. In addition, the influence of variation in the bulk temperature of the foam (as encountered during in-service conditions) on the acoustic response is worth examining. To continue the work on the membrane-embedded CFL case explored in this study, improving the design of the septum plates used to embed the tensioned membrane is appealing. In the current version, the acoustic wave traveling through the incident foam is blocked when it reaches the septum plates and the only interaction the acoustic wave has with the lower half of the liner is through the membrane. It may also be favorable to drill smaller perforations (smaller than the perforations made to account for the membrane) within the carbon foam to take advantage of the cavity resonance as well as the membrane and bulk properties of the foam. In conclusion, given the broad scope of the low-frequency aircraft noise mitigation application vis-à-vis the characteristics of the noise spectra in relation to the flight envelope, the wide variation in the

ambient conditions, and the stringent design constraints related to weight, volume, materials, and processes in the aerospace domain, it may be necessary to combine multiple concepts in a synergistic fashion to realize customized solutions. The development of a unified design methodology and associated modeling tool by building upon this study would be a valuable resource to this end.

REFERENCES

[1] United States Federal Aviation Administration's e-CFR Title 14, Chapter 1C, Part 36, 2018.

[2] J. J. Berton, "System Noise Prediction of the DGEN 380 Turbofan Engine," Journal of Aircraft, 53, 6, (2016).

[3] M. G. Jones, D. M. Nark, A. Baca, and C. R. Smith, "Applications of Parallel-Element, Embedded Mesh-Cap Acoustic Liner Concepts," AIAA/CEAS Aeroacoustics Conference, 3445, (2018).

[4] M. G. Jones, B. M. Howerton, and E. Ayle, "Evaluation of Parallel-Element, Variable-Impedance Broadband Acoustic Liner Concepts," AIAA/CEAS Aeroacoustics Conference, 2194, (2012).

[5] J. W. Wong, E. H. Nesbitt, M. G. Jones, and D. M. Nark, "Flight Test Methodology for NASA Advanced Inlet Liner on 737MAX-7 Test Bed (Quiet Technology Demonstrator 3)," AIAA/CEAS Aeroacoustics Conference, 2763, (2019).

[6] Hexcel. HexWeb® Acousti-Cap® Sound Attenuation Honeycomb. http://www.hexcel.com/Products/Honeycomb/HexWeb-Acousti-Cap (2017).

[7] Noise Control Act of 1972, P.L. 92-574, 86 Stat. 1234, 42 U.S.C. § 4901 - 42 U.S.C. § 4918.

[8] R. A. Mangiarotty, "The Reduction of Aircraft Engine Fan-Compressor Noise Using Acoustic Linings," Journal of Sound and Vibration 18, 1, (1971).

[9] D. L. Huff, "NASA Glenn's Contribution to Aircraft Engine Noise Research," NASA TP 217818, (2013).

[10] E. Garber, "Vibrating Strings and Eighteenth-Century Mechanics. In: The Language of Physics," Birkhäuser, Boston, (1999).

[11] R. Grimsley, "Jean Le Rond d'Alembert," Encyclopedia Britannica, https://www.britannica.com/biography/Jean-Le-Rond-dAlembert, (2008).

[12] P. H. Tuan, C. P. Wen, P. Y. Chiang, and Y. T. Yu, "Exploring the Resonant Vibration of Thin Plates: Reconstruction of Chladni Patterns and Determination of Resonant Wave Numbers," The Journal of the Acoustical Society of America, 137, 4, (2015).

[13] H. V. Helmholtz and A. J. Ellis, "On the Sensations of Tone as Physiological Bias for the Theory of Music," Dover Publications, (1954).

[14] L. Patton, "Hermann von Helmholtz," The Stanford Encyclopedia of Philosophy, (2016).

[15] Prediction of the Thermoacoustic Combustion Instability in Gas Turbines - Scientific Figure on ResearchGate. Available from: https://www.researchgate.net/figure/A-brass-spherical-Helmholtz-resonator-based-on-his-original-design-circa-1890-1900_fig27_235328588, (2020).

[16] Lord Rayleigh, "Theory of Sound: Volume II," The MacMillan Company, 319-326, (1896).

[17] G. Kirchhoff, "Ueber den Einfluss der Wärmeleitung in einem Gase auf die Schallbewegung," Ann. Phys., 210, 6, 177-193, (1868).

[18] D. E. Weston, "The Theory of the Propagation of Plane Sound Waves in Tubes," Proceedings of the Physical Society (Section B), 66, 695, (1953).

[19] C. Zwikker and C. W. Kosten, "Sound Absorbing Materials," Elsevier, (1949).

[20] H. Tijdeman, "On the Propagation of Sound Waves in Cylindrical Tubes," Journal of Sound and Vibration, 39, 1, 1-33, (1975).

[21] K. Attenborough, "On the Acoustic Slow Wave in Air Filled Granular Media," The Journal of the Acoustical Society of America, 81, 1, 93–102, (1987).

[22] J.F. Allard and N. Atalla, "Propagation of Sound in Porous Media," Modeling Sound Absorbing Materials, 2nd Edition, John Wiley & Sons, (2009).

[23] M. Delany and E. Bazley, "Acoustical Properties of Fibrous Absorbent Materials," Applied Acoustics, 3, (1970).

[24] C. E. Feiler and E. W. Conrad, "Fan Noise from Turbofan Engines," Journal of Aircraft, 13, 2, 128-134, (1976).

[25] C. E. Feiler, J. E. Merriman, "Effects of Forward Velocity and Acoustic Treatment on Inlet Fan Noise," NASA/TM, 71591, (1974).

[26] X. Ma and Z. Su, "Development of Acoustic Liner in Aero Engine: A Review," Science China, 63, (2020).

[27] U. Ingard, "On the Theory and Design of Acoustic Resonators," Journal of Acoustical Society of America, 25, 6, (1953).

[28] C. J. Naify, C. M. Chang, G. McKnight, and S. Nutt, "Transmission Loss and Dynamic Response of Membrane-Type Locally Resonant Acoustic Metamaterials," Journal of Applied Physics, 108, 114905, (2010).

[29] C. Naify, M. Sneddon, and S. Nutt, "Noise Reduction of Honeycomb Sandwich Panels with Acoustic Mesh Caps," Acoustical Society of America, 8, 065002, (2009).

[30] L. Y. Ang, Y. K. Koh, and H. P. Lee, "Plate-Type Acoustic Metamaterials: Experimental Evaluation of a Modular Large-Scale Design for Low-Frequency Noise Control," Applied Physics Letters, 112, 051903, (2018).

[31] G. C. Lam, R. C. Leung, H. K. Fan, and Y. Auregan, "Effect of Back Cavity Configuration on Performance of Elastic Panel Acoustic Liner with Grazing Flow," Journal of Sound and Vibration, 492, 115847, (2021).

[32] S. Huang, E. Zhou, Z. Huang, P. Lei, Z. Zhou, and Y. Li, "Broadband Sound Attenuation by Metaliner Under Grazing Flow," Applied Physics Letters, 118, 063504, (2021).

[33] U. Ackermann, H. V. Fuchs, and N. Rambausek, "Sound Absorbers of a Novel Membrane Construction," Applied Acoustics, 25, 197-215, (1988).

[34] W. Frommhold, H. V. Fuchs, and S. Sheng, "Acoustic Performance of Membrane Absorbers," Journal of Sound and Vibration, 5, 170, 621-636, (1994).

[35] L. Fan, Z. Chen, S. Zhang, J. Ding, X. Li, and H. Zhang, "An Acoustic Metamaterial Composed of Multi-Layer Membrane-Coated Perforated Plates for Low-Frequency Sound Insulation," Applied Physics Letters, 106, 151908 (2015).

[36] G. Ma, M. Yang, Z. Yang, and P. Sheng, "Low-Frequency Narrow-Band Acoustic Filter with Large Orifice," Applied Physics Letters, 103, 011903, (2013).

[37] T. Y. Huang, C. Shen, and Y. Jing, "Membrane- and Plate-Type Acoustic Metamaterials," The Journal of the Acoustical Society of America, 139, 3240, (2016).

[38] N. Sui, X. Yan, T. Huang, J. Xu, F. Yuan, and Y. Jing, "A Lightweight Yet Sound-Proof Honeycomb Acoustic Metamaterial," Applied Physics Letters, 106, 171905, (2015).

[39] S. Chen, Y. Fan, Q. Fu, H. Wu, Y. Jin, J. Zheng, and F. Zhang, "A Review of Tunable Acoustic Metamaterials," Applied Sciences, 8, 1480, (2018).

[40] Y. Chen, G. Huang, X. Zhou, G. Hu, and C. Sun, "Analytical Coupled Vibroacoustic Modeling of Membrane-Type Acoustic Metamaterials: Membrane Model," The Journal of the Acoustical Society of America, 136, 969, (2014).

[41] G. Palma, H. Mao, L. Burghignoli, P. Goransson, and U. Lemma, "Acoustic Metamaterials in Aeronautics," Applied Sciences, 8, 971, (2018).

[42] F. Langfeldt, J. Riecken, W. Gleine and O. von Estorff, "A Membrane-Type Acoustic Metamaterial with Adjustable Acoustic Properties," Journal of Sound and Vibration, 373, (2016).

[43] J. Guo, Y. Fang, Z. Jiang, and X. Zhang, "An Investigation on Noise Attenuation by Acoustic Liner Constructed by Helmholtz Resonators with Extended Necks," The Journal of the Acoustical Society of America, 149, 70, (2021).

[44] J. R. Kreitzman, F. T. Calkins, D. E. Nicholson, A. F. Lafranchi, C. A. Dodge, and L. N. Cattafesta, "Active Acoustic Liners Enabled by Shape Memory Alloy Technology," AIAA/CEAS Aeroacoustics Conference, 2617, (2020).

[45] M. Mischke, S. Kazula, and K. Hoschler, "A Comparative Concept Study and Evaluation for New Broadband Noise Absorbing Acoustic Liner Concepts for Civil Aviation," Global Power and Propulsion Society, 0046, (2019).

[46] G. Tissot, R. Billard, and G. Gabard, "Optimal Cavity Shape Design for Acoustic Liners Using Helmholtz Equation with Visco-Thermal Losses," Journal of Computational Physics, 109048, 402, (2020).

[47] J. Yu and E. Chien. "Folding Cavity Acoustic Liner for Combustion Noise Reduction," AIAA/CEAS Aeroacoustics Conference, 2681, (2006).

[48] A. T. Chambers, J. M. Manimala, and M. G. Jones, "Improved Low-Frequency Broadband Absorption using 3D Folded Cavity Acoustic Liners," In proceedings of the Institute of Noise Control Engineering's Noise-Con Conference, 46, 547-554, (2017).

[49] M. G. Jones, W. R. Watson, D. M. Nark, and B. M. Howerton, "Evaluation of Variable-Depth Liner Configurations for Increased Broadband Noise Reduction," AIAA/CEAS Aeroacoustics Conference, 2697, (2015).

[50] M. M. Marinova, M. G. Jones, and N. H. Schiller, "Evaluation of Packing_3D Code for Design of Variable-Depth Bent-Chamber Acoustic Liners," NASA/TM, 220560, (2020).

[51] D. L. Sutliff and M. G. Jones, "Foam-Metal Liner Attenuation of Low-Speed Fan Noise," AIAA/CEAS Aeroacoustics Conference, 2897, (2008).

[52] M. G. Jones, T. L. Parrott, D. L. Sutliff, and C. E. Hughes, "Assessment of Soft Vane and Metal Foam Engine Noise Reduction Concepts," AIAA/CEAS Aeroacoustics Conference, 3142, (2009).

[53] M. A. Kuczmarski and J. C. Johnston, "Acoustic Absorption in Porous Materials," NASA/TM, 216995, (2011).

[54] D. Cuiyun, C. Guang, X. Xinbang, and L. Peisheng, "Sound Absorption Characteristics of a High-Temperature Sintering Porous Ceramic Material," Applied Acoustics, 73, 865-871, (2012).

[55] M. Janus-Michalska and R. B. Pecherski, "Macroscopic Properties of Open-Cell Foams Based on Micromechanical Modeling," Technische Mechanik, 23, (2003).

[56] K. Shelts, L. Peterson, A. Lomte, O. Khaleel, and B. Sharma, "Characterizing the Relationship between Microstructural and Acoustic Properties of Open-Celled Metal Foams," In proceedings of the Institute of Noise Control Engineering's Noise-Con Conference, 164, (2019).

[57] J. Googin, J. Napier, and M. Scrivner, "Method for Manufacturing Foam Carbon Products," US Patent 3.345.440., (1967).

[58] Klett, J, "Process for Making Carbon Foam," US Patent 6.033.506., (2000).

[59] R. Gaeta, "The Sound Absorbing Potential of Carbon-Graphite Foam," AIAA/CEAS Aeroacoustics Conference, 2405, (2006).

[60] M. R. Gazella, T, Takakura, D. L. Sutliff, R. Bozak, and B. J. Tester, "Evaluating the Acoustic Benefits of Over-the-Rotor Acoustic Treatments Installed on the Advanced Noise Control Fan," AIAA/CEAS Aeroacoustics Conference, 3872, (2017).

[61] R. F. Bozak and R. P. Dougherty, "Measurement of Noise Reduction from Acoustic Casing Treatments Installed Over a Subscale High Bypass Ratio Turbofan Rotor," AIAA/CEAS Aeroacoustics Conference, 4099, (2018).

[62] A. A. Svetgoff and J. M. Manimala, "Absorption Characteristics of Membrane-Embedded Acoustic Liners," In proceedings of the Institute of Noise Control Engineering's Inter-Noise Conference, 47, 2046, (2018).

[63] A. A. Svetgoff and J. M. Manimala, "Optimization of Resonant Mechanisms in Acoustic Metastructures for Low-Frequency Aerospace Applications," In proceedings of the Institute of Noise Control Engineering's Noise-Con Conference, 182, (2019).

[64] ASTM E1050-12, "Standard Test Method for Impedance and Absorption of Acoustical Materials Using a Tube, Two Microphones and a Digital Frequency Analysis System."

[65] M. G. Jones, W. R. Watson, D. M. Nark, B. Howerton, and M. C. Brown, "A Review of Acoustic Liner Experimental Characterization at NASA Langley," NASA/TP, 220583, (2020).

[66] M. G. Jones and T. L. Parrott, "Evaluation of a Multi-Point Method for Determining Acoustic Impedance," Journal of Mechanical Systems and Signal Processing, 3, 1, 15-35, (1989).

[67] T. L. Parrott and M. G. Jones, "Parallel-Element Liner Impedances for Improved Absorption of Broadband Sound in Ducts," Noise Control Engineering Journal, 43, 6, 183-195, (1995).

[68] J. Y. Chung and D. A. Blaser, "Transfer Function Method of Measuring In-Duct Acoustic Properties: I. Theory," Journal of Acoustical Society of America, 68, 907-921, (1980).

[69] J. J. Kelly and H. Abu-Khajeel, "A User's Guide to the Zwikker-Kosten Transmission Line Code (ZKTL)," NASA CR-97-206901, (1997).

[70] W. Watson, M Jones, S. Tanner, and T. Parrott, "Validation of a Numerical Method for Extracting Liner Impedance," AIAA/CEAS Aeroacoustics Conference, 34, 3, (1996).

[71] A Standard Test Method for Measurement of Normal Incidence Sound Transmission of Acoustical Materials Based on the Transfer Matrix Method, ASTM Standard E2611-09 (ASTM International, West Conshohocken, PA, 2009).

[72] J. R. Callicoat, "Evaluation of Composite Materials Providing Improved Acoustic Transmission Loss for UAVs," Doctor of Philosophy Thesis, Oklahoma State University, (2016).

[73] M. Drew, R. Spradling, and A. Guth, "Carbon Foams," Advanced Materials & Processes, 29-31, (2003).

[74] D. L. Sutliff, D. M. Elliott, M. G. Jones, and T. C. Hartley, "Attenuation of FJ44 Turbofan Engine Noise with a Foam-Metal Liner Installed Over-the-Rotor," NASA/TM, 215666, (2009).

APPENDICIES

A1. Additional Data

A1.1. Low-Tension MEL

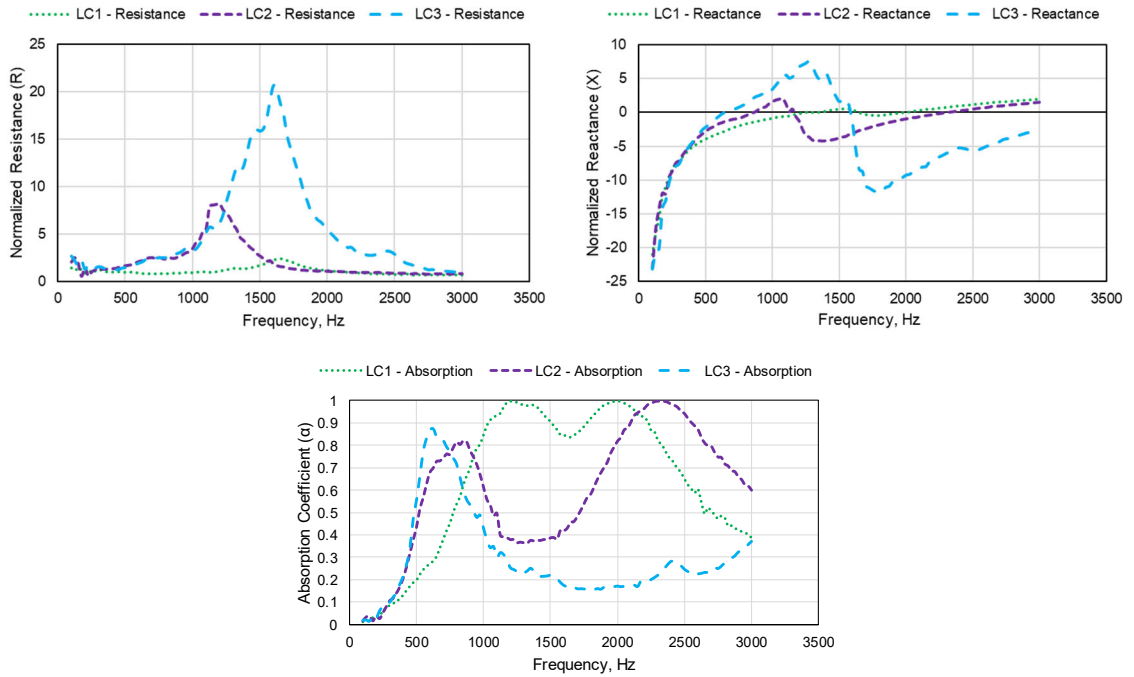The following plots contain the data sets excluded from Table 1.

Figure A1.1: Resistance (top left), reactance (top right), and absorption coefficient (bottom) plots for the low-tension baseline membrane-embedded liner design configuration at a sound pressure level of 140 dB
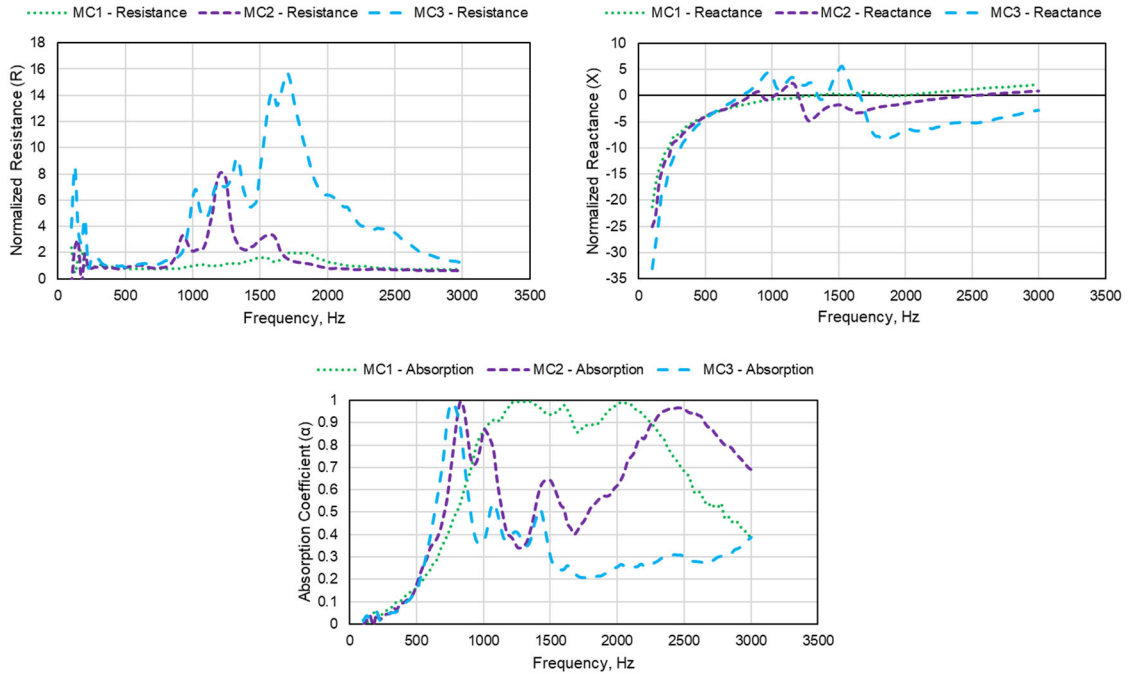
A1.2. Medium-Tension MEL

Figure A1.2: Resistance (top left), reactance (top right), and absorption coefficient (bottom) plots for the medium-tension baseline membrane-embedded liner design configuration at a sound pressure level of 140 dB

The low-tension test cases (LC1-LC3) appear to have a smeared acoustic response when comparing to the corresponding medium- and high-tension test cases. Thus, it cannot be clearly stated that the observed data is the true response due to the membrane for the low-tension case where there was no added weight on the tensioning rig when outfitting the septum plates with a membrane. The medium-tension test case very closely resembles the high-tension test case.

The following charts contain the impedance and absorption spectra for configurations listed in Table 2, but not shown in Chapter 2.

A1.3. MEL Height Study

The following charts contain the impedance and absorption spectra for configurations listed in Table 2, but not shown in Chapter 2.
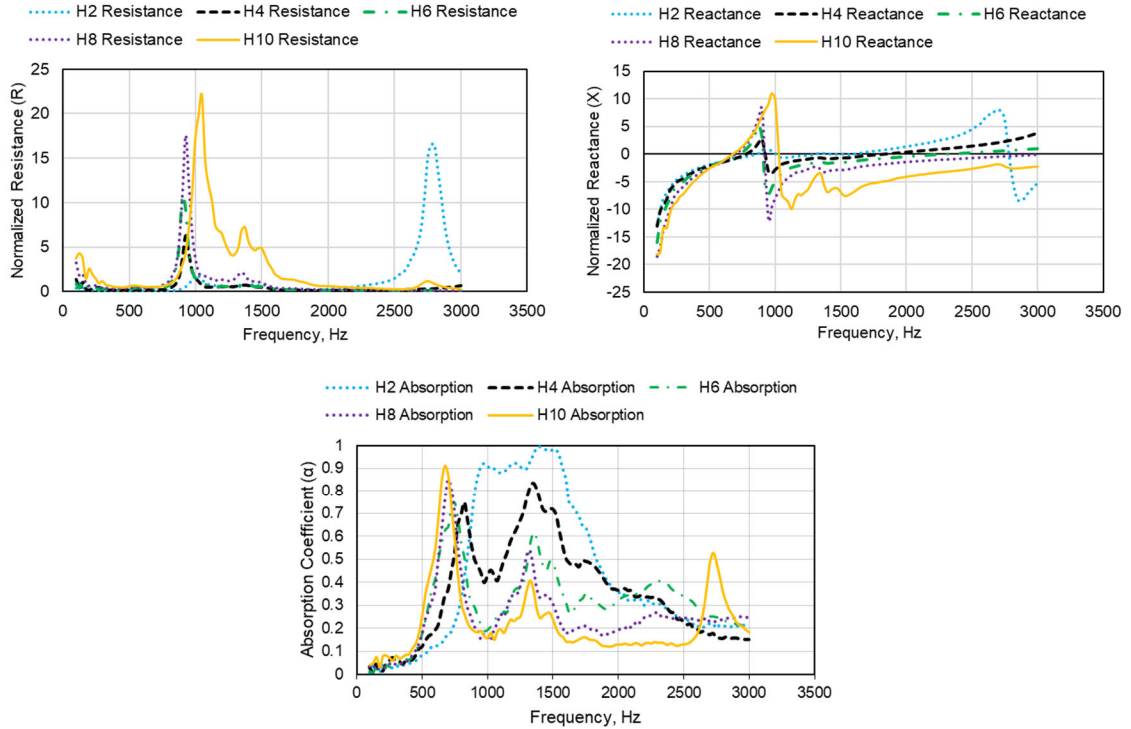

Figure A1.3: Impedance and absorption spectra for test cases listed in Table 2 but not shown within Chapter 2

A1.4. Membrane Height Investigation

To further the understanding of the mechanism at play, the impedance spectra for several of the membrane-embedded configurations are run through a NASA multipoint wave propagation code which has the ability to return the standing wave patterns with respect to an axial location centering at the membrane height location and extending ~13 cm in each normal direction. The configurations chosen to investigate are based on axial membrane height measured from the backplate and first resonant peak seen on the absorption coefficient plots or from the first zero crossing in the reactance curves (see **Error! Reference source not found.**Figure A1.3). The table below contains the list of test cases presented in this effort.

Case Number	Total Liner Height, cm	Membrane Height, cm	Frequency, Hz
SW1	7.62	6.35	675
SW2	7.62	5.08	700
SW3	7.62	3.81	725
SW4	7.62	2.54	775
SW5	7.62	1.27	875
SW6	7.62	1.27	600
SW7	7.62	1.27	400

Since this was a very targeted study, each of the test cases was specifically chosen. For the first five cases (SW1-SW5), the purpose is to look at the location of the standing wave in regard to the first resonant peak. For the plot containing data for SW5-SW7, the membrane height was held constant but the frequency in question is decreased. This is to essentially track the location of the wave as it approached the first resonant peak.
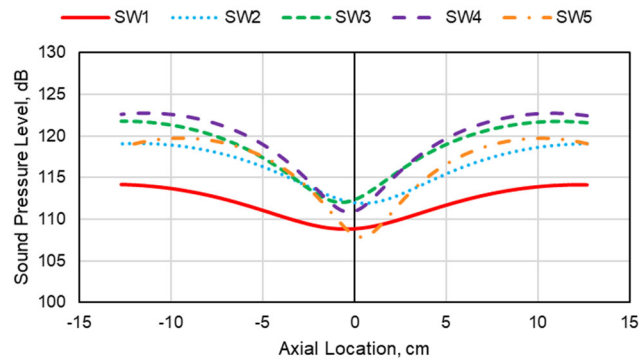

Figure A1.4: Sound pressure level vs. axial location results from NASA propagation code

From this plot, it appears that when analyzing the sound pressure level with respect to axial location, there is a distinct peak at an axial location equal to zero. Which again, corresponds to the liner surface, and that peak corresponds to a maximum in the particle velocity, and a minimum or null in the pressure wave approaching the height of the membrane.
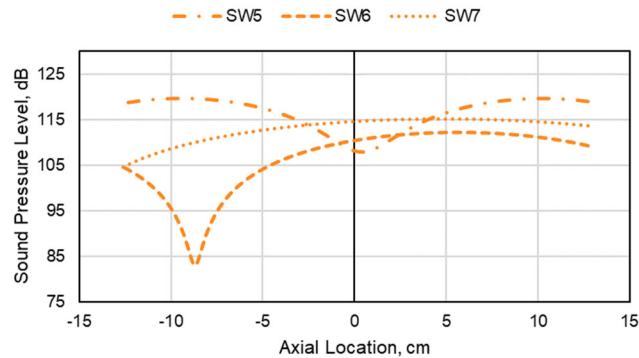

Figure A1.5: Investigation into the approaching standing wave on the resonant frequency

By isolating a single liner configuration and only altering the frequency in question, it appears that going from SW5 (875 Hz) to SW6 (600 Hz) the sharp dip shifts from the axial location of 0

cm to around 8 cm. Furthermore, in SW7 (400 Hz) the dip has far left the chart all together which indicates that the first resonant peak corresponds with a maximum in the particle velocity at the liner surface or when there is a dip in the sound pressure level.

Observing these datasets together, there seems to be another phenomenon occurring in relation to the shape of the dip, or the sharpness of the dip. When the dip is very sharp as in SW5, the impedance is relatively flat and the absorption coefficient contains good broadband attenuation. When the dip is more or less flat like in SW1 the impedance is choppy, and the absorption coefficient has good low-frequency narrowband performance.

This knowledge, albeit does not directly correspond with the main objectives of this thesis but can enable better design of future membrane-embedded liner configurations and can act as a potential tuning mechanism.

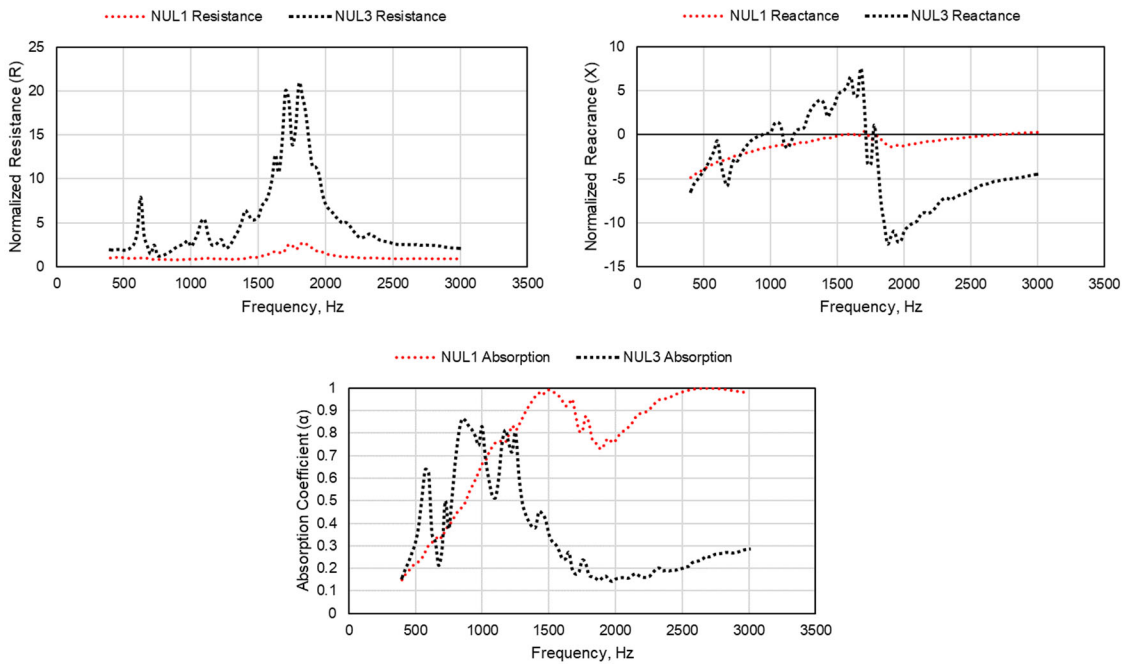The following plots contain the data sets excluded from Table 6.

Figure A1.6: Resistance (top left), reactance (top right), and absorption coefficient (bottom) for the NUL liner configurations conducted at a sound pressure level of 120 dB
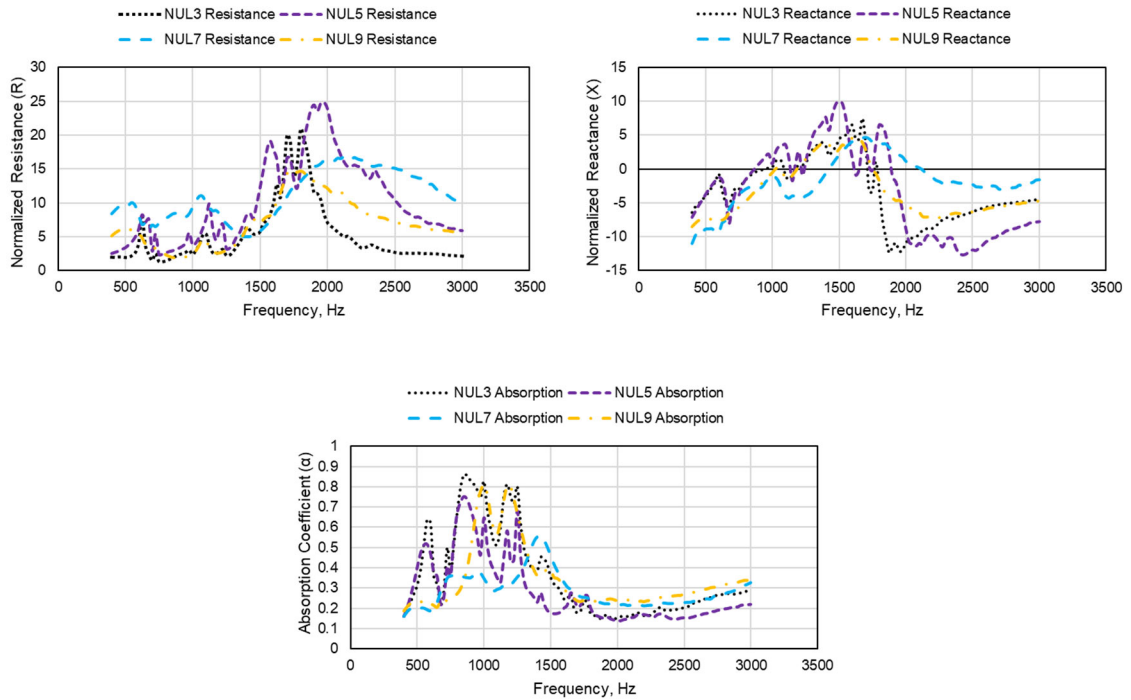
Figure A1.7: Resistance (top left), reactance (top right), and absorption coefficient (bottom) plots for the NUL liner cavity investigation conducted at a sound pressure level of 120 dB

It is clear when comparing the plots for the impedance and absorption coefficient at a sound pressure level of 120 dB to the corresponding datasets at 140 dB that there is no significant difference. This infers that the membrane is behaving somewhat linear in regard to the acoustic response. Albeit membrane linearity is not a primary focus of this thesis but for completeness, both datasets are provided within this thesis.

A1.5. Folded-Cavity Compression Test

In order to get a better idea of how much of an impact making internal modifications to the honeycomb has on the compression strength of the liner, a compression test was conducted on a non-modified liner with an identical facesheet and backplate as in FC2. The same test was then conducted on the modified FC2 liner after all experimental tests had concluded as this destructive test would eliminate any hopes of further acoustic testing. A comparison can be found in the following figures as well as photos of the test samples.
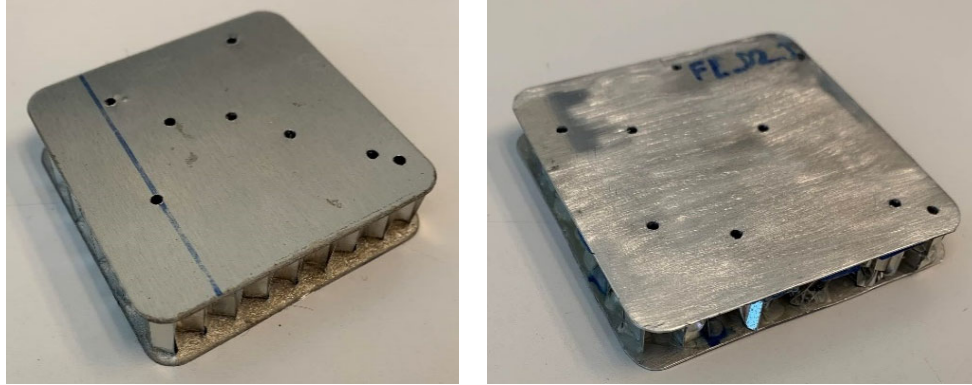
Figure A1.8: Baseline configuration (left) and FC2 (right) after the destructive testing
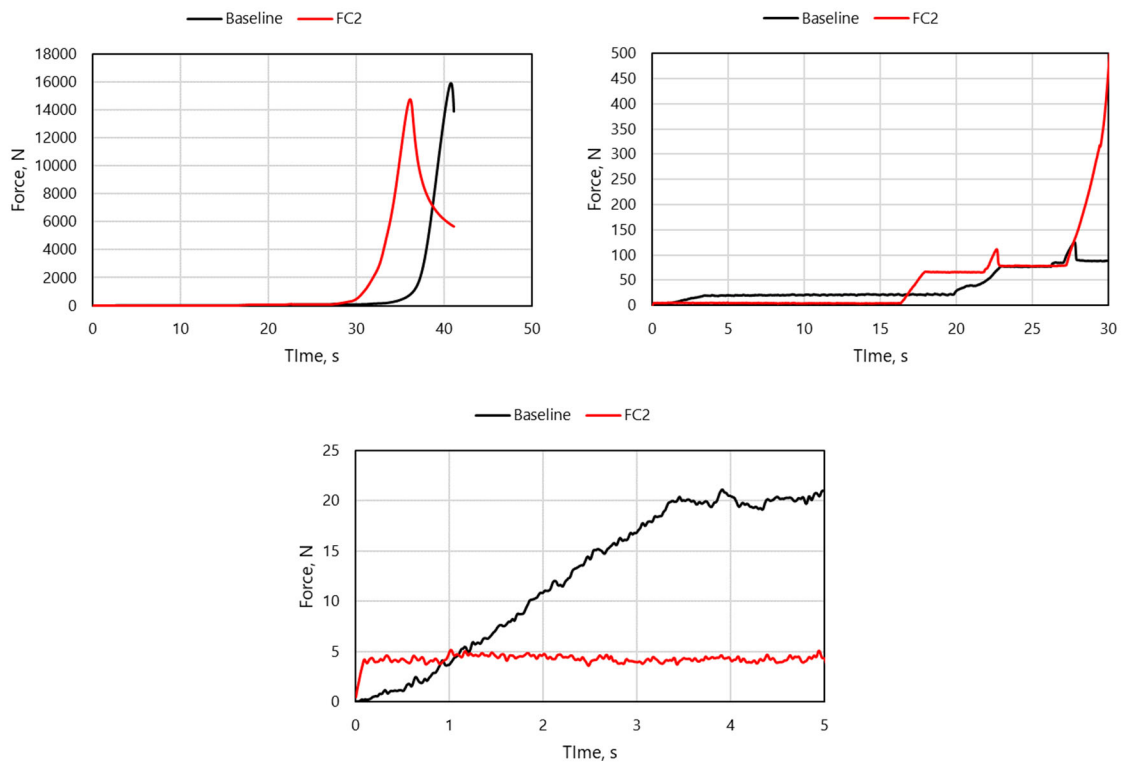

Figure A1.9: Compression testing test results, unmodified data (top left), modified time scale and force (top right), isolated first failure mode (bottom)

At first glance, it appears that the modifications to the honeycomb do not result in a large impact on the structural integrity of the overall liner. But by zooming in on the first 5 seconds of the compression test, a different story can be observed. The baseline (unmodified) test sample retains its strength completely until the first failure mode is discovered at 20 N. The FC2 test sample appears to have failed at 25% of the baseline. This discovery provides even more evidence on the need to do more testing on various types of honeycomb and possibly even various methods used to adjoin the interconnected cavities in order to obtain a design that retains the compression strength close to the baseline.

A2. MATLAB Code for the Two-Thickness Method

```matlab
function TTM(TTM_file)

% inputs
sheet = 2;
rowStart = 3;
rowStop = 1203;

% read the data in from a spreadsheet
freq = xlsread(TTM_file,sheet,sprintf('A%d:A%d',rowStart,rowStop));
R1   = xlsread(TTM_file,sheet,sprintf('B%d:B%d',rowStart,rowStop));
X1   = xlsread(TTM_file,sheet,sprintf('C%d:C%d',rowStart,rowStop));
R2   = xlsread(TTM_file,sheet,sprintf('E%d:E%d',rowStart,rowStop));
X2   = xlsread(TTM_file,sheet,sprintf('F%d:F%d',rowStart,rowStop));

% smooth the data out a little bit
% window=3;
% [R3,window] = smoothdata(R1);
% [X3,window] = smoothdata(X1);
% [R4,window] = smoothdata(R2);
% [X4,window] = smoothdata(X2);

% form the smoothed complex impedance functions
% Z1 = R3 + 1i*X3;
% Z2 = R4 + 1i*X4;
Z1 = R1 + 1i*X1;
Z2 = R2 + 1i*X2;

% parameters
d1 = 0.5;
d2 = 1.0;

% solving for various parameters & computing the characteristic impedance
a = sqrt((2.*Z2-Z1)./(Z1));
la = log((1+a)./(1-a));

% unwrapping the data to account for microphone phase mismatching
Qila = unwrap(imag(la));
gamma = (1/(2*d1)).*(real(la) + 1i*Qila);

Zc = sqrt(Z1.*(2.*Z2-Z1));

ds = 0.5;
Zs = Zc.*coth(gamma.*ds);
abs = (4.*real(Zs))./((real(Zs)+1).^2+(imag(Zs)).^2);

% % plotting the imagionary part of "la"
% figure
% plot(freq, Qila)

% figure
% plot(freq, real(Zc), freq, imag(Zc))

figure
subplot(2,1,1)
plot(freq,real(Zs),freq,imag(Zs))
title('Surface Impedance')
ylim([-10 5])
subplot(2,1,2)
```

```matlab
plot(freq,abs)
title('Absorption Coefficient')
ylim([0 1])


% % write the data to a spreadsheet
% filename = 'characteristic_impedance.xlsx';
% sheet=1;
% xlRange = 'A1';
% xlswrite(filename, freq, sheet, xlRange);
% sheet=1;
% xlRange = 'B1';
% xlswrite(filename, gamma, sheet, xlRange);
% sheet=1;
% xlRange = 'C1';
% xlswrite(filename, realZc, sheet, xlRange);
% sheet=1;
% xlRange = 'D1';
% xlswrite(filename, imagZc, sheet, xlRange);
%
% filename = 'predicted_surface_impedance.xlsx';
% sheet=1;
% xlRange = 'A1';
% xlswrite(filename, freq, sheet, xlRange);
% sheet=1;
% xlRange = 'B1';
% xlswrite(filename, realZs, sheet, xlRange);
% sheet=1;
% xlRange = 'C1';
% xlswrite(filename, imagZs, sheet, xlRange);
% sheet=1;
% xlRange = 'D1';
% xlswrite(filename, abs, sheet, xlRange);

% filename = 'smoothed_impedance.xlsx';
% sheet=1;
% xlRange = 'A1';
% xlswrite(filename, freq, sheet, xlRange);
% sheet=1;
% xlRange = 'B1';
% xlswrite(filename, R3, sheet, xlRange);
% sheet=1;
% xlRange = 'C1';
% xlswrite(filename, X3, sheet, xlRange);
% sheet=1;
% xlRange = 'D1';
% xlswrite(filename, R4, sheet, xlRange);
% sheet=1;
% xlRange = 'E1';
% xlswrite(filename, X4, sheet, xlRange);

end
```

VITA

Alexander A. Svetgoff

Candidate for the Degree of

Master of Science

Thesis: AN INVESTIGATION OF LIGHTWEIGHT CONCEPTS FOR
LOW-FREQUENCY PERFORMANCE ENHANCEMENT IN ACOUSTIC
LINERS

Major Field: Mechanical and Aerospace Engineering

Biographical:

Education:

Completed the requirements for the Master of Science in Mechanical and
Aerospace Engineering at Oklahoma State University, Stillwater, Oklahoma in
May, 2021.

Completed the requirements for the Bachelor of Science in Mechanical
Engineering at Oklahoma State University, Stillwater, Oklahoma in December,
2018.

Experience:

AST Aerospace Engineer   June 2020 - Present
NASA Glenn Research Center
Cleveland, OH

Acoustics Engineering Intern   May 2019 – August 2019
Spirit AeroSystems
Wichita, KS

Research Assistant   December 2018 - May 2021
Oklahoma State University
Stillwater, OK

Engineering Intern   May 2017 - August 2017, May 2018 - August 2018
NASA Langley Research Center
Hampton, VA